COHERENTLY CONTROLLED SPIN-DEPENDENT CHARGE CARRIER TRANSITIONS IN ORGANIC SEMICONDUCTORS: PROPERTIES AND APPLICATIONS

by

William J. Baker

A dissertation submitted to the faculty of
The University of Utah
in partial fulfillment of the requirements for the degree of

Doctor of Philosophy

in

Physics

Department of Physics and Astronomy

The University of Utah

August 2012

The University of Utah Graduate School

STATEMENT OF DISSERTATION APPROVAL

The dissertation of **William J. Baker**

has been approved by the following supervisory committee members:

Christoph Boehme	, Chair	**June 11, 2012** Date Approved
John M. Lupton	, Member	**June 11, 2012** Date Approved
Oleg Starykh	, Member	**June 11, 2012** Date Approved
Kyle Dawson	, Member	**June 11, 2012** Date Approved
Jennifer Shumaker-Parry	, Member	**June 11, 2012** Date Approved

and by **David B. Kieda**, Chair of the Department of **Physics and Astronomy**

and by Charles A. Wight, Dean of The Graduate School.

ABSTRACT

This thesis is focused on the investigation of the fundamental physical nature and potential technical applications of spin-dependent charge carrier recombination in poly[2-methoxy-5-(2'-ethyl-hexyloxy)-1,4-phenylene vinylene (MEH-PPV), a π conjugated polymer which has been utilized as organic thin film semiconductor. Pulsed electrically detected magnetic resonance (pEDMR) spectroscopy was used to observe how coherent spin motion of paramagnetic charge carrier states (so called polarons) control the macroscopic conductivity of thin ($\sim$100nm) MEH-PPV layers under different charge carrier injection regimes. The pEDMR experiments were conducted at frequencies covering almost three orders of magnitude ($\sim$20MHz to $\sim$10GHz) and at temperatures between $\sim$5K and $\sim$300k. The measurements revealed that under balanced bipolar injection, the conductivity of MEH-PPV is influenced at any temperature by the polaron pair (PP) mechanism, a spin-dependent process previously described in the literature. The experiments showed that PPs are weakly exchange- and dipolar-coupled pairs but they are strongly influenced by proton induced hyperfine fields. Electrical detection of coherent polaron-spin motion revealed extraordinary long coherence times (order of μs) at room temperature which could qualify PPs for quantum information applications. The PP mechanism was also demonstrated to work as an extraordinary sensitive (< 50 nT $\mathrm{Hz}^{-1/2}$) organic thin film probe which uses the polarons gyromagnetic ratio γ as magnetic field standard. γ was observed to be independent of temperature, device-current, and -bias, and degradation of the MEH-PPV device. In addition to the PP mechanism, another spin-dependent process previously described in the literature was confirmed to significantly influence conductivity in MEH-PPV: Triplet-exciton polaron recombination.

To my wife Emily

CONTENTS

ABSTRACT . . . . . **iii**

LIST OF FIGURES . . . . . **viii**

ACKNOWLEDGMENTS . . . . . **x**

CHAPTERS

1. INTRODUCTION **1**

1.1 History 1
1.2 Organic spintronics: state of the field 4
1.3 Material background 5
1.3.1 Chemical bonding in π-conjugated polymers 6
1.3.2 Charge carrier pairs 6
1.4 Questions addressed in this thesis 7
1.5 References 9

2. PEDMR ON ORGANIC SEMICONDUCTOR DEVICES **12**

2.1 Experimental foundations of pEDMR 12
2.2 The technical implementation of pEDMR spectroscopy on carbon-based materials 13
2.2.1 Challenges 13
2.2.2 pEDMR compatible thin film templates 14
2.2.3 Device fabrication details 16
2.2.4 pEDMR compatible organic semiconductor samples and devices 20
2.2.5 The spectroscopy setup (X-band) 20
2.2.5.1 Current after magnetic resonant excitation 21
2.2.6 Coherent control of device current 22
2.3 Rabi-nutation mapping and simulation: confirmation of weakly coupled pair 26
2.4 Discussion 28
2.5 References 30

3. HYPERFINE-FIELD-MEDIATED SPIN BEATING IN ELECTROSTATICALLY BOUND CHARGE CARRIER PAIRS **31**

3.1 Hyperfine fields in organic semiconductors 32
3.2 Experiment 33

3.2.1 Weakly coupled pair . . . 33
3.2.2 Using spin beating to determine average hyperfine strength . . . 36
3.3 Conclusion . . . 40
3.4 References . . . 42

4. TRIPLET EXCITON-POLARON RECOMBINATION IN MEH-PPV . . . 44

4.1 Models for spin-dependent processes in organic semiconductors . . . 45
4.2 Experiment . . . 46
4.2.1 Devices: balanced and imbalanced injection . . . 46
4.2.2 Multiple spin–dependent channels . . . 50
4.2.3 Coherent "Rabi–beating" spectroscopy . . . 52
4.2.4 Half–field excitonic resonance . . . 55
4.3 Exclusion of models . . . 57
4.3.1 Single spin 1/2 process . . . 58
4.3.2 Second PP process with different dynamics . . . 59
4.3.3 Bipolaron . . . 59
4.3.4 Trion recombination . . . 60
4.3.5 Triplet-triplet exciton annihilation . . . 60
4.3.6 Triplet-exciton polaron(TEP) . . . 61
4.4 Conclusions . . . 61
4.5 References . . . 63

5. SLOW HOPPING AND SPIN-DEPHASING OF COULOMBICALLY BOUND POLARON PAIRS IN AN ORGANIC SEMICONDUCTOR AT ROOM TEMPERATURE . . . 65

5.1 Electrically detected Hahn echoes . . . 66
5.2 Decoherence mechanism . . . 68
5.3 Simulation of hopping pairs . . . 70
5.4 Discussion . . . 74
5.5 References . . . 76

6. ROBUST ABSOLUTE MAGNETOMETRY WITH ORGANIC THIN-FILM DEVICES . . . 78

6.1 Traditional magnetometry approaches . . . 79
6.2 Results . . . 81
6.2.1 Resonant current change mechanism . . . 81
6.2.2 Field sensing: precision and stability . . . 85
6.2.3 An integrated magnetic resonance-based organic magnetometer . . . 89
6.3 Discussion . . . 91
6.4 Methods . . . 93

6.4.1 Device fabrication 93
6.4.2 Experimental setup 93
6.4.3 Sensitivity analysis 94
6.5 References 95

7. SUMMARY AND OUTLOOK 98

7.1 List of publications 100
7.2 Pending manuscripts 101

APPENDIX: LOW-FIELD METHODS 102

LIST OF FIGURES

2.1 Illustration of an organic semiconductor sample which is prepared on a pEDMR compatible sample template as it is placed within a cylindrical microwave resonator. 15

2.2 A scanning electron microscope (SEM) image of a factory polished ITO films. 17

2.3 Photo of an MEH-PPV based OLED device fabricated on a pEDMR sample template. 21

2.4 Plot of the current change ΔI in a MEH-PPV OLED after a short microwave pulse as a function of time and the magnetic field B_0. 23

2.5 The integrated current after a coherent microwave pulse, measured as a function of the pulse length. 25

2.6 Rabi frequency detuning of coherent spin dynamics of weakly-coupled carrier pairs in an OLED at room temperature. 27

3.1 Observation of the two spin partners in an electrostatically bound carrier pair in an OLED. 35

3.2 Coherent oscillations of the ensemble of spin pairs, observed by measuring the change in OLED current. 37

3.3 Beating of spin precession following compensation of the difference in intrapair hyperfine fields. 39

4.1 IV curves of both balanced and electron-rich devices. 47

4.2 X-band EDMR of OLEDs with carrier balance and electron preference. 49

4.3 Transient EDMR spectra at different times after spin-resonant excitation at 10 K. 51

4.4 Rabi flopping in the current of an electron-dominated device at 10 K. . 54

4.5 Spin-1 (triplet) half-field Rabi flopping in the electron-rich device. 56

5.1 Illustration of hopping induced decoherence mechanism during a Hahn-echo sequence. 67

5.2 Experimentally observed magnetic resonance spectrum and spin echoes. 71

5.3 Computational modeling of the expected echo decay time T_2^{Sim} as a function of polaron hopping time for an ensemble of polaron pairs. 73

6.1 Device concept of an organic semiconductor magnetic resonance based magnetometer (MRM). 80

6.2 Device concept of an organic semiconductor magnetic resonance based magnetometer (MRM). 82
6.3 Calibration of the MR magnetometer. 84
6.4 Robustness and sensitivity limits of the magnetometer device. 87
6.5 An integrated absolute magnetic field sensor. 90
A.1 The setup used in the magnetoresistance (OMAR) measurements. 102
A.2 The low-field pulsed EDMR setup. 103
A.3 The magnetic field sensor configuration. 105
A.4 An example of frequency sweep experiment carried out with the all-coil configuration. 106
A.5 A diagram explaining the components of the all-coil low field resonator. 108
A.6 A collection of Rabi-nutations using the all coil configuration. 109
A.7 A diagram explaining the components of the all-stripline low field resonator. 110
A.8 A single Rabi-nutation experiment at 0db using the all stripline configuration. 111

ACKNOWLEDGMENTS

The process of gaining my PhD has really been an interesting experience. This has been directly related to the individuals with whom I have had the opportunity of working. They have all been world class, and I would like to acknowledge them.

I want to thank my advisor Christoph Boehme for giving me a chance to do such interesting work and for always being available for discussions. On many occasions your insight has been the reason for the quick development of my research, and your knowledge and quick recall have led to a very interesting environment to work in. Thanks for humoring my sometimes silly hypotheses and fostering an open mind environment. I have learned how important keeping an open door is to the progression of a project, and I hope to continue to remain friends and collaborators.

I would also like to thank John Lupton for the opportunity to discover new physics in such a rich and interesting field of study. I have benefited from your attention to detail and your broad scope of understanding. Thank you for always being so upfront and realistic with opinion.

I next would like to thank Dane McCamey for taking the time to walk me through the basics, sometimes with many iterations. I understand now how hard it can be, and very time consuming, to show a new PhD student the ropes and it will forever be remembered. The things I cherish most are some of the off-the-cuff conversations in your office when I am sure you were busy with something else. Your patience and expertise are recognized every time we have a discussion. I feel so lucky to have arrived when I did to the group. To have you around was like having a second advisor next to Christoph.

I would like to thank everyone in the Lupton group for your input and suggestions. Thanks Nick Borys for always being available for some computer related issue, and for some good discussions. Thanks Kipp van Schooten and Alex Thiessen, for all the

results here were highly dependent on the operation of the chemical labs including the glovebox, and its the expertise and attention to detail of Kipp and Alex that has made this lab stand out as a very functional fabrication facility.

Thanks to all the family who has been there for support.

CHAPTER 1

INTRODUCTION

This first chapter of this dissertation will give an outline of the field of organic semiconductors in the context of spin-effects and spintronics. The history behind this development will be discussed and the group of, arguably, the most important experimental methods. This is the method of electron spin resonance (ESR) spectroscopy and in particular the derived method of electrically detected magnetic resonance (EDMR). A special emphasis in this regard is given to the coherent time domain EDMR, the so called pulsed (pEDMR) spectroscopy, which has been developed in the past 10 years. During this time, pEDMR has led to many new insights into the quantum nature of paramagnetic states which can influence conductivity. Finally, a brief overview about the following chapters is given, which will bring the individual studies contained in this dissertation into a general context of organic spintronics.

Some of the following sections are reprinted from a publication *Physica.Stat.Solidi* B[1] coauthored by Christoph Boehme, Dane McCamey, Kipp van Shooten, Sang-Yun Lee, Seo-young Paik, and John Lupton who shall be acknowledged here.

1.1 History

Spin selection rules on electronic transitions play a profoundly important role for the electrical and optical properties of materials with weak spin-orbit coupling. Because of this, the understanding of photo- or dark-conductivity in low atomic order semiconductors such as silicon or carbon requires appreciation of the qualitative and quantitative nature of paramagnetic centers involved in charge carrier

[1] C. Boehme, McCamey, D. R. and van Schooten, K. J. and Baker, W. J. and Lee, S.-Y., Paik, S.-Y., Lupton, J. M. , Phys. Status Solidi B 246, 2750 (2009). Copyright 2009 by the John Wiley and Sons, Inc., reprinted with permission from John Wiley and Sons, Inc.

transport and recombination. Paramagnetic centers in condensed matter have been investigated for decades with conventional ESR and nuclear magnetic resonance (NMR) spectroscopies. However, for carbon-based materials, the benefits of these methods for the understanding of spin-dependent processes have oftentimes been constrained due to (i) sensitivity limitations of these volume-sensitive methods which prevent the detection of highly diluted centers or centers in low dimensional (e.g., thin film) materials, (ii) the indistinguishability of paramagnetic defects which influence conductivity from those which are not relevant, and (iii) the lack of information that is obtained about the way these centers are involved in electronic transitions. Because of these limitations, electrically and optically detected magnetic resonance spectroscopies (EDMR and ODMR, respectively) have been widely used for the investigation of spin-dependent transitions in carbon-based materials [1–6]. Both ODMR and EDMR are based on the indirect detection of magnetic resonance through detection of electronic transitions (fluorescence and phosphorescence for ODMR, recombination or transport for EDMR) that depend on the electronic spin states manipulated with ESR. This indirect detection scheme overcomes size limitations since detection of even single photons is straightforward at infrared or shorter wavelengths, and because individual charge detection is technically possible as well. Both ODMR [7, 8] and EDMR [9] have been demonstrated to be sensitive to single spins. For the investigation of how paramagnetic centers affect optical or electrical properties, ODMR and EDMR are also advantageous since they detect only the paramagnetic centers of interest - those spins that are not part of spin-dependent transitions will remain invisible for these methods.

Traditionally, ESR, ODMR, and EDMR have been carried out as continuous wave (cw) experiments where the observables (microwave radiation, infrared or shorter wavelength light, and conductivity, respectively) are monitored as a function of an applied magnetic field B_0 that is swept adiabatically while the sample is continuously exposed to microwave irradiation with constant frequency and intensity [10]. This approach is simple, but the information obtained from the cw spectra is limited to Landé-(g)-factors and strongly convoluted spin-relaxation-, coupling-, and electronic

lifetime-parameters which determine the lineshapes and linewidths of the resonances. Because of the limitations of cw-ESR and cw-ODMR, much effort has been invested into the development of ESR [11] and ODMR spectroscopy [12] in the coherent time domain where the quantum mechanical propagation of the spins during a short pulsed resonant excitation is observed, providing a significantly enhanced set of qualitative and quantitative parameters about the investigated spin [11]. PESR [11] and pODMR [12] have been performed since the 1970s following the earlier development of pNMR in the 1950s, a method that to date is performed almost exclusively in the coherent time domain. In contrast, pEDMR, the direct electrical detection of coherent spin propagation, was not demonstrated until about a decade ago [13]. Many technical challenges prevented pEDMR experiments from being straightforward, such as the difficulty (a) to generate strong homogeneous electromagnetic pulses (the B_1 field) around electrically conductive semiconductor samples and devices [14], (b) to prevent the conducting samples from absorbing the B_1 field (antenna effect) which produces strong perturbing currents, and (c) to measure the oftentimes subtle spin-dependent current on top of strong spin-independent current offsets at a time resolution that is appropriate for the observation of coherent spin motion [15]. It was especially (c), which prevented the electrical detection of coherent spin motion until an indirect spin-pump current-probe measurement scheme for pEDMR was demonstrated in 2002, which allowed the observation of electrically detected rotary echoes in hydrogenated microcrystalline silicon [16]. Since this first demonstration of the electrical detection of electronic spin coherence, a broad range of previously developed pESR pulse sequences have been demonstrated as identical or similar pEDMR experiments. Among those are spin-Rabi nutation experiments which have since their first demonstration [17] been used for the investigation of exchange (J) [18], dipolar (D) [19], and hyperfine (A) [20] coupling strength within pairs of paramagnetic states; Hahn echo experiments for the investigation of transverse spin relaxation times (T_2) [21, 22]; and inversion recovery experiments for the investigation of longitudinal spin relaxation times (T_1) [23]. Most of the pEDMR experiments to date have been performed on inorganic semiconductors such as silicon in various morphologies

(amorphous [24,25], microcrystalline [26], monocrystalline [20,22], and combinations thereof). Given this extensive work and the equally extensive tradition of cw EDMR measurements on carbon-based semiconductors, which have revealed the existence of many spin–dependent processes which affect fluorescence and conductivity, it is clear that pEDMR on the latter materials holds much promise for new insights and discoveries. This is why the application of pEDMR to carbon-based materials, especially organic semiconductors, has been undertaken in recent years [5,18,27,28].

1.2 Organic spintronics: state of the field

Organic spintronics is a currently emerging research field that focuses on the exploration of spin effects in organic semiconductors. One of the research activities aims at utilizing the low spin-orbital coupling within these materials which are based mostly on elements with low Z-numbers. Since spin-orbit interaction is low, spin relaxation times can be long, possibly long enough to store information in spin manifolds and to transport spin information over sufficiently long distances. However, while spin-orbit is truly low in many organic semiconductors, other major issues affecting the transport of polarized spin currents across distances of more than just a few nanometers have evolved (e.g., strong hyperfine fields, low carrier mobilities, transport through localized states and disorder). In spite of the successful demonstrating of spin-valves, no successful Hanle experiment confirming the existence of long range ballistic spin transport has been demonstrated yet. It seems that the spin information of charge carriers is lost, possibly due to slow hopping between random localized states which are exposed to different, random hyperfine environments (see the discussion of hyperfine fields in Chapter 5).

The beginning of what is referred to as "organic spintronics" goes back to the first organic spin valve (SV) [29] demonstrated about a decade ago. An organic SV consists of an organic semiconductor layer sandwiched between two ferromagnetic injection layers with different coercive fields. Depending on the relative polarization orientation of the two ferromagnetic layers, a charge current is higher or lower. Thus, the organic SV is a spin-sensitive switch. When the device is placed in an external field, the

injector and collector directions will have either aligned, or anti-aligned directions and thus have low or high resistance accordingly. As known from inorganic SVs, organic SVs, show a coercive field depends magnetoresistance. However, as organic SVs have failed to exhibit the Hanle effect (This effect corresponds to a Larmor precession dependent current when a magnetic field perpendicular to the carrier propagation is applied), it is still highly elusive whether spin transport occurs in these devices or whether the observed magnetoresistance is due other spin-dependent phenomena such as spin-dependent electronic interface transitions.

Another intensively investigated "organic spintronic" effect is the intrinsic magnetoresistance of organic semiconductors in absence of spin polarized injection layers, referred to as organic magnetoresistance (OMAR) [30]. Many studies have been conducted on this effect [30–36], although much of the work has been based on experiments which solely aimed at the study of macroscopic materials behavior (plain measurements of conductivity effects without directly control of the current by controlled spins states) which oftentimes has led to ambiguous results and resulting controversy [30, 35, 37, 38]. As a consequence, a proliferation of microscopic models has taken place [35, 39, 40] which all fit experimental observations. The OMAR effect has been revisited in this thesis, in particular in Chapter 6.

1.3 Material background

The material used and investigated in the following chapters is a conducting organic polymer poly[2-methoxy-5-(2'-ethyl-hexyloxy)-1,4-phenylene vinylene (MEH-PPV) that is a very well studied and documented [27,30,41,42]. MEH-PPV is a PPV derivative with a side group to facilitate dissolution in many solvents like toluene and chlorobenzene. This is important for the uniformity of a spincoated thin film as needed for OLED and organic solar cell applications. With sufficient molecular densities, a film created after spincoating will be tightly packed in a three dimensional bulk consisting of a disordered collection of entangled molecular chains. It is in this disordered spaghetti-like bulk where injected excitations (charge carrier) will interact, form pairs, and recombine.

1.3.1 Chemical bonding in π-conjugated polymers

Excitations injected into π-conjugated polymers are called polarons due to the bonding distortions which are caused by their presence. They occupy states created from the conjugation through the π-bonds resulting from the p_z orbitals which come from of the sp^2 hybridization of the carbon atoms [42] in the polymer chain. Π-conjugation leads to distended and delocalized orbitals that overlap many repeat units within a given molecular chain. The lowest energetic excitations in π-conjugated polymers are $\pi - \pi^*$ transitions, which are usually between energies of 1.5ev and 3ev. This energy range therefore leads to absorption and emission of visible light, which one reason why these materials are of importance for optoelectronics and photovoltaics. Interaction between molecular chains are predominantly very weak van der Waals forces. Because of this, a "phonon dressing" of injected electrons and holes can take place and due to Coulomb interaction, a distortion of the local bonding environment is possible. It is this what leads to the appearance of polaronic states. Hole polarons and electron polarons will fill the highest occupied molecular orbitals (HOMO) and lowest unoccupied molecular orbitals (LUMO) states, respectively, and as such, the two entities can effectively interact on lengths scales of a few chain segments. In this dissertation, this will become important for the interpretation of electrically detected magntic resonance line widths.

1.3.2 Charge carrier pairs

The intrinsic carrier densities in a material such as MEH-PPV can be as low as 1cm^{-3} [43] in absence of intrinsic doping as known from conventional inorganic semiconductors like silicon. However, doping can effectively be introduced via electrical injection from electrical contacts which can lead to charge carrier densities above 10^{10} - 10^{15}cm^{-3} [43]. Because of the high degree of disorder in the bulk, injected polarons can undergo a thermally driven hopping transport since eigenenergies of polarons are broadly Gaussian distributed of around the HOMO and LUMO levels [42]. Polaron mobilities under such conditions are usually below $10^{-3}\text{cm}^2/\text{Vs}$ [43]. This is in stark contrast to charge carrier mobilities in inorganic semiconductors which can be many

orders of magnitude higher (e.g., crystalline silicon: $\sim 100\text{cm}^2/\text{Vs}$). Electron and hole polarons can interact with other charge carriers, in particular those with opposite charge. Due to the microscopic morphology of π-conjugated materials, this interactions typically takes place cross neighboring molecular chains through Coulombic forces. Once an electron polaron and a hole polaron encounter each other below the Onsager radius (= the distance where the Coulomb attraction exceeds the thermal energy), they can form a Coulombically bound polaron pair [42]. While polaron pairs consisting of two polarons located on adjacent molecular chains are weakly spin-exchange and spin-dipolar coupled, they can undergo electronic transitions into pairs states localized on one molecular chain. Once such a transition occurs, the polaron pair the spin interaction within the pair strongly increases (due to enlarged exchange splitting of as much as 0.7eV to 1eV) and an excitonic state is formed.

1.4 Questions addressed in this thesis

In essence, this thesis consists a series of studies conducted on a prototypical organic semiconductor, the π-conjugated MEH-PPV. Each of these studies is described in each of the following five chapters. In the following, brief summaries of these studies are presented in order to describe how their logical succession allowed each new chapter to built on the results of the previous chapters and how the comprehensiveness of all this work led to the evolution of a new understanding of spin-dependent processes in MEH-PPV in particular and organic semiconductors in general.

Chapter 2 — PEDMR is the most important experimental technique for the studies presented in this dissertation. A thorough discussion of pEDMR, related methods, its capabilities and limitations as well as technical aspects will therefore be the subject of Chapter 2. Also, the fundamental physical effects which can be observed with pEDMR, namely, magnetic resonantly induced coherent spin motion will be shown.

Chapter 3 — This chapter is focused on the use of pEDMR for the investigation of hyperfine field effects on the PP mechanism in MEH-PPV OLEDs under biplolar

injection. The chapter will address questions such as how resonantly induced spin-Rabi beat oscillation can be used for the precise measurement of hyperfine fields and whether hyperfine fields can vary within individual PPs.

Chapter 4 — After the experimental confirmation of the PP process in Chapters 2 and 3, the question of other spin-dependent processes in MEH-PPV as described in the literature, is discussed. Experiments similar to those described in Chapter 3 were repeated on devices with different charge carrier injection conditions, namely, imbalanced bipolar injection with either electron polarons or hole polarons as majority carriers. The results of these experiments have helped to confirm but also refute some of the hypothetical spin-dependent mechanism found in the literature.

Chapter 5 — After showing how to experimentally distinguish the PP mechanism from other spin-dependent processes, the measurement of transverse and longitudinal spin relaxation times as function of the injection current and temperature is presented. First electrically detected Hahn–echo experiments on organic semiconductors are presented. Based on these observations, hypothesis for spin–coherence limiting processes (phonon scattering, spin-spin interactions, charge carrier hopping) will be discussed and scrutinized by further experiments. The results of this study has been of significance in particular in context of whether electronic spin states in organic semiconductors are suitable for spin-information and spin-quantum information applications.

Chapter 6 — Finally, the last chapter will focus on a technical application (a new organic spintronics device) of the PP process. It is suggested to use an OLED thin film device in order to carry out magnetometry based on magnetic resonantly induced electric currents. This organic magnetic resonant magnetometer (OMRM) uses the gyromagnetic ratio of polarons as magnetic field standard. It is shown that this gyromagnetic ratio is a true constant as it is very robust under changing device conditions. This allows organic diodes to be used as calibration and degradation insensitive sensors.

1.5 References

[1] K. Murata et al., Chemical Physics **227**, 191 (1998).

[2] G. Silva, L. Santos, R. Faria, and C. Graeff, Physica B: Condensed Matter **308-310**, 1078 (2001).

[3] M.-K. Lee, M. Segal, Z. G. Soos, J. Shinar, and M. A. Baldo, Phys. Rev. Lett. **94**, 137403 (2005).

[4] M. Segal et al., Nat Mater **6**, 374 (2007).

[5] W. Harneit et al., Phys. Rev. Lett. **98**, 216601 (2007).

[6] C. G. Yang, E. Ehrenfreund, F. Wang, T. Drori, and Z. V. Vardeny, Phys. Rev. B **78**, 205312 (2008).

[7] J. Kohler et al., Nature **363**, 242 (1993).

[8] J. Wrachtrup, C. von Borczyskowski, J. Bernard, M. Orritt, and R. Brown, Nature **363**, 244 (1993).

[9] M. Xiao, I. Martin, E. Yablonovitch, and H. W. Jiang, Nature **430**, 435 (2004).

[10] J.-M. Spaeth and H. Overhof, 2003.

[11] A. Schweiger and G. Jeschke, 2001.

[12] D. J. Gravesteijn and M. Glasbeek, Phys. Rev. B **19**, 5549 (1979).

[13] C. Boehme and K. Lips, Appl. Phys. Lett. **79**, 4363 (2001).

[14] C. Boehme and K. Lips, Phys. Rev. Lett. **91**, 246603 (2003).

[15] C. Boehme and K. Lips, Phys. Rev. B **68**, 245105 (2003).

[16] C. Boehme and K. Lips, phys. stat. sol. (b) **233**, 427 (2002).

[17] C. Boehme and K. Lips, 2006.

[18] S. Schaefer et al., phys. stat. sol. (b) **245**, 2120 (2008).

[19] K. Lips, C. Boehme, and T. Ehara, The impact of the electron spin on charge carrier recombination - the example of amorphous silicon, 2005.

[20] A. R. Stegner et al., Nat Phys **2**, 835 (2006).

[21] H. Huebl et al., Phys. Rev. Lett. **100**, 177602 (2008).

[22] G. W. Morley et al., Phys. Rev. Lett. **101**, 207602 (2008).

[23] S.-Y. Paik, S.-Y. Lee, W. J. Baker, D. R. McCamey, and C. Boehme, Phys. Rev. B **81**, 075214 (2010).

[24] K. Lips and C. Boehme, Recombination echoes in disordered silicon, 2003-10-01.

[25] T. W. Herring et al., Phys. Rev. B **79**, 195205 (2009).

[26] J. Behrends et al., Journal of Non-Crystalline Solids **354**, 2411 (2008).

[27] D. R. McCamey et al., Nat Mater **7**, 723 (2008).

[28] E. Thomsen, 2008.

[29] Z. H. Xiong, D. Wu, Z. Valy Vardeny, and J. Shi, Nature **427**, 821 (2004).

[30] T. D. Nguyen et al., Nat Mater **9**, 345 (2010).

[31] T. S. Santos et al., Phys. Rev. Lett. **98**, 016601 (2007).

[32] L. Hueso, I. Bergenti, A. Riminucci, Y. Zhan, and V. Dediu, Adv. Mater. **19**, 2639 (2007).

[33] F. J. Wang, C. G. Yang, Z. V. Vardeny, and X. G. Li, Phys. Rev. B **75**, 245324 (2007).

[34] H. Vinzelberg et al., J. Appl. Phys. **103**, 093720 (2008).

[35] P. A. Bobbert, T. D. Nguyen, F. W. A. van Oost, B. Koopmans, and M. Wohlgenannt, Phys. Rev. Lett. **99**, 216801 (2007).

[36] Y. Sheng et al., Phys. Rev. B **74**, 045213 (2006).

[37] J. M. Lupton and C. Boehme, Nat Mater **7**, 598 (2008).

[38] W. J. Baker, D. R. McCamey, K. J. van Schooten, J. M. Lupton, and C. Boehme, Phys. Rev. B **84**, 165205 (2011).

[39] L. S. Swanson et al., Phys. Rev. B **46**, 15072 (1992).

[40] M. Wohlgenannt, W. Graupner, G. Leising, and Z. V. Vardeny, Phys. Rev. Lett. **82**, 3344 (1999).

[41] R. H. Friend et al., Nature **397**, 121 (1999).

[42] C. E. Pope, M. & Swenberg, *Electronic Processes in Organic Crystals and Polymers*, Clarendon, 1982.

[43] W. Brutting, Introduction to the physics of organic semiconductors, in *Physics of Organic Semiconductors*, pages 1–14, Wiley-VCH Verlag GmbH & Co. KGaA, 2006.

CHAPTER 2

PEDMR ON ORGANIC SEMICONDUCTOR DEVICES

In this chapter the sample design, the experimental setup and the execution of pEDMR measurements will discussed. The experiments covered in this chapter were the basis for most experiments described in the following chapters. The rigorous theoretical foundations of pEDMR spectroscopy will not be discussed here, many other publications have dealt with this topic [1–5] over the past ten years. Some of the following sections are reprinted from a publication *Physica.Stat.Solidi B*[1] coauthored by Christoph Boehme, Dane McCamey, Kipp van Shooten, Sang-Yun Lee, Seo-young Paik, and John Lupton who shall be acknowledged here.

2.1 Experimental foundations of pEDMR

Carbon-based materials have an intrinsically weak spin-orbit coupling which imposes spin selection rules on many electronic transitions. The spin degree of freedom of electrons and nuclei can therefore play a crucial role in the electronic and optical properties of these materials. Spin-selection rules can be studied via magnetic resonance techniques such as electron-spin resonance and optically detected magnetic resonance as well as electrically detected magnetic resonance (EDMR). The latter has progressed in recent years to a degree where the observation of coherent spin motion via current detection has become possible, providing experimental access to many new insights into the role that paramagnetic centers play for conductivity and photoconductivity. While mostly applied to inorganic semiconductor materials

[1] C. Boehme, McCamey, D. R. and van Schooten, K. J. and Baker, W. J. and Lee, S.-Y., Paik, S.-Y., Lupton, J. M. , Phys. Status Solidi B 246, 2750 (2009). Copyright 2009 by the John Wiley and Sons, Inc., reprinted with permission from John Wiley and Sons, Inc.

such as silicon, this new, often called pulsed-(p) EDMR spectroscopy, has much potential for organic (carbon-based) semiconductors. In this study, progress on the development of pEDMR spectroscopy on carbon-based materials is reviewed. Insights into materials properties that can be gained from pEDMR experiments are explained and limitations are discussed. Experimental data on radiative polaron-pair recombination in poly[2-methoxy-5-(2'-ethyl-hexyloxy)-1,4- phenylene vinylene] (MEH-PPV) organic light emitting diodes (OLEDs) are shown, revealing that under operating conditions the driving current of the device can be modulated by spin-Rabi nutation of the polaron spin within the charge carrier pairs. From this experimental data it becomes clear that for polaron pairs, the precursor states during exciton formation, exchange interaction is not the predominant influence on the observed pEDMR spectra.

2.2 The technical implementation of pEDMR spectroscopy on carbon-based materials

2.2.1 Challenges

As for pEDMR with inorganic semiconductor materials, organic materials must be contacted in a way that the contacts do not distort and inhomogenize the B_1 fields needed for the spin manipulation. For silicon samples, this problem has been solved through the use of geometrically well-defined contact designs which can be implemented via photolithography [6]. Using the same approach for carbon-based semiconductors is difficult since carbon-based semiconductors are often prepared in inert atmospheres (glove boxes) where the application of photolithography is impractical. One solution to this problem is the use of shadow masks. However, the latter is technically demanding as well, for it provides poor structural resolution and is inapplicable to the vertical sample device structures described in the following. Since these structures contain inorganic dielectric isolation layers made out of silicon nitride, they cannot be deposited in a glove box environment. Another challenge for the pEDMR sample preparation is to quickly prepare samples with great reliability and reproducibility. Note that due to the extreme sensitivity of many carbon-based semiconductors to ambient air, the sample structure should provide best possible

encapsulation of the sample materials and at the same time, the sample preparation process should be quick and easy so that the sample preparation does not become the bottle neck for the measurement process. Finally, the sample preparation should be versatile enough so that different materials and material combinations can be subjected to the measurements without the need for a new sample design and the associated time consumption for sample development and implementation. As pEDMR spectroscopy has proven to be particularly insightful when conducted on devices such as light-emitting diodes or solar cells under operation conditions [7], the sample design should allow the implementation of organic solar cells or organic light-emitting diodes.

2.2.2 pEDMR compatible thin film templates

The requirements for pEDMR measurements on carbon materials described in Section 2.2.1 can be met by using photolithographically prepared templates for the sample preparation. The idea is to first carry out all lithography steps using materials which do not need to be confined to a glove box before the sensitive materials are prepared.

Figure 2.1 illustrates the structure of such a sample which is deposited on a sample template designed for a cylindrical resonator, such as the commercially available dielectric Bruker Flexline resonators. The sketch shows that the sample consists of a long matchstick-like substrate. On one end of the substrate, two contacts are positioned well outside the resonator volume. They are connected via two thin film wires with the sample area on the other end which is located at the resonator center where B_1 fields are maximal and homogeneous. The connecting thin film wires are made thin enough ($\sim$50 - 100nm) to leave the microwave radiation mostly unperturbed. Note that due to the low mobility of organic semiconductors, most samples and devices will require a current path perpendicular to the substrate surface. The template illustrated in Fig. 2.1 allows such vertical contacting due to the presence of an insulating dielectric layer (silicon nitride or hard-baked photoresist) which covers the thin film wiring except for four windows at the two contact pads, the sample area, and a via which is located close to the middle of the long substrate. In the following,

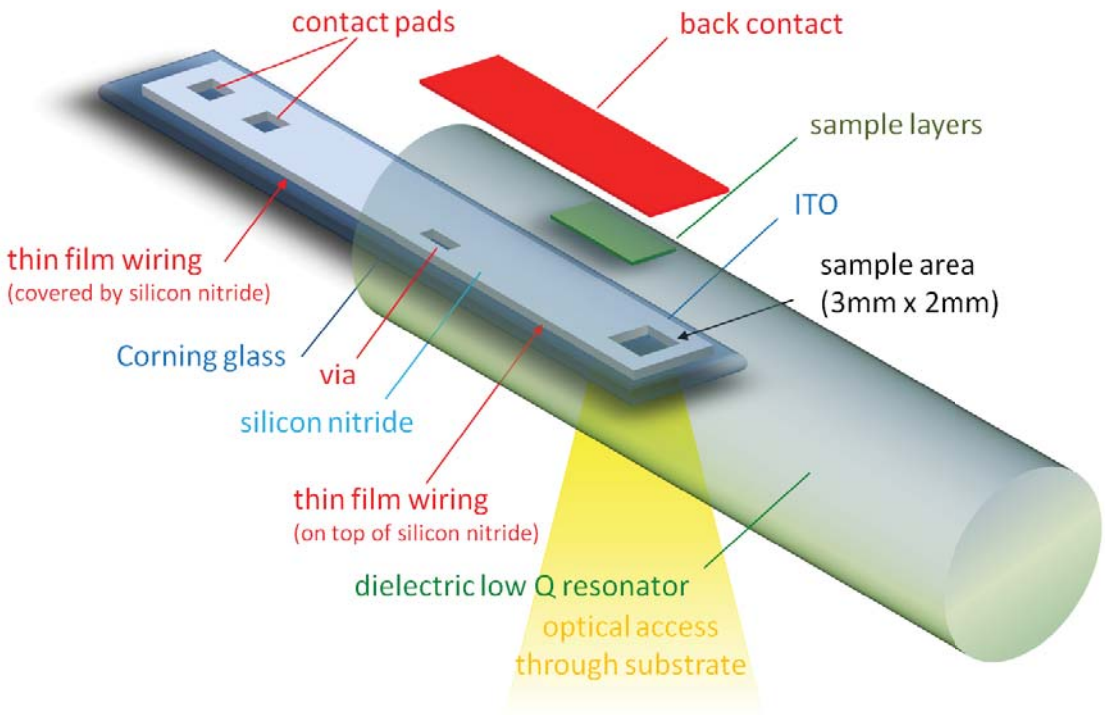

Figure 2.1. Illustration of an organic semiconductor sample which is prepared on a pEDMR compatible sample template as it is placed within a cylindrical microwave resonator. The sketch is not to scale. Adapted from [8].

the combination of the substrate, the thin film wiring as well as the patterned silicon nitride layer is referred to as the template. Templates can be made with simple clean room procedures quickly in large numbers and, as described in the following, these templates allow the implementation of a large variety of pEDMR compatible materials and sample devices without the need for additional lithography steps.

2.2.3 Device fabrication details

In the following, organic device components and it preparation methods are briefly described that have been used for the pEDMR experiments discussed in the following chapters.

Clean room — The preparation of organic layer devices for pEDMR measurements consists of two parts: (i) The clean room processing steps, and (ii) the glove box work. The clean room processes do not involve organic materials but metal and inorganic dielectrics. The main purpose is to lithographically define the geometry of the pEDMR devices, which will then later serve as template when the organic layers are deposited.

ITO — For the preparation of optoelectronic devices, transparent conducting materials are needed. There is a group of high bandgap, intrinsically n-doped oxides (zinc oxide, indium tin oxide [ITO]) which can be utilized for this purpose. For the experiments presented in this dissertation, ITO was used. The best approach to a smooth ITO film is using factory polished substrates, since self sputtered ITO without polish results in large "spikes" that can be more than 100nm high. Spiking can lead to electrical shorts through the organic layers. Even factory "polished" ITO can have large rough regions. In Fig. 2.2 are shown SEM images of different ITO active regions displaying different roughness.

Alignment markers — Alignment markers are used throughout the fabrication procedure in order to align subsequent masks in a very specific direction in order to create an electrical template. Alignment positions are set by photolithography using a UV lamp to expose spun-on photoresist. After a short bake of the photo resist at 100 degrees Celsius, the film is developed and metal is deposited using a sputtering setup. The thickness of metal layers were kept are approximately 100nm to survive

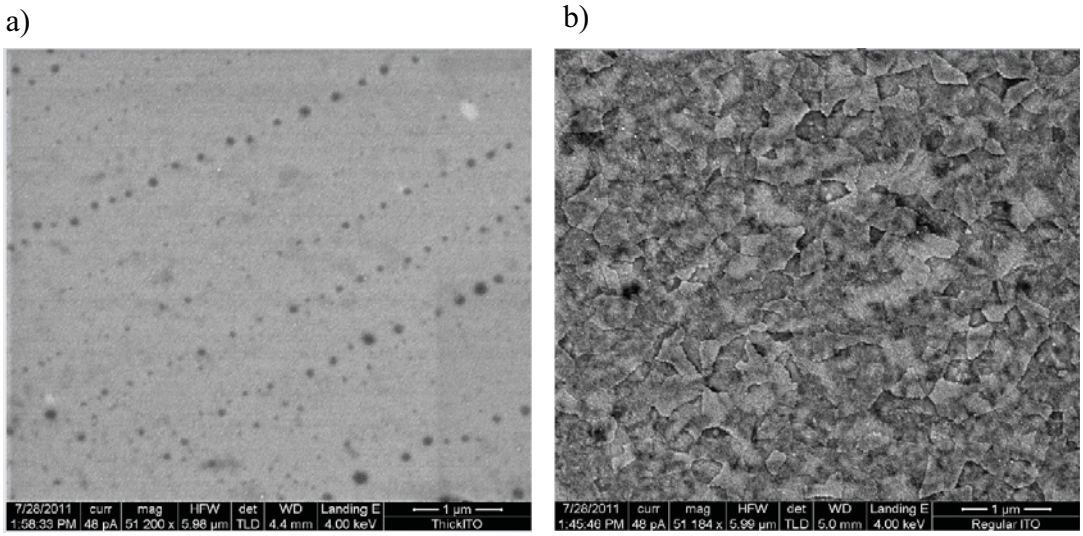

Figure 2.2. a) A scanning electron microscope (SEM) image of a factory polished ITO film showing a very uniform film which will not likely lead to many shorts after organic spin coating. b) An SEM image of a film from a company claiming to have polished the surface (Delta Industries). This film is much like what is expected from just sputtering ITO without polishing. The surface roughness can lead to electrical shorts through the organic layers that are spin coated above. Acknowledgment to Rachel Baarda for the images.

all etching steps.

Lift-off — A lift-off step is used in order to structure deposited metal layers. During liftoff the sample is placed in a sonicator (an acetone liquid bath which vibrates at ultrasound frequencies) for ≈ 10 minutes. This procedure removes all the photoresist and long with it, all metal that is deposited above photoresist structure. The remaining metal structures (including the alignment markers) are left on the previous device layer and can be further processes during additional photolithography steps or with reactive ion etch (RIE).

ITO etch — Once alignment markers are placed, the properly defined regions for the active ITO areas defined with an UV aligner. The samples are then placed in a RIE setup where the ITO is etched off except at the active device regions.

Thin-film wiring — Once the active ITO regions prepared, another photolithography step is used to define thin-film wiring on the device along with the contact pads and via. The templates are then placed in a sputtering setup where between 50 and 100nm of aluminum are deposited. This thickness is chosen to be much smaller than the penetration depth of the microwaves used in the X-band resonator, the electric wiring of the pEDMR device therefore becomes invisible to the microwave radiation.

Insulating layer — Next, a silicon nitride layer(50-100nm) is deposited with plasma enhanced chemical vapor deposition in order to isolate the thin-film wiring from shorting when the organic layer are deposited. Alternatively to the silicon nitride, one can also use other insulating layers such as hard-baked photoresist.

Hard-baking photoresist — In order to deposit the hard baked photoresist, a layer of 1813 PR is spin-coated at 3000rpm and placed on a hot plate for approximately 30 minutes. This will result in a solid insulating layer which will isolate the thin-film wiring and not disappear with the application of solvents during the cleaning process.

Silicon nitride etch — If silicon nitride is used as insulating layer, the contact, via and the active device regions must be cleared from the insulating material. This is done again by the RIE technique mentioned above.

Glovebox — Once the device template for pEDMR measurements is fabricated,

it is moved into a nitrogen atmosphere glovebox where the organic device layers are prepared. The first step of this active layer deposition process involves cleaning of the template surface. This is followed by the deposition of a first charge carrier injection layer.

Hole injection — For hole injection, a conducting material with high work–function is needed. Poly(3,4-ethylenedioxythiophene) [PEDOT] can be deposited on the cleaned ITO surface, a spin speed of 1000-3000rpm is used to deposit a thin layer of approximatly 50-100nm of material. The PEDOT requires baking at 100^{o}C for 10 minutes to extract any residual moisture.

Active stack deposition — After the charge carrier injection layer is deposited, the active device stack can be deposited. For OLEDs, a single material is used, for organic solar cells, blend materials or layer stacks are used. With MEH-PPV dissolved in toluene at approx. 7.5g/l, good results can be achieved with a spin speed of 1600rpm. The choice for a solvent and the spin speed are very important for the materials morphology, and therefore, the electrical of optical properties of the deposited material.

Electron injection — For electron injection, a conducting material with low work–function is needed. Examples include metals like Ca, Sr, Ba which can be deposited by thermal evaporation at low pressure (10^{-6}mBar). A thickness of 2nm is enough.

Encapsulation — After the back injector deposition, the entire active device region must be encapsulated in order to protect ex-situ penetration of oxygen. This is accomplished by evaporation of an aluminum layer that with a thickness of around 150-200nm. After this, the device can be encapsulated further by a two-part epoxy materials, which is applied to the active device region and baked to a required hardness on a hot plate. It is important to keep the baking temperature below the glass transition temperature of the used polymer material.

2.2.4 pEDMR compatible organic semiconductor samples and devices

To summarize the last section briefly, pEDMR compatible carbon samples can be implemented quickly using solely spincoating and metal evaporation. For spin-coating on the template, we built a template holder that fixes the long substrate in a position such that the rotation axis is close to its center. While spin coating does not produce laterally well defined layers, the area of the active sample will always be defined by the sample window dimensions in the silicon nitride layer. Stacks of material may be formed by additional spin coating steps. Once a desired material stack is prepared, the back contact of the sample is made via metal evaporation. The latter covers the entire substrate area except for a ∼1cm long region around the contact pads which are protected by a simple shadow mask during evaporation. Thus, by depositing the thin metal layer, the back contact of the material stack is connected through the via at the center of the template with one of the sample contacts. In addition to its contact properties, the metal cover also provides a simple encapsulation of the entire sample which preserves the sample stack during the transfer of the sample from the glove box into the microwave resonator. Figure 2.3a) displays a photo of a finished sample after it is installed in a pEDMR sample rod. The latter is a mechanical device that holds the sample in place when it is inserted into the resonator and at the same time provides electrical connection between the sample that is in the resonator (which in turn is placed in a sealed cryostat) and the outside of the cryostat. Figure 2.3 b) is a photo of an OLED based on an indium-tin-oxide (ITO) front contact, a poly(3,4-ethylenedioxythiophene) (PEDOT) hole injection layer as well as a poly[2-methoxy-5-(2'-ethyl-hexyloxy)- 1,4-phenylene vinylene] (MEH-PPV) layer under operating conditions. The orange light emission due to the currentinduced electroluminescence is clearly recognizable.

2.2.5 The spectroscopy setup (X-band)

For the demonstration of pEDMR measurements on the MEH-PPV OLED devices shown in Fig. 2.3 b), a) Bruker Elexsys E580 X-band (≈9.7GHz) pulsed ESR spectrometer, equipped with a 5mm flexline pulse resonator, was used.

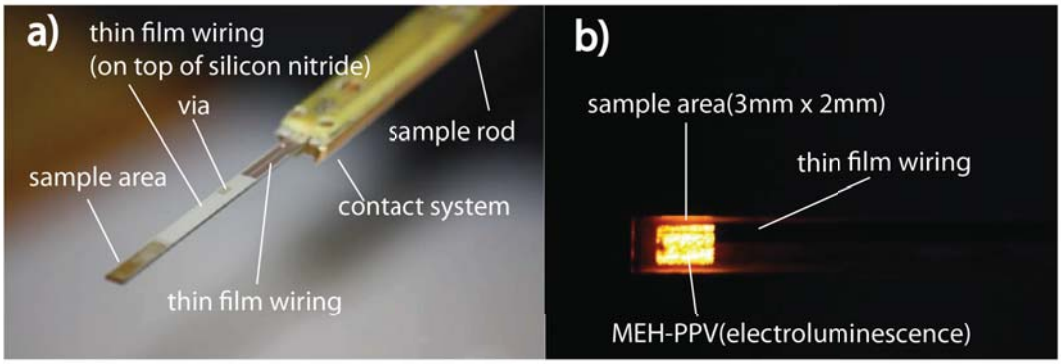

Figure 2.3. Photo of an MEH-PPV based OLED device fabricated on a pEDMR sample template as sketched in Fig. 2.1. The sample is held by a pEDMR sample rod with a built-in contact system for electrical connections. (b) Photo of the MEH-PPV OLED under operating conditions.

The device was brought to its operating point using a Keithley 2600 constant current source. For the current detection, a Stanford Research SR570 current amplifier was used whose output was connected to the input of the SpecJet transient recorder of the Elexsys spectrometer.

2.2.5.1 Current after magnetic resonant excitation

For a pEDMR experiment on the polaron pair mechanism in MEH-PPV, the presence of a spin-dependent current within the otherwise constant sample current must first be identified. This is done by time-resolved measurement of the sample current change from the steady state after a one-pulse excitation, repeated as a function of the magnetic field B_0. Figure 2.4a) displays a measurement conducted at T=300K and a current of I=100 μA. The two-dimensional data set represents the measured sample current change $\Delta I(t,\ B_0)$ after a microwave pulse with B_1=0.15mT was applied at t=0. The data show that around $B_0 \approx 344.7$mT there is a pronounced response which consists of a current quenching followed by a subsequent current enhancement. The decay of the resonantly changed sample current via two components with distinct time constants and opposite signs is well known from spin-dependent transitions between

spin-pairs [1] and the observation made here with MEH-PPV OLEDs under operating conditions confirms similar measurements in the photovoltaic mode [8]. The improved signal to noise ratio of the measurements presented here in comparison to Ref. [8] allows a closer look at the magnetic resonance line shape of this signal, which can be obtained from considering the B_0 dependence of the data in Fig. 2.4 a) for the time slice t=10.2μs where the current change reaches its maximum.

These data are equivalent to the information that would usually be obtained from cwEDMR experiments, and are displayed in the plots of Fig. 2.4 b) and c) which show the same experimental data sets but different fit functions. Figure 2.4 c) is a fit with one central Gaussian peak and two additional identical Gaussian peaks which are weaker in magnitude and equally separated from the center peak. This fit scenario describes the presence of significant exchange coupling within the polaron pairs and, in the past, it has been applied to the interpretation of organic EDMR spectra measured on zinc phthalocyanine devices [9] and fullerene C_{60} samples [10]. Figure 2.4 b) is a fit with two Gaussian lines that are centered about the same Landé-factor of $g \approx 2.003(1)$ but that have different widths. This fit scenario assumes small exchange within polaron pairs (so called distant pairs) but strong inhomogeneous line broadening which differs for the two pair partners. The fit ambiguity displayed for the data in Fig. 2.4 is an excellent example of the limitations of cw EDMR which solely provides line spectra with no or little [11] dynamic information.

2.2.6 Coherent control of device current

In order to get more insight into the nature of the underlying spin dependent channel of the data in Fig. 2.4, especially the question on whether intra-pair exchange coupling is the cause of the observed spectrum, we conducted Rabi spin nutation experiments. These experiments are based on the measurement of the integrated current change $Q(\tau) = \int \Delta I dt$ after a magnetic resonant pulse excitation as a function of the pulse length, τ, which reveals the nutation of the resonantly excited spin with spin-1/2 Rabi frequency $\Omega = \gamma B_1$ [1] where γ is the gyromagnetic ratio. Simulations of the pEDMR detected transient nutation have shown that the presence

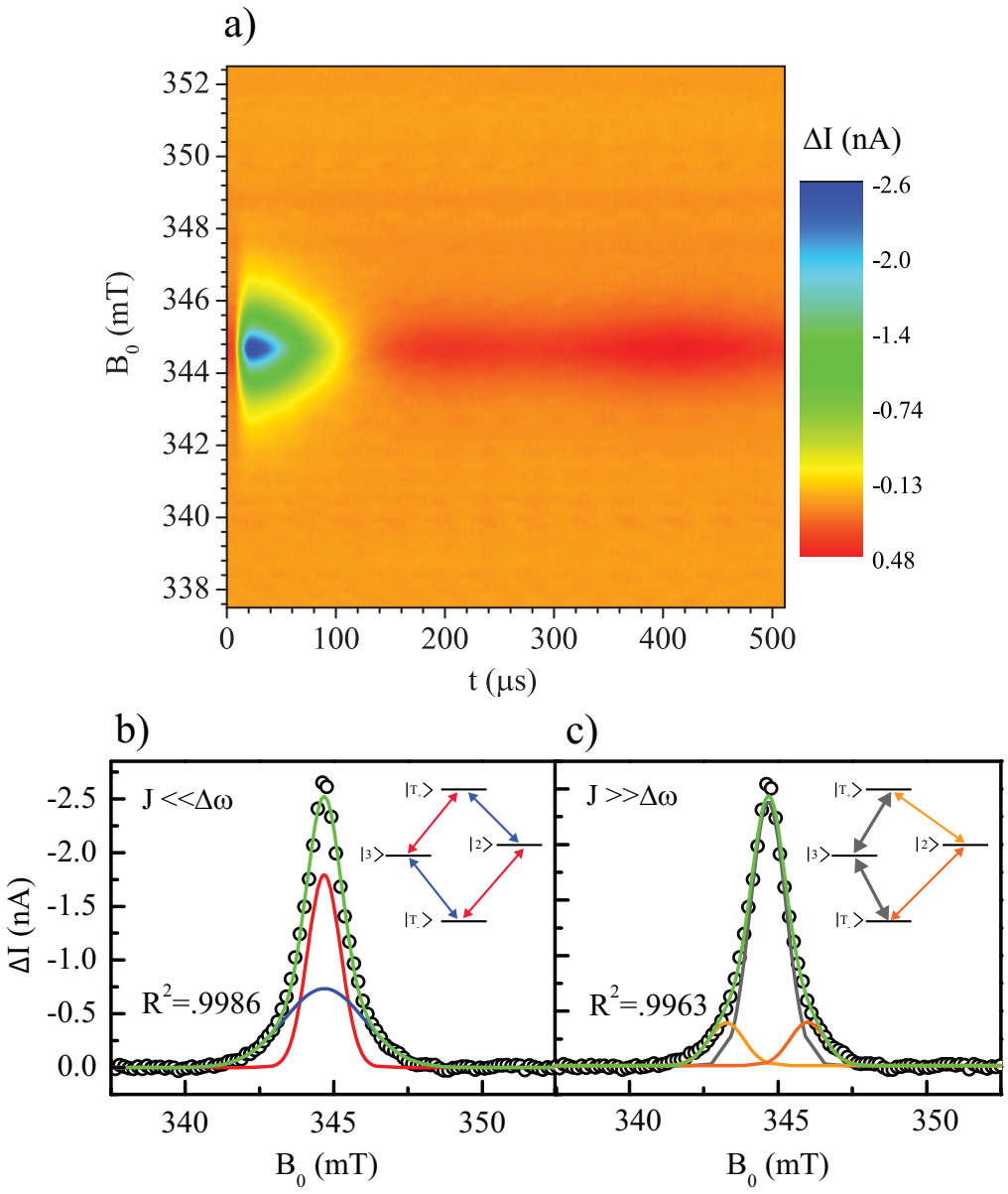

Figure 2.4. (a) Plot of the current change ΔI in a MEH-PPV OLED after a short microwave pulse as a function of time and the magnetic field B_0. The data show an initial strong quenching followed by a slowly decaying weak enhancement as expected for spin-dependent pair transitions (b,c): Plot of the B_0 dependent data shown in (a) for the time slice $t = 10.2\mu$s with two different fits for (b) significant exchange interaction within the pair and (c) for weakly coupled pairs with different inhomogeneous broadening as expected from hyperfine influences ($T = 300$K).

of significant exchange coupling ($J \gg \hbar\Delta\omega$, with $\Delta\omega$ being the Larmor frequency difference within the pair) leads to the appearance of a second nutation component with $\Omega = 2\gamma B_1$ due to the beat oscillation of the excited spin with its exchange coupled pair partner [2] while the $\Omega = \gamma B_1$ spin-1/2 nutation component disappears (becomes much weaker). Note that the double frequency component in the Rabi oscillation observed in a zinc phthalocyanine device has previously been attributed to this effect [9]. The simulations [2] predict that the beat oscillation component is observable independently of the strength of B_1 as long as the Larmor separation within the precursor pairs $\Delta\omega$ is smaller than the exchange interaction ($\hbar\Delta\omega \ll J$). However, a nutation beat oscillation can also occur when exchange is absent but $\gamma B_1 \gg \Delta\omega$ [3]. Thus, a verification or exclusion of the exchange hypothesis should be possible by measurement of pEDMR detected Rabi oscillation components at B_1 fields that are weaker than the $J \approx 1.3$mT coupling that could be inferred from the spectra of Fig. 2.4. While the dominating presence of the beat nutation may or may not be due to the presence of exchange interaction, the absence is clear proof that exchange does not determine the observed spectrum. Following the previous demonstration of coherent spin control of a current of an MEH-PPV OLED in the photovoltaic mode [8] we conducted spin Rabi nutation experiments whose results are displayed in Fig. 2.5.

The experiment was carried out at B_1 fields ranging from .26mT to 1.46mT, verified by a control experiment using a weakly (10^{15} cm^{-3}) ^{31}P doped crystalline silicon (c-Si) sample as a spin label. The plots in the right panel Fig. 2.5 show the imprint of a spin nutation signal that can be described by either a single modified Bessel function [1] (uppermost scan), or shows the imprint of multiple beating spin nutation signals from the simultaneous rotation of single spin-1/2 and spin-1. In order to determine the oscillation components, a Fourier transform was carried out which is plotted in the left panel of Fig. 2.5. This frequency plot shows only a single frequency corresponding to the rotation of a single spin-1/2 particle, $\Omega \approx \gamma$ 0.26mT $\approx$ 7MHz at B_1=.26mT. At twice this values ($\approx$ 14MHz) there is a small local maximum, however, while this maximum cannot unambiguously be identified

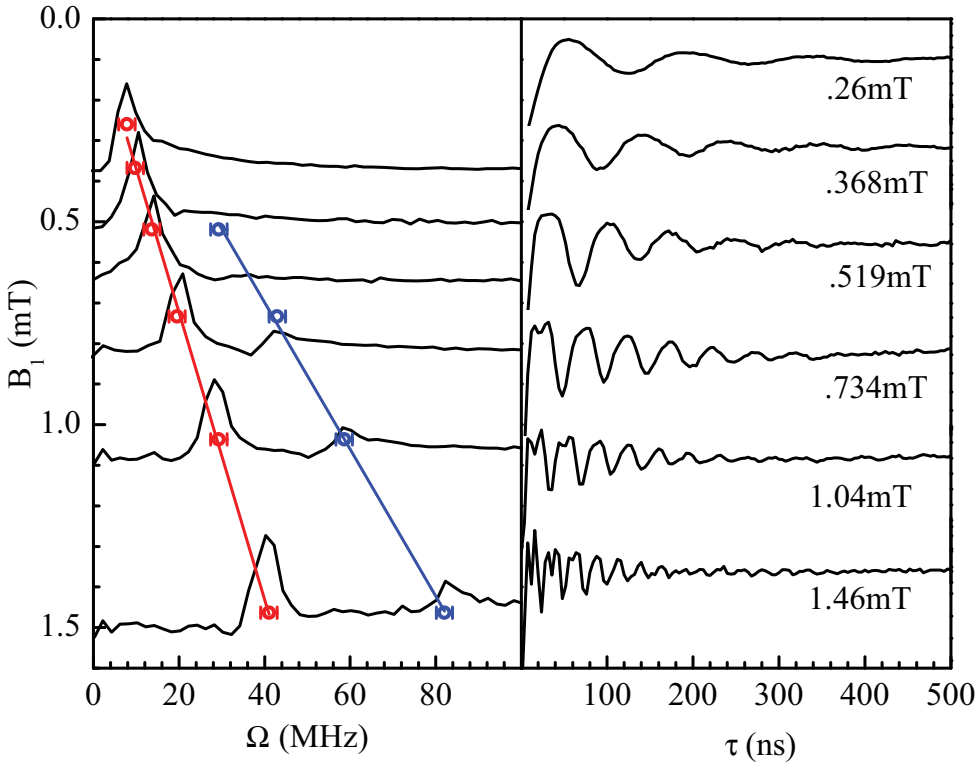

Figure 2.5. Right: The integrated current after a coherent microwave pulse, measured as a function of the pulse length. Left: Fourier transform of the nutation transients normalized to the nutation frequency of an isolated spin-1/2. The plot shows only a single nutation frequency of spin-1/2 at low B_1 strengths and a second frequency spin-1 component becomes stronger as B_1 increases. This behavior is indicative of a weakly coupled pair mechanism.

as a beat component or noise, it is clear that there is no beat component that would be stronger than the spin-1/2 nutation component as anticipated for the presence of exchange interaction. As the B_1 field is increased a second frequency component corresponding to $\Omega = \gamma B_1$ becomes more prominent corresponding to the case where $B_1 \gg \Delta\omega$.

2.3 Rabi-nutation mapping and simulation: confirmation of weakly coupled pair

Information from the last section gives clear and unambiguous evidence that the weakly coupled pair is responsible for the pEDMR signals seen in this material, but to further confirm the nature of the interaction an integrated Rabi nutation experiment as a function of the external magnetic field was carried out. This was done in order to gain a detailed 2D Rabi frequency measurement (a measurement of a Rabi transient as a function of the applied magnetic field B_0) much like what is modeled in Ref [2,3]. A collection of simulations were then carried out, including models that represented either the weakly coupled pair or a exchanged coupled pairs. These results are shown in Fig. 2.6 a)-d), with Fig. 2.6 a)-b) are the integrated Rabi nutation data and the corresponding FFT mapping.

The numerical model used to generate the simulated data in Fig. 2.6 c)-d) involved the weakly and strongly exchanged coupled spin-pair approximation as described by Boehme and Lips [1], Rajevac et al. [3] and Gliesche et al. [2]. For weakly coupled pairs, the precession related to the spin-spin interaction is less relevant than the field-induced precession, i.e. $(D^d{+}\mathrm{J}) \ll (\hbar\gamma B_1, \Delta\omega)$, with D^d the zero-field splitting parameter, J the mutual exchange coupling, and $\Delta\omega$ the difference of the Larmor frequencies within a pair. Under such a consideration, a purely analytical solution for the pulse length dependent change in density can be found. In addition, a double integration over the two distributions has been taken into account due to the hyperfine-induced inhomogeneity in Landé g-factor. The widths of the resonances for electron and hole in the simulation were taken from the two Gaussians describing the resonance spectrum in Fig. 2.4a). No dephasing effects were added in this simulation. For the simulation of strong exchange coupling ($\Delta\omega \ll J$), a Liouville equation

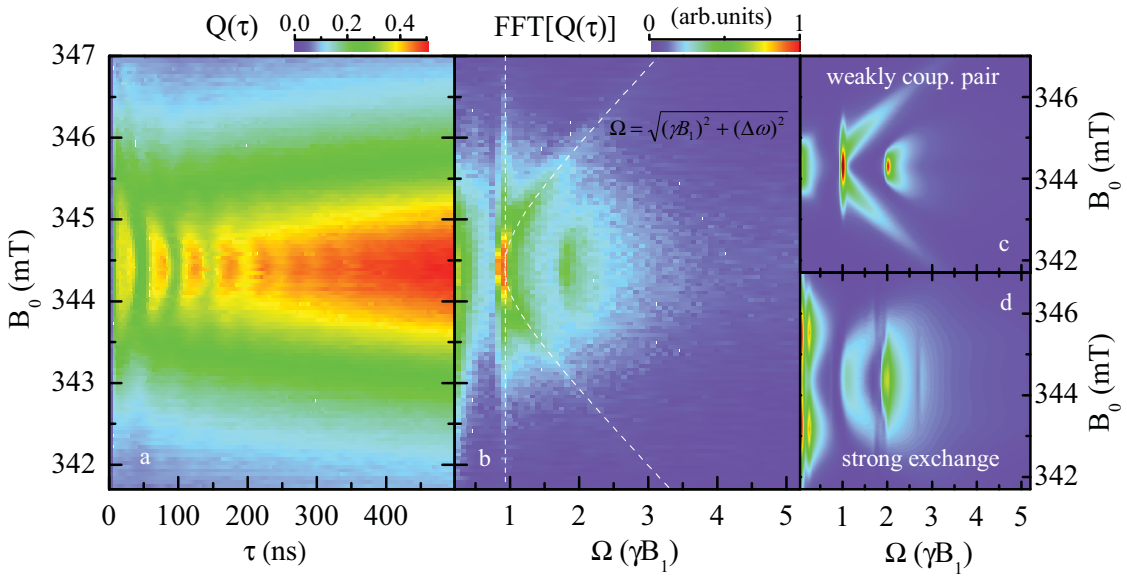

Figure 2.6. Rabi frequency detuning of coherent spin dynamics of weakly-coupled carrier pairs in an OLED at room temperature. a) Varying the external magnetic field B_0 off resonance (driving field B_1=1.1 mT) leads to an increase in the Rabi flopping frequency as a function of microwave pulse duration τ due to detuned driving of the spin two-level system. (b) A Fourier transform of the Rabi oscillations in (a) reveals a dominant spin-1/2 frequency component at γB_1 (dashed white line) and a spin beating feature at $2\gamma B_1$ which arises as a result of simultaneous rotation of both spin pair partners, electrons and holes. The coherent oscillations at large detuning are well described by Rabi's relation, inset. (c) The experiment agrees with numerical modeling of a weakly-coupled spin pair process following Ref. [3], assuming no decoherence. (d) For comparison, a simulation of a strongly exchange-coupled pair is shown.

for the ensemble of pairs consisting of two charge carriers with spin s = 1/2 was solved numerically under consideration of Gaussian distributed hyperfine fields yet in absence of any coherent or incoherent dephasing effects. Parameters for hyperfine- and exchange-coupling strengths for the two simulations were obtained from fits of the resonance lines of the magnetic field dependency data of the sample current (shown in Fig. 2.4 a) for the two given coupling scenarios. There is excellent agreement of the experimental data with the simulation of the weakly coupled pair model. The features reproduced in the simulation are the low frequency components, the strong spin-1/2 signal at $\Omega = \gamma B_1$, the reproduction of the Rabi-formula hyperbolic feature and the slightly smaller in magnitude signal at $\Omega = 2\gamma B_1$ corresponding to the spin-1 or the simultaneous rotation of both pairs. What is not seen in the data that is seen in the strong exchange coupled pair are the very strong low-frequency components spread by $\Delta\omega$, and the much weaker signal at γB_1. Based on this comparison, it is concluded that isotropic (Heisenberg) exchange interaction does not have any observable significance in the observed PPs. Since $\Delta\omega \approx 0.8$mT, one can conclude that exchange within the PPs must be at least an order of magnitude smaller ($J <$ 10neV).

2.4 Discussion

The magnetic field dependence of the current transients in Fig. 2.4 unambiguously confirms that the spin-dependent processes in MEH-PPV OLEDS are due to a pair mechanism as the enhancement/quenching behavior is observed. Given the Landé-factor of $g \approx 2.003(1)$, it is clear that these pairs consist of polarons. The transient nutation data obtained with pEDMR experiments reveals solely a spin-1/2 nutation frequency at low driving fields and no dominant higher order beat oscillations until $B_1 \gg \Delta\omega$. Note that had the spectrum shown in Fig. 2.4 been determined by the presence of exchange coupling we would have anticipated the presence of a nutation beat signal at B_1 fields smaller than the exchange strength which is equal to the separation of the center peak and the two satellite peaks (1.3mT). Due to the absence of this beat oscillation in the nutation data of Fig. 2.5 at low B_1, we conclude that

the spectrum shown in Fig. 2.4 is not caused by exchange interaction. At high B_1, the FFT of the Rabi nutation data does show a beat signal (due to a broad excitation with) which is matched very well with simulations based on PPs that are very weakly spin coupled. It is therefore conclude exchange coupling within the precursor pairs is not J=1.3mT (as suggested by the spectral fit) and it can not be determined from this spectral data. However, using the B_0-field dependence of the Rabi nutation, an upper limit for the exchange can be set ($J < 10$neV).

2.5 References

[1] C. Boehme and K. Lips, Phys. Rev. B **68**, 245105 (2003).

[2] A. Gliesche et al., Phys. Rev. B **77**, 245206 (2008).

[3] V. Rajevac et al., Phys. Rev. B **74**, 245206 (2006).

[4] D. R. McCamey, S.-Y. Lee, S.-Y. Paik, J. M. Lupton, and C. Boehme, Phys. Rev. B **82**, 125206 (2010).

[5] C. Michel et al., Phys. Rev. B **79**, 052201 (2009).

[6] C. Boehme and K. Lips, 2006.

[7] T. W. Herring et al., Phys. Rev. B **79**, 195205 (2009).

[8] D. R. McCamey et al., Nat Mater **7**, 723 (2008).

[9] S. Schaefer et al., phys. stat. sol. (b) **245**, 2120 (2008).

[10] W. Harneit et al., Phys. Rev. Lett. **98**, 216601 (2007).

[11] F. Castro et al., Journal of Non-Crystalline Solids **338340**, 622 (2004).

CHAPTER 3

HYPERFINE-FIELD-MEDIATED SPIN BEATING IN ELECTROSTATICALLY BOUND CHARGE CARRIER PAIRS

In the previous chapter it was shown that pEDMR signals of MEH-PPV based OLEDs are due to recombination of weakly spin–coupled PPs. This conclusion was supported not only by the observed spectral linewidth, but also be the B_1 dependent spin–beat signature obtained from the Rabi nutation effect. In this chapter, it is shown how electrically detected Rabi nutation can be used to obtain information about the local hyperfine fields in Coulombically bound polaron pairs. Organic semiconductors offer a unique environment to probe the hyperfine coupling of electronic spins to a nuclear spin bath. The interaction of spins in PPs in the presence of inhomogeneous hyperfine fields by monitoring the modulation of the current through an organic light emitting diode under coherent spin-resonant excitation are explored. At weak driving fields, only one of the two spins in the pair precesses. As the driving field exceeds the difference in local hyperfine field experienced by electron and hole, both spins precess, leading to pronounced spin beating in the transient Rabi flopping of the current. This effect is used to measure the magnitude and spatial variation in hyperfine field on the scale of single carrier pairs, as required for evaluating models of organic magnetoresistance, improving organic spintronics devices, and illuminating spin decoherence mechanisms.

The chapter is a reprinted of a paper[1] published in *Physical Review Letters* in

[1]McCamey, D. R. and van Schooten, K. J. and Baker, W. J. and Lee,S.-Y. and Paik, S.-Y. and Lupton, J. M. and Boehme, C.,Hyperfine-Field-Mediated Spin Beating in Electrostatically Bound Charge Carrier Pairs,Phys. Rev. Lett. 104, 017601 (2010),

the year 2010 with coauthors Dane McCamey, Kipp van Shooten, Sang-Yun Lee, Seo-young Paik, John Lupton, and Christoph Boehme.

3.1 Hyperfine fields in organic semiconductors

The hyperfine interaction between single electronic and nuclear spins is well understood theoretically [1]. In real condensed matter spin-based systems, however, individual electronic spins couple to an ensemble, or bath, of nuclear spins [2–4]. Such coupling is of both technological and fundamental importance. Local variations in the hyperfine field contribute significantly to spin dephasing in many types of quantum bits, including GaAs quantum dots [2, 5, 6] and NV centers in diamond [6]. As well as influencing the fundamental recombination processes responsible for light emission in organic light-emitting diodes (OLEDs), such local variations are also a leading candidate for explaining the large magnetoresistive effects observed in organic semiconductors [7–12]. For example, the bipolaron model of organic magnetoresistance proposes that spin mixing by local variations of the hyperfine field reduces spin blockade of hopping transport at low magnetic fields. The interaction of quantum systems with their environment has also been discussed in the context of the emergence of classical behavior [13]. Exploiting spin-dependent carrier recombination in organic semiconductors [14], the fundamental spin interaction within pairs of electrostatically bound charge carriers is probed, as mediated by the local nuclear spin bath. Time-domain beating in the spin precession in electrostatically correlated spin pairs in an OLED is demonstrated, driven by a resonant electromagnetic field. Such beating occurs when the driving field compensates the local difference in hyperfine fields acting on each spin within a pair, and appears as a doubling of the frequency with which the spin pair transitions between singlet and triplet configuration [15, 16]. Organic semiconductors provide a unique platform to explore the underlying physics of spin coupling due to long spin lifetimes, weak spinorbit coupling, and facile electric readout [14]. While usually considered as a way to obtain promising new device architectures [17, 18], organic spin electronics provide a rich parameter space in which to study fundamental spin physics [19]. Recently, it was demonstrated that

conventional disordered organic semiconductors, such as the conjugated polymer poly[2-methoxy-5-(2'-ethylhexyloxy)- 1,4-phenylene vinylene] (MEH-PPV), display surprisingly long spin coherence times on the order of 1μs, which can readily be exploited using pulsed electrically detected magnetic resonance (PEDMR) techniques [14]. As with other carbon-based systems such as fullerenes [20], carbon nanotubes [3, 21], graphene [22], and diamond [4], organic semiconductors can exhibit extremely weak spin-orbit coupling; however, the ubiquitous hydrogen atoms in organic semiconductors give rise to significant hyperfine interactions, which, combined with the structural disorder, result in substantial inhomogeneous broadening of resonance field strengths [23]. Organic semiconductors are inherently large-gap ambipolar materials and can support both electron and hole currents in the undoped state [24], which, combined with the weak dielectric screening and strong carrier pair correlation, allows us to probe intrinsic spin interactions in electrostatically coupled electron-hole pairs. In contrast to mesoscopic systems, which are conventionally used to study elementary spin physical processes [2,5,25], organic semiconductors combine facile processing with a wide range of physical interactions. Rather than selecting particular spin coupling scenarios by addressing individual units, as is the approach commonly pursued in quantum dot spin spectroscopy [2, 5], disordered strongly interacting conjugated polymers allow us to use pEDMR to select particular interaction pathways. Thus is is possible to investigate the transition of electrostatically bound charge carrier pairs from acting as isolated charges (with a spin-1/2 resonance) to displaying correlated behavior.

3.2 Experiment

3.2.1 Weakly coupled pair

Under standard operating conditions of an OLED, electrons and holes are injected from opposite electrodes, migrate through the device, and ultimately recombine, forming either a light-emitting exciton of singlet character or a non-light-emitting triplet exciton (referred to here as injection-recombination). As the injected charge carriers move through the disordered organic semiconductor film, two characteristic distances

can be defined: r_C, the carrier separation below which the Coulombic binding energy of electron and hole exceeds the thermal energy of the carriers, and r_K, the carrier separation below which the electrostatically bound carrier spins begin to interact. Below r_K a linear superposition of the spin states has to be considered, leading to an energetic splitting between singlet and triplet manifolds [26]. Generally, experiments on OLEDs probe either injection-recombination or the reverse process: dissociation of an optically generated exciton to yield a photocurrent. Very little is known about the interchromophoric exchange interaction, when electron and hole reside on different conjugated segments (on different chains or within a chain) within the film. In contrast, when electron and hole finally recombine on one conjugated segment, the resulting singlet or triplet excitons are strongly exchange split by typically 0.7 eV [10]. Coherent spin effects allow us to investigate this important transition region at the onset of intermolecular exchange. As singlet excitons are typically preferable for efficient OLEDs, it is especially crucial to understand the nature of this exchange to appreciate fundamental efficiency limitations in devices [27].

PEDMR on MEH-PPV OLEDs similar to devices previously described [14] were performed. In those earlier experiments, noise-limited current resolution prohibited observation of the intricacies of the resonance line shape [28], which was assumed to originate from single carriers, either electrons or holes. Figure 3.1 shows the change in current passing through an operating OLED biased in the forward direction as a function of magnetic field (B_0), following a short microwave pulse.

Careful inspection of the signal reveals that it cannot be fit by a single Gaussian line, as would be expected for a resonance from a single spin species. The data are well fit by both two and three Gaussian resonances. As discussed in Chapters 1 and 2, these data can be discussed only as an ensemble of strongly Coulomb–coupled, but weakly spin-coupled spin pairs (two–spin s =1/2 systems). Individual spins and spin-dependent process involving more than two spins can be excluded due to the real time behavior and the line shapes of this signal. Thus, the observed signal is due to a system with two spin species that are, in principle, exposed to different numbers of surrounding nuclear spins (hyperfine fields). This confirms studies which

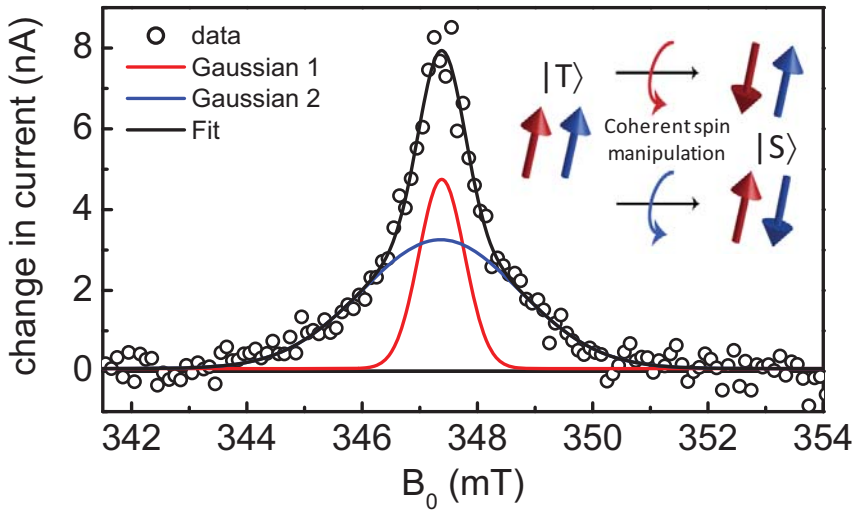

Figure 3.1. Observation of the two spin partners in an electrostatically bound carrier pair in an OLED. The pair can be shuttled between the singlet and triplet manifold by coherently manipulating the orientation of one of the two electron spins within the pair (inset). The change in current through a MEH-PPV OLED 10.2 μs after a microwave pulse is plotted as a function of external magnetic field B_0. The spectrum is described by two Gaussian lines, that is assigned to the two spins in the carrier pair.

demonstrated that the resonance shape in fact arises from the difference in local hyperfine field felt by each spin [28, 29], indicating that this is the dominant cause of the observed spectra. The ability to fit the spectrum with two Gaussian lines indicates that the signal arises from the two different spin species which form the electrostatically coupled carrier pair: electron and hole.

3.2.2 Using spin beating to determine average hyperfine strength

When spin resonance causes coherent precession of either the electron or the hole spin in the driving microwave (B_1) field as illustrated in the inset of Fig. 3.1, the permutation symmetry of the spin pairs will start to oscillate at the same frequency [15], resulting in a change of the total recombination and dissociation rates of the system. Indeed, it is this change of rates which allows electrical detection of the resonance, since it causes an increase in the free polaron density directly following the spin manipulation (see supplementary information in Ref. [14] for details of this mechanism). The peak of the resonance line provides the g factor of the spin species, $g = 2.003$. This value is in agreement with previous conventional, optically detected, and electrically detected electron paramagnetic resonance (ESR) studies of radicals and radical pairs [28, 30]. Since the width of the resonance Γ is not determined by spin-orbit coupling or dipolar electron spin interactions, it offers a measure of the distribution of the hyperfine field strength present at different sites in the disordered molecular film [23]. While one cannot assign positive and negative charges to the two lines observed it is not surprising that Γ should differ for electrons and holes since this will depend very sensitively on the localization of the carrier wave function; the degree of localization determines the number of hydrogenic nuclear spins the carrier spin interacts with, which in turn need not be equal for the two charge species. The larger the number of nuclear spins that interact with the polaron, the smaller the total hyperfine field they will feel. This rather counterintuitive effect arises because the standard deviation (from zero) of the net nuclear spin orientation decreases as the ensemble size increases (due to the central limit theorem), leading us to conclude that the narrower line arises from the larger polaron. Fitting two Gaussians, $G(B, \Gamma)$, to

the resonance spectrum allows us to extract the hyperfine fields felt by each polaron type, $\Gamma_a = 2.7(2)$mT and $\Gamma_b = 0.79(5)$mT, analogous to earlier incoherent EDMR investigations [28]. One can also estimate the difference in hyperfine field between electron and hole within a carrier pair by computing the expectation value of the difference in a random distribution of hyperfine fields, i.e.,

$$\langle |\Delta B_H yp| \rangle = \int \int_{-\infty}^{+\infty} = G_a(B_a\Gamma_a)G_b(B_b\Gamma_b)\,|B_a - B_b|\,dB_b dB_a = 1.1(1)mT \quad (3.1)$$

It is noted that the experimental value of $\langle |\Delta B_{Hyp}| \rangle$ obtained in this way is in agreement with earlier theoretical estimates based on the inhomogeneous line shape [11]. Here an experiment is presented that allows the confirmation of this estimate by directly probing the difference in hyperfine field of spins within charge carrier pairs coherently manipulated with different B_1 driving fields. Figure 3.2 a) displays coherent modulation of the OLED current as a function of the duration of a spin-resonant microwave pulse of magnitude $B_1 = 1.2$mT. As the length of the pulse

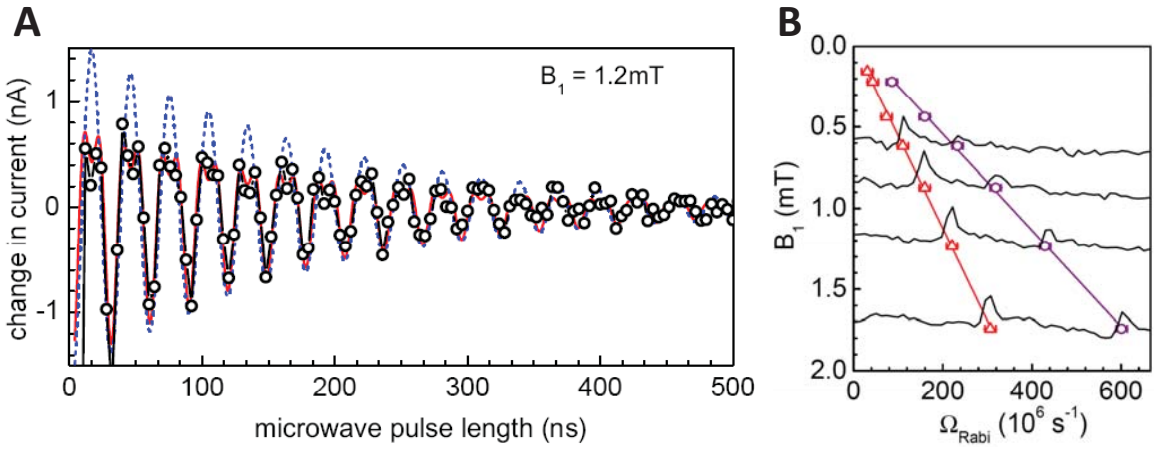

Figure 3.2. (a) Coherent oscillations of the ensemble of spin pairs, observed by measuring the change in OLED current 7.2 μs after application of resonant microwave pulses of increasing length. The fit with an exponentially damped sinusoidal function with components at both Ω_{Rabi} and $2\Omega_{Rabi}$ is shown (solid red line), as is a fit with only a single frequency component Ω_{Rabi} (dashed blue line). (b) Sample Fourier transform spectra of Rabi nutation traces obtained at different B_1 field strengths. The frequency of the two peaks was determined, and plotted as a function of B_1

increases, the spin state of the charge carrier pair undergoes Rabi oscillations from singlet to triplet and back again, as sketched in the inset of Fig. 3.1. This oscillation leads to a periodic modulation of the current depending on the duration of the applied B_1 field. The oscillations, seen in Fig. 3.2 a), which extend for over 17 periods, can be accurately described by a superposition of two oscillating functions of frequency Ω and 2Ω. For comparison, a periodic function with a single period is fitted (dotted line). The high quality of the data and the long coherence time of the spin precession allow us to perform an accurate analysis of the Fourier components in the oscillations. Figure 3.2 b) shows the frequency spectrum for four different driving fields, B_1, close to the estimated field $\langle|\Delta B_{Hyp}|\rangle$. Two peaks are clearly identified in the Fourier spectrum, at $\Omega = \Omega_{Rabi}$. The Fourier frequency components are also plotted as a function of driving field B_1. As expected from Rabi's frequency equation for a spin in resonance with an electromagnetic field, the Rabi frequency varies linearly with B_1 field for both peaks [with a factor of 2 difference between slopes, lines in Figure 3.2 b)]. The ratio of peak areas also changes as the B_1 field is changed, with the beat signal disappearing at low driving fields. Figure 3.3 a) illustrates the Rabi nutation experiment. As long as $B_1 < |\Delta B_{Hyp}|$, either electron or hole spin within the pair should precess in response to the on-resonant driving field, but not both, as the other pair partner is likely out of resonance. Once $B_1 > |\Delta B_{Hyp}|$, the driving field is so strong that the intrinsic hyperfine field-induced variation between electron and hole resonance (g factor) is overcome, and both carriers within a pair precess together rather than individually [15, 16]. This joint precession halves the time period required for triplet-singlet transitions, thereby doubling the frequency of modulation of the measured device current. Frequency doubling arises since the pair's spin permutation symmetries reflect the beat oscillation of the two pair partners' spin-1=2 Rabi frequencies (i.e., $\Omega = 2\Omega_{Rabi}$) [15,16]. This dependence is summarized in Fig. 3.3 b), where the relative fraction of spin pairs with the fundamental (Ω_{Rabi}) and twice the fundamental frequency ($2\Omega_{Rabi}$) is plotted as a function of B_1. The B_1 dependence of the relative intensities of fundamental and harmonic frequencies can be accurately described by a quantile function, as expected given a Gaussian distribution,

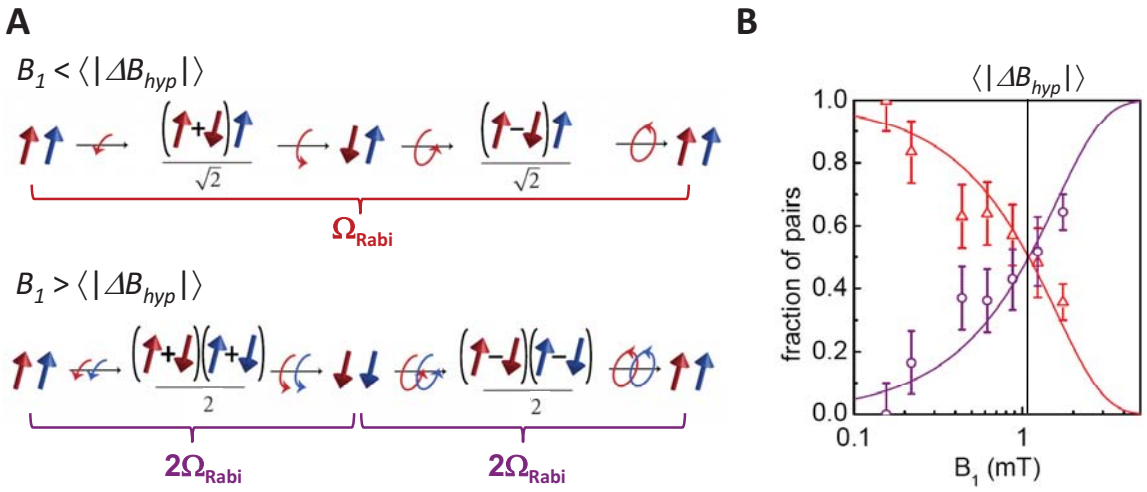

Figure 3.3. Beating of spin precession following compensation of the difference in intrapair hyperfine fields. (a) As the driving field is increased, the current modulation frequency changes from the Rabi frequency Ω_{Rabi} to twice the Rabi frequency. This doubling arises because the difference in intrapair hyperfine fields is overcome and both spins are simultaneously in resonance. (b) Relative fraction of pairs with $\Omega = \Omega_{Rabi}$ (not beating) ($\triangle$) and $\Omega = 2\Omega_{Rabi}$ (beating) ($\bigcirc$). The solid lines show the expected form of the distribution, the crossover of which gives a measure of $\langle|\Delta B_{Hyp}|\rangle$ = 1.1(1) mT

$G(\Gamma)$, $|\Delta B_{Hyp}|$ i.e., $f(B_1) = 2\int_0^{B_1} G(\Gamma)dB$ whereΓ is determined by$\langle|\Delta B_{Hyp}|\rangle$. The two fit curves cross at $B_1 = 1.1$mT, precisely when the driving field overcomes the difference in hyperfine fields experienced by the electron and hole within a pair. By overcoming the local hyperfine field disorder at $B_1 = \langle|\Delta B_{Hyp}|\rangle$, a threshold driving field is reached at which the pair partners' resonances mix and spin beating occurs. This direct measurement of $\langle|\Delta B_{Hyp}|\rangle$ by the observation of B_1-induced spin beating coincides with our estimate based on the resonance line shapes shown in Fig. 3.1.

3.3 Conclusion

It is noted that the experiments presented here did not reveal signatures of spin-dipolar interactions within the pair, which would be manifested in either the magnetic field dependence of the resonance or in the Rabi nutation as a component with frequency $\Omega = \sqrt{2}\Omega_{Rabi}$[37]. Spin-exchange coupling can also be excluded, since such coupling results in $f(2\Omega_{Rabi}) = 1$ independent of the magnitude of B_1 [31]. The absence of dipolar spin-spin interactions leads us to conclude that the carriers in a pair are separated by a distance of more than 2nm, and are therefore most likely intermolecular. Besides offering a unique approach to tuning coherent spin-spin interactions, this direct experimental determination of $\langle|\Delta B_{Hyp}|\rangle$ in the time domain is crucial to interpreting magnetic field effects in disordered organic semiconductors, noting prior controversy surrounding the precise value of $\langle|\Delta B_{Hyp}|\rangle$ [11]. This technique may also be of use for measuring differences in local magnetic environments in other materials where the g-factor separation is due to mechanisms other than the hyperfine field. Examples of nonhyperfine field mechanisms that could lead to different resonances of electron and hole include spin-orbit coupling [32], spin-dipolar coupling, and spin exchange coupling [33] within the pair. It is noted that determining $\langle|\Delta B_{Hyp}|\rangle$ by fitting the spectral line shapes assumed that there was no correlation between the hyperfine fields felt by polarons within each pair. The confirmation of this assumption by the time domain beating indicates that there is no substantial overlap of the polaron wave functions, as such an overlap would lead to a correlation of the hyperfine fields from the nuclear spins within the shared region. This is consistent

with the pairs having weak exchange, as confirmed by the B_1-field dependence of the Rabi frequency. Spin-spin interactions in mesoscopic systems are usually investigated using coupled quantum dots, which are experimentally demanding [2, 3, 5, 26]. Spin beating occurs naturally in organic semiconductors during bipolar carrier capture, the prerequisite process in any OLED. The combination of these versatile material systems with the unique abilities of the PEDMR technique promises many future insights into the fundamentals of spin interactions in small spin ensembles and may ultimately offer a hitherto unexplored pathway to creating entangled states for quantum information processing.

3.4 References

[1] N.M.Atherton, *Electron Spin Resonance*, Ellis Horwood,Pretence Hall, chichester, England, 1993.

[2] D. J. Reilly et al., Science **321**, 817 (2008).

[3] H. O. H. Churchill et al., Nat Phys **5**, 321 (2009).

[4] G. Balasubramanian et al., Nat Mater **8**, 383 (2009).

[5] J. R. Petta et al., Science **309**, 2180 (2005).

[6] S. Takahashi, R. Hanson, J. van Tol, M. S. Sherwin, and D. D. Awschalom, Phys. Rev. Lett. **101**, 047601 (2008).

[7] Y. Sheng et al., Phys. Rev. B **74**, 045213 (2006).

[8] P. A. Bobbert, T. D. Nguyen, F. W. A. van Oost, B. Koopmans, and M. Wohlgenannt, Phys. Rev. Lett. **99**, 216801 (2007).

[9] P. A. Bobbert, W. Wagemans, F. W. A. van Oost, B. Koopmans, and M. Wohlgenannt, Phys. Rev. Lett. **102**, 156604 (2009).

[10] M. Reufer et al., Nat Mater **4**, 340 (2005).

[11] J. M. Lupton and C. Boehme, Nat Mater **7**, 598 (2008).

[12] J. D. Bergeson, V. N. Prigodin, D. M. Lincoln, and A. J. Epstein, Phys. Rev. Lett. **100**, 067201 (2008).

[13] W. H. Zurek, Rev. Mod. Phys. **75**, 715 (2003).

[14] D. R. McCamey et al., Nat Mater **7**, 723 (2008).

[15] C. Boehme and K. Lips, Phys. Rev. B **68**, 245105 (2003).

[16] V. Rajevac et al., Phys. Rev. B **74**, 245206 (2006).

[17] Z. H. Xiong, D. Wu, Z. Valy Vardeny, and J. Shi, Nature **427**, 821 (2004).

[18] V. A. Dediu, L. E. Hueso, I. Bergenti, and C. Taliani, Nat Mater **8**, 707 (2009).

[19] W. M. Witzel and S. Das Sarma, Phys. Rev. B **77**, 165319 (2008).

[20] W. Harneit et al., Phys. Rev. Lett. **98**, 216601 (2007).

[21] K. Tsukagoshi, B. W. Alphenaar, and H. Ago, Nature **401**, 572 (1999).

[22] N. Tombros, C. Jozsa, M. Popinciuc, H. T. Jonkman, and B. J. van Wees, Nature **448**, 571 (2007).

[23] S. Kuroda, T. Noguchi, and T. Ohnishi, Phys. Rev. Lett. **72**, 286 (1994).

[24] C. E. Pope, M. & Swenberg, *Electronic Processes in Organic Crystals and Polymers*, Clarendon, 1982.

[25] F. H. L. Koppens et al., Science **309**, 1346 (2005).

[26] M. Segal, M. A. Baldo, R. J. Holmes, S. R. Forrest, and Z. G. Soos, Phys. Rev. B **68**, 075211 (2003).

[27] M. Wohlgenannt, K. Tandon, S. Mazumdar, S. Ramasesha, and Z. V. Vardeny, Nature **409**, 494 (2001).

[28] G. B. Silva, F. Nesch, L. Zuppiroli, and C. F. O. Graeff, phys. stat. sol. (c) **2**, 3661 (2005).

[29] V. Dyakonov, G. Rösler, M. Schwoerer, and E. L. Frankevich, Phys. Rev. B **56**, 3852 (1997).

[30] M.-K. Lee, M. Segal, Z. G. Soos, J. Shinar, and M. A. Baldo, Phys. Rev. Lett. **94**, 137403 (2005).

[31] C. Boehme et al., phys. stat. sol. (b) **246**, 2750 (2009).

[32] J. Spaeth and H. Overhof, *Point Defects in Semiconductors and Insulators*, Springer, Berlin, 2003.

[33] S. Schaefer et al., phys. stat. sol. (b) **245**, 2120 (2008).

CHAPTER 4

TRIPLET EXCITON-POLARON RECOMBINATION IN MEH-PPV

There have been many proposed models for spin-dependent conductivity mechanisms in organic semiconductor materials other than the PP mechanism discussed above, this includes; triplet-triplet annihilation [1], bipolaron pair transport [2], triplet-excition polaron [3,4]. Some of the these interactions have recently received attention due to the still unresolved OMAR effect. Some these models differ on a microscopic scale fundamentally, yet macroscopically they agree with the experimental OMAR data. Thus, without an experimental confirmation of the true nature of the spin-dependent processes on a microscopic level, the accuracy of these models has remained elusive.

This chapter is reprinted from a paper[1] published in 2011 in *Physical Review B* on page 165205. The manuscript was coauthored by Dane McCamey, Kipp Van Shooten, John Lupton and Christoph Boehme, and represents a collection of studies in which devices were made with the sole intent to find signs of any of the other interactions outside the commonly seen polaron pair. The first of which describes the interaction of free electron polarons with bound triplet excitons before recombination. To the best of the authors knowledge, this is the first study that strongly confirms the existence of the mechanism, and shows the power of the pEDMR method.

Pulsed electrically-detected magnetic resonance offers a unique avenue to distinguish between polaron-pair (PP) and triplet-exciton polaron (TEP) spin-dependent

[1]Baker, W. J., McCamey, D. R., van Schooten, K. J., Lupton, J. M. and Boehme, C.,Phys. Rev. B 84,165205 (2011).

interactions, which control the conductivity and magnetoresistivity of organic semiconductors. Which of these two fundamental processes dominates depends on carrier balance: by injecting surplus electrons, it is shown that both processes simultaneously impact the device conductivity. The two mechanisms are distinguished by the presence of a half-field resonance, indicative of TEP interactions, and transient spin beating, the signature of PPs. Coherent spin Rabi flopping in the half-field (triplet) channel is observed, demonstrating that the triplet exciton has an ensemble phase coherence time of at least 60ns, offering insight into the effect of carrier correlations on spin dephasing.

4.1 Models for spin-dependent processes in organic semiconductors

Spin-dependent phenomena, though amongst the first physical effects studied in organic semiconductors [1], have only recently been explored in the context of device applications [5]. Spin-dependent conductivity has received particular attention in magnetoresistive devices [2, 5–9] which offer avenues to information storage and magnetic field sensing. However, without direct observation of spin precession through, e.g., the Hanle effect, it is hard to separate magnetic field phenomena in spin valves [5] into bulk spin polarization and surface magnetization effects [10]. Devices with non-magnetic electrodes also show magnetoresistance effects [2, 6–9], which are virtually impossible to break down into bulk and interfacial processes. Although models of organic magnetoresistance have started appearing, largely based on site-specific Pauli-blocking mechanisms [2], the qualitative similarity in magnetoresistance in a wide range of very different semiconducting materials [5, 11], both organic and inorganic, urges caution in assigning a particular material-specific mechanism to the phenomenon. Many of these models derive from a phenomenological description of the influence of magnetic fields on molecular reaction kinetics [12]. As these approaches rely on indirect inference of the role of spin in conductivity, it is not always apparent how they may apply to a particular measurement situation [8]. Electron paramagnetic resonance, in contrast, allows carrier spin to be directly manipulated, and is thus ideally suited to unraveling spin-dependent transport in organic devices.

A longstanding question in the physics of spin-dependent processes in organic semiconductors has been the interpretation of optically- or electrically-detected magnetic resonance (O/EDMR) in terms of the polaron-pair (PP) mechanism or the exciton-polaron interaction. Vardeny et al. have promoted the former, offering evidence for magnetic resonance signals arising from spin-dependent recombination and dissociation of weakly-coupled spin-1/2 carrier pairs [13, 14]. In contrast, Shinar et al. have reported clear signatures of half-field resonances in EDMR, which can only be observed if spin-1 species such as triplet excitons can influence conductivity, by, for example, modifying recombination and dissociation rates [15]. The discussion has been particularly active [16] because the assignment of the spin-dependent mechanism relates to the ultimate efficiency achievable in organic light-emitting diodes (OLEDs) [9]. It has recently been explored how coherently-driven spin dynamics impact spin-dependent transport using pulsed EDMR, the results of which have been broadly in agreement with the PP model [17–19]. In the following, however, it is shown under which conditions both PP and triplet-exciton polaron (TEP) mechanisms [3, 20] can occur at once, providing an answer to the question of which mechanism is responsible for EDMR signals, [16] and highlighting the power of spin resonance techniques in illuminating magnetic-field effects in organic semiconductors

4.2 Experiment

4.2.1 Devices: balanced and imbalanced injection

A commonly used conjugated polymer poly[2-methoxy-5-(2'-ethyl-hexyloxy)-1,4-phenylene-vinylene] (MEH-PPV) was studied, incorporated into OLED structures designed to operate within an EDMR spectrometer as described previously [18]. The electron-hole carrier was balanced within the device by either fabricating the OLED directly on an indium tin oxide (ITO) anode, or inserting a hole injection layer of poly(3,4-ethylenedioxythiophene) (PEDOT) [21–23]. In the former case, with a calcium cathode, the device is hole-limited [24], whereas PEDOT leads to more balanced carrier injection (Fig. 4.1 a)-b)).

In order to experimentally verify the different injection schemes for the devices

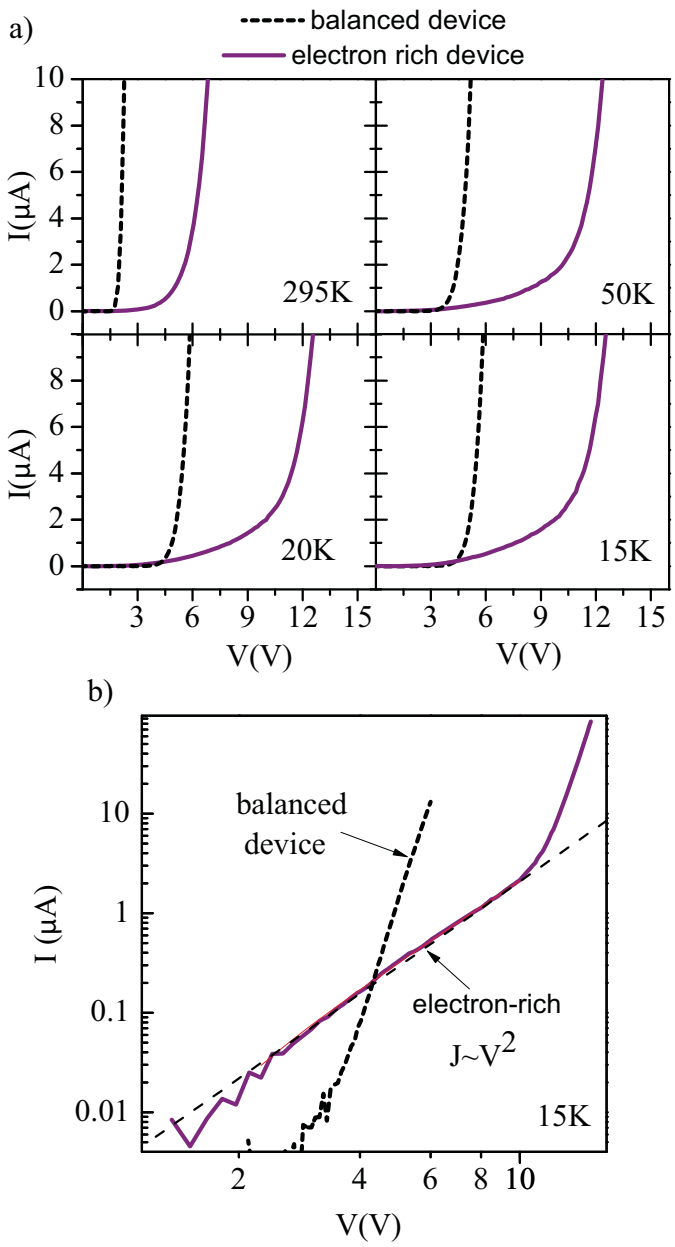

Figure 4.1. (a) IV curves of both balanced (dashed) and electron-rich devices (solid) showing a consistently higher current injection in the balanced devices over the imbalanced resulting from the higher hole injection as a result of the PEDOT:PSS. (b) The 15K IV curve in log-log scale to display the "Child's Law" V^2 dependent current from single carrier dominated injection of the devices without PEDOT:PSS hole-transport layer.

with and without the PEDOT hole injection layer, a series of current-voltage (IV) measurements were undertaken. Fig. 4.1 a) shows IV curves from devices both with the PEDOT ("balanced", dashed) and without the PEDOT ("electron rich", solid) layer. The electron rich devices show consistently higher resistance than the balanced device at all temperatures. This is an indication of less injection into the devices without the PEDOT:PSS, as has been reported repeatedly in many previous OLED efficiency studies. To further scrutinize the charge injection imbalance, IV curves for both electron rich and balanced devices measured at 15K are shown on a double logarithmic scaling (see Fig. 4.1 b)). The dramatic difference in the IV curve functionality between the two devices results from the difference in charge injection imbalance. The balanced device shows an exponential IV characteristic. The current in the electron-rich device shows a V^2 dependency for voltages from 0-11 volts. This is expected in devices with space-charge limited current behavior, where the current is expected to follow the V^2 dependence described by Child's law. The operating points for the PEDMR measurement were always below 9V in the experiment. The fact that these devices show space-charge limited injection demonstrates the single carrier dominated transport. At higher applied voltages, above ∼11V, the current dramatically increases (exponential), indicating the onset of significant hole injection. The functional behavior of the electron-rich IV characteristic at high voltages approximately matches that of the balanced device at lower biases. Fig. 4.2 sketches both configurations and presents X-Band EDMR spectra at full and half field at 295 K and 10 K for each. The "relative change in current" is defined as $\frac{\Delta I}{I_0}$, where ΔI is the change in current on resonance due to spin-dependent processes and I_0 is the total current through the device when a constant bias is applied. All devices show full-field resonances in the differential current at approx. 345 mT, depending on the microwave frequency. At room temperature, no half-field resonance is observable (with a sensitivity of $\frac{\Delta I}{I_0} < 10^{-7}$). Upon cooling to 10 K, a resonance appears at half field (∼172 mT, slightly lower than half of the full-field resonance due to the specific zero-field parameters [25], indicating the involvement of a spin-1 species in transport or recombination. The signal exhibits similar zero-field splitting parameters (D ≈

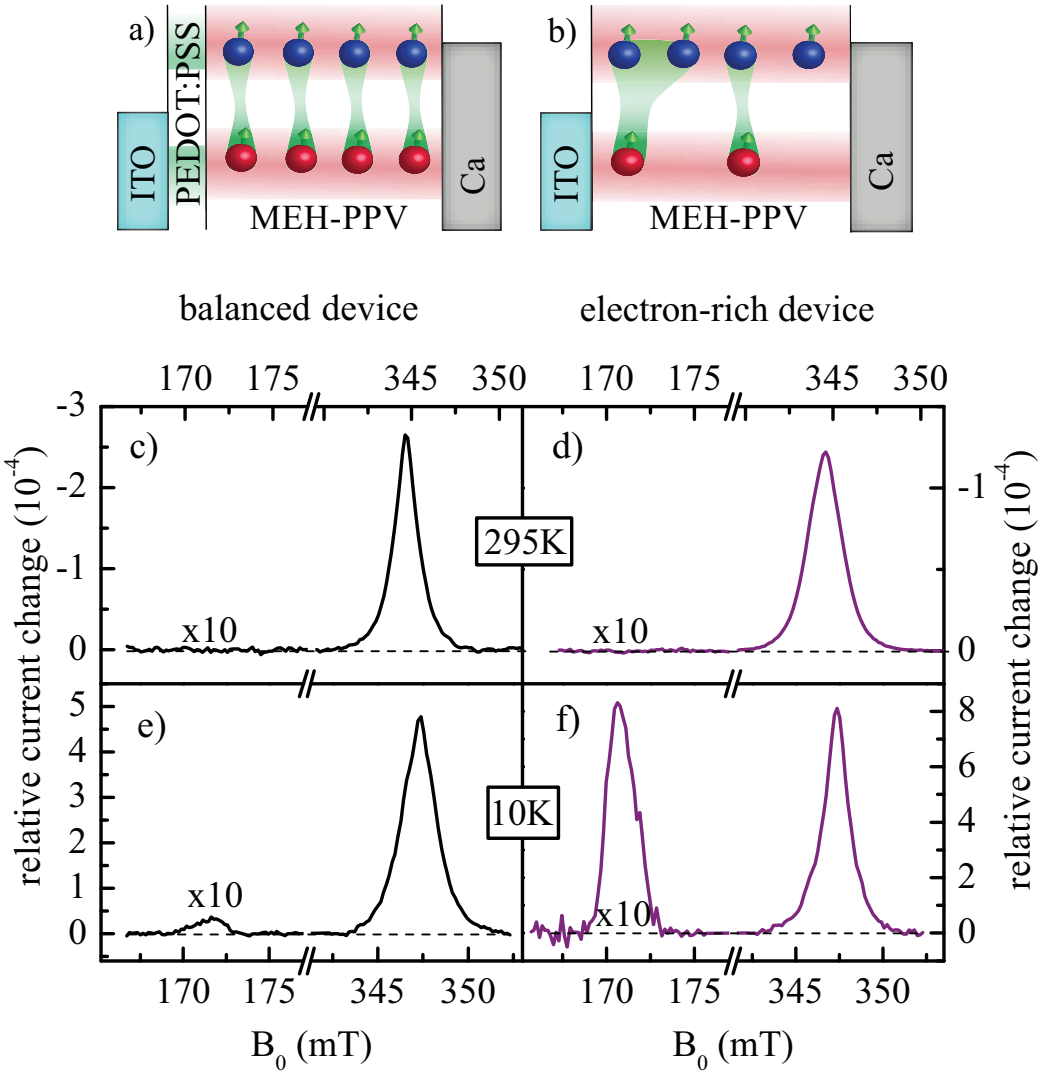

Figure 4.2. X-band EDMR of OLEDs with carrier balance (a) and electron preference (b). (c), (d) At 295 K, only the full-field resonance is observed. (e), (f) At 10 K, the half-field resonance is seen, which depends on carrier balance. Microwave frequencies: 9.66 GHz at 295K and 9.74 GHz at10K.

508 G and $0 \leq E \leq D/3$) to those observed by Shinar [15]. This half-field signal is 10 times stronger for the electron-rich device in Fig. 4.2 f), suggesting that the polaron partner of the triplet exciton in the TEP process is the electron. Spin-1/2 species can be clearly identified by their precession frequency in the EDMR transients discussed below.

4.2.2 Multiple spin–dependent channels

The main focus of this chapter is the identification and experimental discrimination of multiple spin-dependent channels in the electron-rich MEH-PPV OLED devices. Figure 4.3 a)- b) shows evidence that more than one spin dependent channel exists due to the spectral line shape variation as a function of time after the spin-resonant microwave pulse. Regardless of injection imbalance, the resonances seen include both electrons and holes that have been inhomogeneously broadened by the hyperfine interactions with their random nuclear spin environments, giving a different Gaussian line width for each carrier type [18]. If the majority of carriers are involved in the same spin-dependent process, such as in the polaron-pair signal seen in Fig. 4.3 a), the temporal dependence of the resonances involved in the spin dependent process will be identical, and the compound line-shape will not change with time. Consequently, the signal is seen in Fig. 4.3 a) is a reflection of the overall pair dynamics and not just the singular dynamic information of any one of the pair partners [17]. For instance, if the longitudinal relaxation time, or T_1, of one of the two pair partners changed, one might see an overall increase in dynamical behavior, but the temporal difference in the distributions would still be constant after the excitation, as it is determined by the dynamics of all the spins involved in the one spin-dependent channel.

The transient response of an OLED current to a microwave pulse has been discussed in Chapter 2: The initial quenching and subsequent enhancement, due to the different recombination and dissociation dynamics of singlet and triplet PPs, is described in detail in Ref. [17]. Fig. 4.3 a) plots the resonance spectrum of the balanced device at different times following a microwave pulse ($B_1 \approx 0.6$ mT) of 200ns duration. For ease of comparison, the normalized absolute values of the

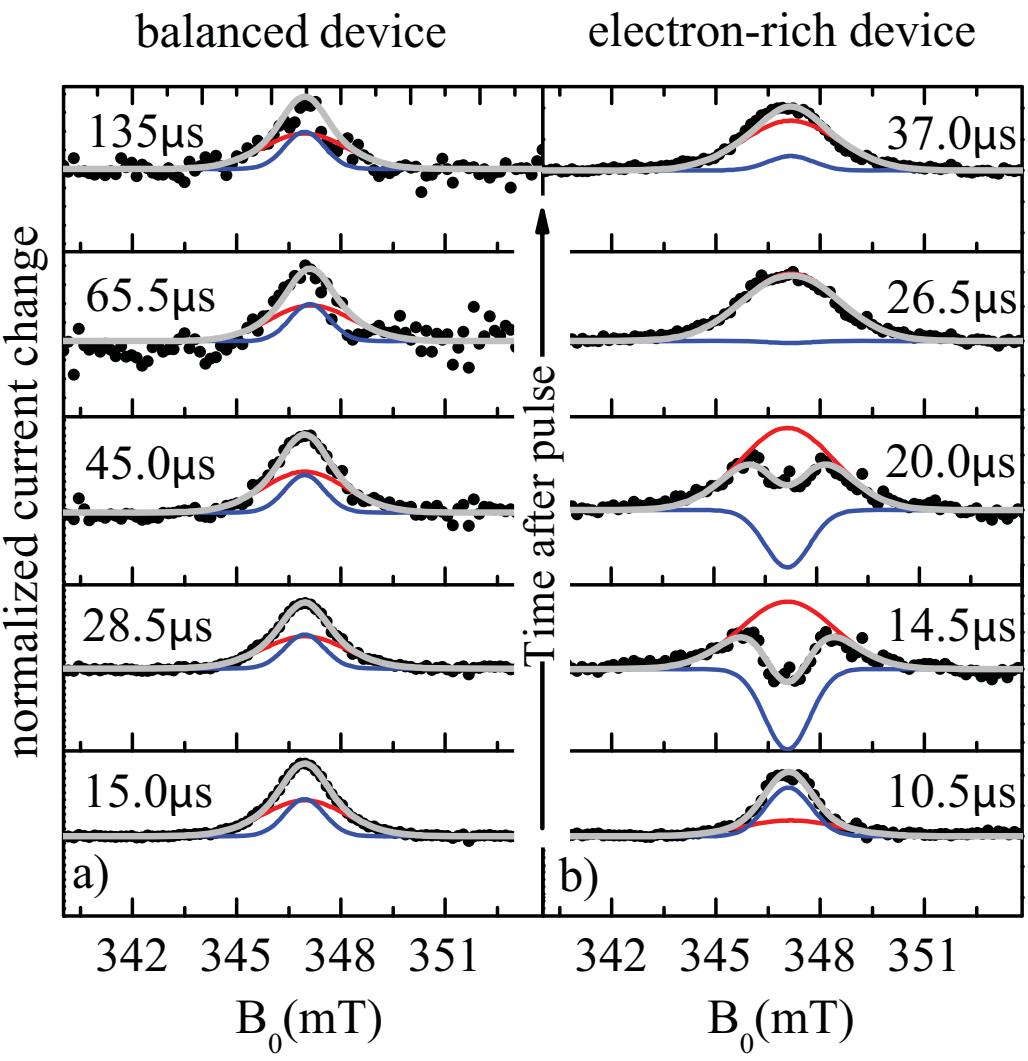

Figure 4.3. Transient EDMR spectra at different times after spin-resonant excitation at 10 K. (a) In the balanced device, the spectrum is time invariant and described by two Gaussians (see text). (b) With excess electrons, the spectrum (described by the same two Gaussians) changes with time, indicating the presence of two spin-dependent mechanisms.

resonance are plotted: the lower four panels correspond to quenching, the upper panel to enhancement. The spectra can all be described by the sum of two Gaussians of different width, corresponding to electron and hole spin-resonances broadened by the hyperfine interaction as described in Ref. [18]. The spectral shape does not change with time, demonstrating that only one spin-dependent mechanism dominates the resonance. For the electron-rich device in Fig. 4.3 b), however, the spectrum changes significantly with time, but is still accurately described by the sum of the same two Gaussians whose relative amplitudes now vary with time. The current transient is more complex, showing the usual quenching-enhancement succession seen in balanced devices, as well as an additional enhancement at short times. For the electron-rich device, two spin-dependent mechanisms with different transient characteristics must be present to account for the temporal dynamics in the spectrum. Importantly, the amplitudes of the two mechanisms are of opposite sign: whereas one process gives rise to enhancement at, e.g., 14.5 μs, the other induces current quenching. It is important to understand that the transient data in Fig. 4.3 b) proves that the conductivity is influenced by two *uncorrelated* spin-dependent processes. However, it does not prove that either one of these channels is the TEP mechanism

4.2.3 Coherent "Rabi–beating" spectroscopy

To distinguish and understand the qualitative nature of the two spin-dependent mechanisms, the influence of the B_1 microwave driving field duration and strength on the ΔI transient has been investigated. The clearest evidence to date for the PP mechanism in spin-dependent processes has come from the observation of coherent spin-beating Rabi flopping in the current of a balanced OLED device [18]. Since the PP are weakly spin-coupled, the application of an on-resonant microwave pulse B_1 drives the rotation of only a single spin-1/2 species within the pair if $B_1 < \langle |B_{Hyp}| \rangle$, or the average difference in hyperfine field experienced by electron and hole. This rotation gives rise to a simple modulation of the current at the primary Rabi frequency γB_1. If the magnitude of the driving microwave field B_1 exceeds $\langle |B_{Hyp}| \rangle$, both carriers precess in phase, and spin beating occurs at twice the Rabi frequency. It

is this beating signature which offers a route to differentiating between the two mechanisms in the imbalanced devices. The first demonstration of this beating effect was given by McCamey et al. [18] who attributed this observation to polaron pairs (weakly spin coupled pairs of s=1/2 consisting of oppositely charged polaron states controlling recombination) in MEH-PPV; however, this effect has also been seen in currents of MEH-PPV/PCBM blends [26], where it was attributed to to bipolaron pairs (weakly spin coupled pairs of s=1/2 consisting of equally charged polaron states controlling transport) in the MEH-PPV phase. The discrepancy between these two interpretations of the unambiguously observed pairs of s=1/2 has recently been resolved by the test of both models using optically detected magnetic resonance showing that the observed beat effect governs recombination, and is therefore due to polaron pairs with opposite charge [27]. In the following, the beat effect is used to distinguish spin-dependent transport channels involving two carriers from those involving only one.

Fig. 4.4 a)-e) shows the details for an electron-dominated OLED, the enhancement-quenching-enhancement $\Delta I(t)$ transient following the microwave pulse, as a function of the pulse length, for $B_1 = 1.4\text{mT} > \langle |B_{Hyp}| \rangle$ [18]. Rabi flopping and beating is seen in the vertical slice of the plot at 27 μs (Fig.4.3 b)), consistent with the PP process. The lifetime of the Rabi oscillations is τ_{eh}'=100 ns, providing a lower limit for the spin phase coherence time. The Fourier transform (Fig. 4.4 c)) shows two frequency components, characteristic of beating. In contrast, the vertical slice taken at 8μs (Fig. 4.4 d) does not show beating: in this mechanism, which dominates at shorter times, only one spin-1/2 carrier is involved with a longer Rabi-flopping lifetime, τ_e'=225ns. The corresponding Fourier transform (Fig. 4.4 e)) reveals no higher harmonics in the spin precession. As well as electron-hole pairs, spin beating is also conceivable for electron-electron or hole-hole pairs (bipolarons), although this would occur with different B_{Hyp} magnitudes and can be excluded based on the data (see appendix). No beating is seen for driving fields exceeding $\langle |B_{Hyp}| \rangle$, indicating that the signal is either due to a single spin-1/2 carrier, or occurs with a partner which has a resonance at a substantially different magnetic field. The only other observed

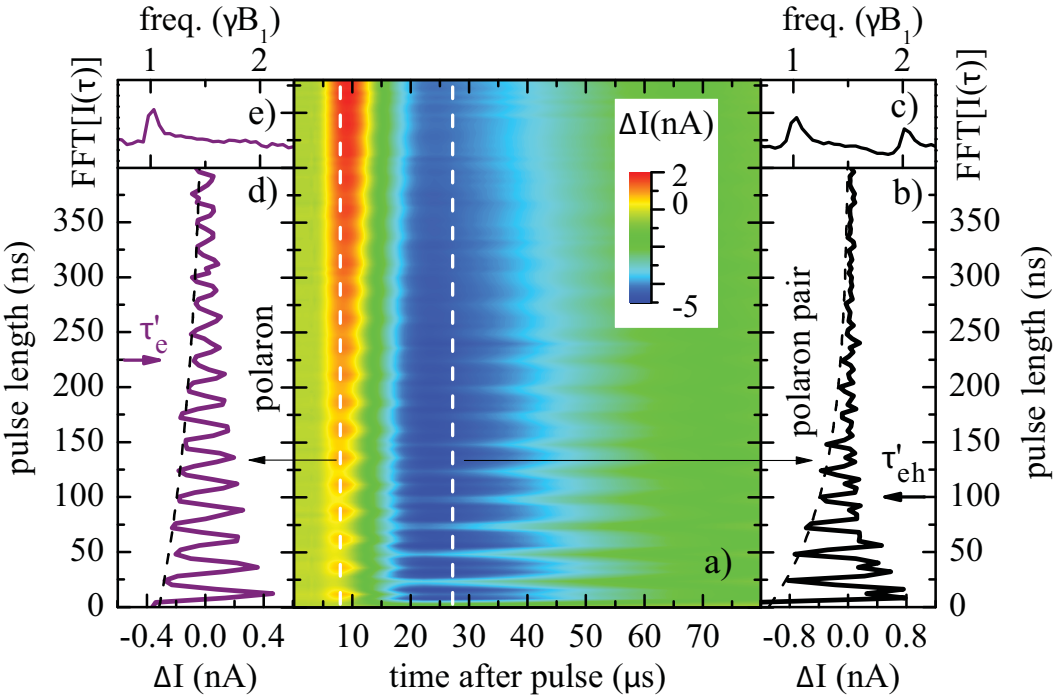

Figure 4.4. Rabi flopping in the current of an electron-dominated device at 10 K. The differential current on resonance (B_0=345.5 mT) is plotted as a function of the microwave pulse duration and time after the pulse. During the application of the microwave (B_1) field spin precession occurs, leading to Rabi flopping in the current along the vertical graph axis. At short times after B_1 application single-frequency Rabi flopping is seen - the TEP mechanism (left panel; Fourier transform inset above). At longer times, spin beating arises in the PP process (right panel) with a harmonic in the Fourier transform (top right).

resonance in the system, the triplet half-field signal, is an obvious candidate. This hypothesis is supported by the time transient recorded following a microwave pulse resonant with the triplet at half field (not shown), which also leads to a current enhancement displaying a temporal dependence very similar to that of the additional enhancement seen at full field in the electron-rich device (Fig. 4.4). Note that the observations shown in Fig.4.4 as well as the half-field resonance safely exclude other spin-dependent transport processes that have been hypothesized in the literature (see appendix) and that are also described in the appendix. Only the properties of the TEP mechanism are found to be consistent with the observed spin-dependent conductivity behavior.

4.2.4 Half–field excitonic resonance

In order to further test the weakly-coupled TEP hypothesis, one can vary the temperature: at high temperatures, no half-field resonance is observed, possibly because triplet excitons decay more readily by thermally-activated non-radiative means and the triplet density is therefore much lower [9]. At full field, spin nutation is detected at both high and low temperatures; the 10K nutation is shown in Fig. 4.4. At room temperature (not shown), where no half-field resonance is seen, the ratio between fundamental and harmonic amplitude in the full-field Rabi flopping depends solely on the strength of B_1 and the hyperfine interactions [18], which do not change with temperature. As the temperature is reduced, the part of the signal corresponding to spin-1/2 nutation increases, and is clearly correlated with the increasing intensity of the half-field resonance shown in Fig. 4.5, providing further evidence that the two signals arise from the same physical process, the TEP interaction. The points labeled (ff) in the Fig. 4.5 inset are amplitudes of the spin-1/2 Rabi oscillation extracted from measurements of the Rabi flopping versus the real-time transient of the device current at each temperature (i.e. plots analogous to Fig. 4.4). These Rabi oscillation measurements allow removal of the contribution from the PP process, resulting in a corrected spin-1/2 oscillation amplitude due exclusively to the single carrier (non-PP) process. With the TEP mechanism identified, one can now focus

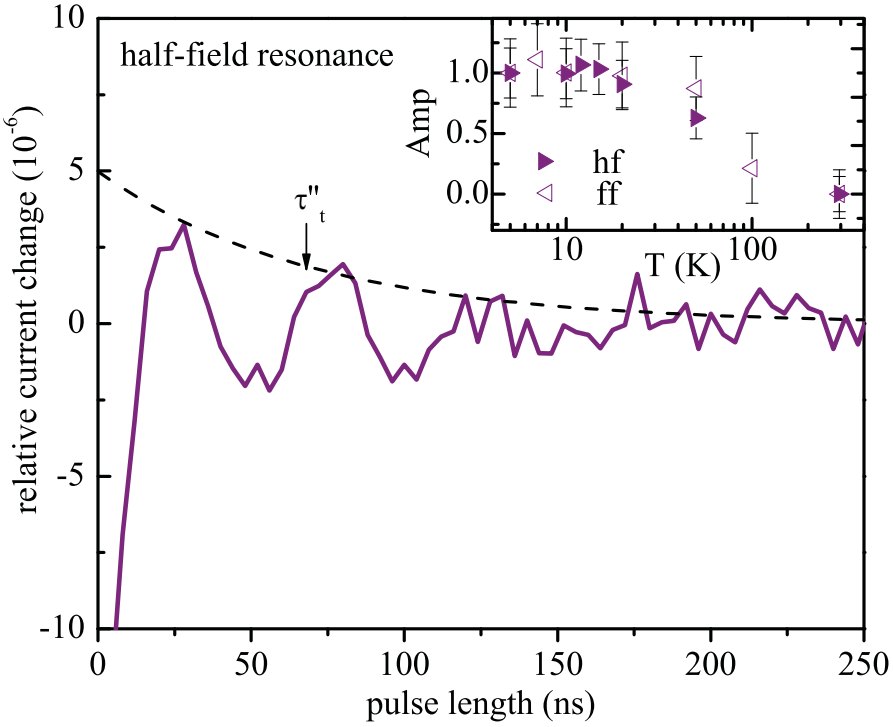

Figure 4.5. Spin-1 (triplet) half-field Rabi flopping in the electron-rich device. As the temperature increases, both the half-field resonance amplitude (hf) and the corrected amplitude of the nonbeating component of the full-field resonance (ff) disappear (upper inset).

on the intriguing question of the actual spin phase coherence of the triplet exciton itself. Fig. 4.5 shows half-field Rabi flopping in the OLED current as a function of pulse length. Here, only processes involving triplet excitons (S=1) are detected due to spin-resonant transitions between the triplet T_+ and T_- levels. Both the full and half-field Rabi frequencies are proportional to B_1 (not shown), and the ratio of the frequencies $\Omega_{Full}/\Omega_{Half} \approx 2.1 \pm 0.7$. The coherence time extracted from the decay of the Rabi oscillation amplitude τ"=60 ns is shorter than the single spin-1/2 time τ_e' =225 ns noted in Fig. 4.4, indicating faster spin dephasing as expected in the strongly-correlated electron-hole pair constituting the triplet exciton. The difference between these times contradicts the strongly spin-spin coupled triplet-polaron pair (trion) hypothesis [16], which should exhibit identical dephasing times. However, the difference between τ' and τ'' is consistent with a weakly spin-spin coupled pair comprising a triplet exciton and a polaron. As the zero-field matrix of the triplet exciton is strongly anisotropic, most of the randomly-oriented triplet states will be slightly off-resonance under half-field excitation, and thus coherent dephasing of the triplet ensemble significantly faster than the dephasing of the polaron is expected.

4.3 Exclusion of models

With the evidence of different spin-dependent channels given, the coherent spin-Rabi nutation experiments revealing different nutation frequencies at different detection time was conducted in order to elucidate the nature of the different spin-dependent signals (see Fig. 4.4 for data). As explained above, one of the observed nutation signatures is in agreement with the polaron-pair mechanism, identical to the sole process seen in the charge balanced device. The nutation signature of the other process is in agreement with the triplet exciton-polaron process. The observed data refutes alternative explanations for this second observed nutation signature. As also explained in detail in above, the spin-nutation experiments produced the following observations: In the electron-rich device a strong "half-field" resonance is detected, which is indicative of a strongly-coupled triplet exciton. At full field in the electron-rich device, a strong single spin-1/2 signal (Fig. 4.4) dominates the

transient current behavior at $\sim 8\mu$s after a resonant microwave pulse. This is not seen in the balanced device at any temperature. Reducing the temperature leads to an increase in the half-field resonance and a correlated increases in the full-field spin-1/2 signal (Fig. 4.5 inset). The inconsistency of these observations with spin-dependent mechanisms other than the triplet-polaron mechanism are discussed in the following on a case-by-case basis.

4.3.1 Single spin 1/2 process

With the observation of the single spin-1/2 signal at full field, the first and simplest model to consider would be a spin-dependent process involving only the single spin-1/2 carrier. This may be due, for example, to spin resonantly manipulated hopping rates. Transport in disordered organic materials is governed by thermally assisted hopping through localized molecular sites. Due to the intrinsic disorder in the material, the next-nearest hopping site will be energetically offset by some amount ϵ. If this offset energy is more than the thermal energy kT then that hop is energetically unfavorable. However, with the application of an external magnetic field this offset could be partially compensated by the Zeeman splitting, thus leading to a greater probability of a hopping transition with a rate that is inversely proportional to the energy offset between the hopping sites. The population of these Zeeman states will follow Boltzmann statistics, so the change in the conductivity due to driven transitions between the states will increase as the temperature decreases. The signal for a spin dependent process resulting from a single spin must be proportional to the square of the thermally driven spin polarization [28]. This expected polarization dependence is not seen experimentally (Fig. 4.5, inset); instead, a constant value which persists over a large temperature range is seen. Furthermore, the signal strengths predicted by a single spin model are more than two orders of magnitude too small [28] when compared to the signals seen in these experiments. Thus, a spin dependent process involving a single spin cannot explain the data and, therefore, it can be excluded. This model does also not predict the presence of a signal at half field.

4.3.2 Second PP process with different dynamics

One hypothesis to account for the presence of a second spin-dependent channel next to the previously confirmed polaron pair signal is to assume the presence of a second polaron pair channel with different recombination dynamics. In the electron rich devices, a shift of the recombination zone toward the anode could also imply a shift of electronic and spin relaxation times. Since polaron pairs consist of two weakly coupled spins with s=1/2 similar to the bipolaron pairs, the same arguments exclude this possibility. The observed spin-dependent process should display beating at B_1-fields above 1.1mT at the most. This is not seen experimentally and thus this hypothesis can be excluded.

4.3.3 Bipolaron

The bipolaron interaction [2] involves the weakly coupled pair of two same-charged carriers. The model consists of a free carrier passing through an already occupied site. The mobility through the site is proportional to the overall singlet content of the pair, leading to a Pauli-blocking mechanism. This interaction could become more prevalent in the case where there is a large carrier imbalance. One would expect different dynamics than for the polaron-pair mechanism and thus a clearly distinguishable second signal would be seen. This model involves the interaction of two weakly coupled spins in pairs of either two electrons or two holes (pair of two s=1/2), and a beating in the Rabi nutation signal should be seen once the driving field is comparable to the average difference in the local hyperfine fields between the pairs. Since the pair consists of either e-e or h-h, this average difference would be approximately the width of the respective resonance. In these experiments it is the narrower resonance which displays the additional Rabi nutation signal. This resonance has a width of $\sim$8 G, and after the application of a driving field of more than 14 G the signal still shows no beating component. Thus, the bipolaron mechanism can be excluded as the origin of the observed signal. As with the single spin model, the triplet exciton resonance seen in the data is not predicted by the bipolaron model, either.

4.3.4 Trion recombination

The trion [29] or charged-exciton is usually described in terms of an exciton and "free" charge residing on the same molecular chain. This high degree of locality between the two entities leads to a strong exchange coupling interaction. Under spin resonance, both a full-field and half-field resonant change in detected current would be observed, as the overall transition rate is proportional to the spin-1/2 or "doublet" content of the combined spin-1 + spin-1/2 (or spin-3/2) wavefunction. This rate can be manipulated by either driving the triplet or the polaron resonances of the trion, although due to the coupling, both the exciton and polaron will always nutate. The observed current change would be a result of an excited polaron with higher mobility after the Auger-like process described above. However, due to the strong exchange coupling, the Rabi-nutation expected for this s=3/2 system at full field would not simply reflect the rotation of a single polaron with frequency γB_1. Instead, the nutation would occur with a primary frequency $\sqrt{3}\gamma B_1$ [30]. An s=1/2 nutation at γB_1 is not present in this system (see Fig. 4.4) and thus this hypothesis can be excluded.

4.3.5 Triplet-triplet exciton annihilation

At high triplet-exciton concentration, triplet-triplet interactions are expected [1], and have indeed been reported before in organic devices. The interaction can change many experimental observables, including both the current and the luminescence. Under resonance of the triplet pair, there is a certain probability to annihilate the triplets and produce, due to spin conservation, a singlet ground state along with a weakly coupled polaron-pair. This would modify the current by changing the density of the overall polaron pair population, and thus would be observed through the intrinsic differences in triplet and singlet polaron dissociation rates. If the triplets were interacting as a weakly coupled pair, or the fine-structure term of the overall triplet-triplet Hamiltonian were negligible, the Rabi-nutation frequency expected at full field would be due to the transition of just one of the spin-1 pair partners. If the pair were strongly coupled, a full field signal would be seen with a Rabi-nutation

frequency of $2\gamma B_1$ and a beating frequency of $\sqrt{6}\gamma B_1$ [30] at high B_1 strengths due to the Δm=$\pm$1 transitions within the five states of a strongly coupled S=2 pair. One can see only a γB_1 Rabi-nutation frequency for all applied driving field strengths. This is not expected from this model, and thus, one can safely exclude triplet-triplet annihilation and the trion model as an explanation of the observed electrically detected signal.

4.3.6 Triplet-exciton polaron(TEP)

The TEP mechanism results from the interaction between a triplet exciton and a free polaron [3, 4]. The process is similar to the trion; recombination leads to an excited free polaron with a higher mobility. However, unlike the trion process, the two pair partners are weakly spin coupled. The spin-dependency of the triplet recombination results from the transition of the 6-state manifold of the s=1/2 - s=1 pair into a doublet [singlet s=0 /s=1/2] system. The occurrence of a half-field resonance is predicted due to the Δm=$\pm$2 transitions within the triplet manifold, which become allowed due to strong dipolar interaction within the exciton. The resonance at half-field affects the recombination rate and, thus, the current. Finally, a single spin-1/2 or γB_1 Rabi-nutation frequency at full-field due to the Δm=$\pm$1 transitions of the free polaron is also expected. In contrast to the other mechanisms discussed above, the presence of the correlated s=1/2 and s=1 nutation components in the presented data is consistent with the TEP model.

4.4 Conclusions

In conclusion, a conductivity signature of the TEP process in MEH-PPV has been identified which becomes significant below $\sim$100 K. Under magnetic resonance, the conductivity can be manipulated due to this process. Measuring the phase coherence and spin lifetimes of the triplet exciton using this approach offers a way to directly study the role and influence of the often elusive triplet excitons in purely hydrocarbon organic semiconductors. The direct coherent manipulation of the triplet exciton (Fig. 4.5) combined with electrical readout provides a further intriguing avenue to

classical and quantum spin information concepts in the limit of extremely strong exchange coupling which is not available in inorganic semiconductors.

4.5 References

[1] C. E. Pope, M. & Swenberg, *Electronic Processes in Organic Crystals and Polymers*, Clarendon, 1982.

[2] P. A. Bobbert, T. D. Nguyen, F. W. A. van Oost, B. Koopmans, and M. Wohlgenannt, Phys. Rev. Lett. **99**, 216801 (2007).

[3] V. Ern and R. E. Merrifield, Phys. Rev. Lett. **21**, 609 (1968).

[4] Y. Meng, X. J. Liu, B. Di, and Z. An, The Journal of Chemical Physics **131**, 244502 (2009).

[5] V. A. Dediu, L. E. Hueso, I. Bergenti, and C. Taliani, Nat Mater **8**, 707 (2009).

[6] E. L. Frankevich et al., Phys. Rev. B **46**, 9320 (1992).

[7] J. Kalinowski, J. Szmytkowski, and W. Stampor, Chemical Physics Letters **378**, 380 (2003).

[8] J. M. Lupton and C. Boehme, Nat Mater **7**, 598 (2008).

[9] M. Reufer et al., Nat Mater **4**, 340 (2005).

[10] G. Salis, S. F. Alvarado, M. Tschudy, T. Brunschwiler, and R. Allenspach, Phys. Rev. B **70**, 085203 (2004).

[11] M. P. Delmo, S. Yamamoto, S. Kasai, T. Ono, and K. Kobayashi, Nature **457**, 1112 (2009).

[12] U. E. Steiner and T. Ulrich, Chemical Reviews **89**, 51 (1989).

[13] M. Wohlgenannt, K. Tandon, S. Mazumdar, S. Ramasesha, and Z. V. Vardeny, Nature **409**, 494 (2001).

[14] M. Wohlgenannt, W. Graupner, G. Leising, and Z. V. Vardeny, Phys. Rev. Lett. **82**, 3344 (1999).

[15] L. S. Swanson et al., Phys. Rev. B **46**, 15072 (1992).

[16] M.-K. Lee, M. Segal, Z. G. Soos, J. Shinar, and M. A. Baldo, Phys. Rev. Lett. **94**, 137403 (2005).

[17] D. R. McCamey, S.-Y. Lee, S.-Y. Paik, J. M. Lupton, and C. Boehme, Phys. Rev. B **82**, 125206 (2010).

[18] D. R. McCamey et al., Phys. Rev. Lett. **104**, 017601 (2010).

[19] D. R. McCamey et al., Nat Mater **7**, 723 (2008).

[20] E. J. W. List et al., Phys. Rev. B **64**, 155204 (2001).

[21] M. Gross et al., Nature **405**, 661 (2000).

[22] J. Scott, S. Carter, S. Karg, and M. Angelopoulos, Synthetic Metals **85**, 1197 (1997).

[23] Y. Cao, G. Yu, C. Zhang, R. Menon, and A. J. Heeger, Synthetic Metals **87**, 171 (1997).

[24] J. C. Scott et al., Hole limited recombination in polymer light-emitting diodes, 1999, journal article.

[25] N. Atherton, M. Davies, B. Gilbert, and A. Davies, *Electron Spin Resonance*, Electron spin resonance, Royal Society of Chemistry, 1996.

[26] J. Behrends et al., Phys. Rev. Lett. **105**, 176601 (2010).

[27] S.-Y. Lee et al., J. Am. Chem. Soc. **133**, 2019 (2011).

[28] C. Boehme, *Dynamics of spin-dependent charge carrier recombination*, PhD thesis, Philips-Universitat Marburg, 2002.

[29] V. M. Agranovich et al., Chemical Physics **272**, 159 (2001).

[30] A. V. Astashkin and A. Schweiger, Chemical Physics Letters **174**, 595 (1990).

CHAPTER 5

SLOW HOPPING AND SPIN-DEPHASING OF COULOMBICALLY BOUND POLARON PAIRS IN AN ORGANIC SEMICONDUCTOR AT ROOM TEMPERATURE

One of the important but still unresolved questions about organic semiconductors [1] is on what length scales ballistic spin diffusion [2] is possible. There have been many claims of spin polarized injection and spin transport across large distances (≈100nm) in organic semiconductors, most of which come from experimental studies conducted on organic spin valves which clearly show electric switching when the ferromagnetic domains at the contact layers are changed by coercive magnetic fields. In spite of this effect, it is not known whether or not the mechanism responsible for this switching behavior is ballistic spin diffusion or whether other effects (spin-dependent interface transitions, spin-dependent hopping) could be responsible. Most the the skepticism about organic spin-diffusion is based on the still lacking demonstration of the Hanle effect, the observation of spin–precession of diffusing spins when a magnetic field perpendicular to the injection polarization is applied [3, 4].

In this chapter (that has been reprinted from a manuscript that is to be published in *Physical Review Letters* and has been coauthored by Dane McCamey, Tom Keevers, Christoph Boehme and John Lupton.[1]) electrically-detected spin echoes arising from direct quantum control of polaron pair spins in an organic light-emitting diodes (OLED) at room temperature are presented. This approach reveals phase coherence

[1]W.J. Baker,T.L. Keevers,J.M. Lupton, D.R. McCamey and C. Boehme, Slow hopping of coherently coupled polaron pairs in an organic semiconductor at room temperature, Phys. Rev. Lett., to be published (2012). Copyright 2012 by the American Physical Society. Reprinted with permission from the American Physical Society

on a microsecond timescale, and offers a direct way to probe charge recombination and dissociation processes in organic devices, revealing temperature-independent intermolecular carrier hopping on slow timescales. The knowledge of both longitudinal as well as transverse spin-relaxation times in MEH-PPV will give insight into why the Hanle effect has not been observed in organic semiconductors. In addition, the spin phase coherence times at room temperature revealed in the course of this study is also of potential interest for the development of quantum-enhanced sensors and information processing systems, which operate at room temperature.

5.1 Electrically detected Hahn echoes

In this chapter, electrically detected spin-Hahn echo experiments are demonstrated that one can use for the measurement of spin phase coherence lifetimes. As illustrated in Fig. 5.1, by using the pair's internal quantum phase as a probe, the motion of polarons within a pair through the random magnetic environment arising from the Overhauser field of the polymer's nuclear spins can be determined. We show that after coherence has been encoded into the spin pairs the phase information can be recovered as long as the polaron remains on a particular segment of the polymer chain during the measurement. However, if there is a hopping or tunneling event to a nearby unit the phase coherence is nonrecoverable due to the changed orientation of the local Overhauser field, since there is no long-range correlation of nuclear spins [5]. This migration of an individual charge carrier leads to a measurable decay in spin echo amplitude of the ensemble.

Here pEDMR [6,7] is performed on devices consisting of a an organic π -conjugated polymer poly[2-methoxy-5-(2'-ethylhexyloxy)-1,4-phenylene vinylene] (MEH-PPV), similar to devices previously studied [5, 8] . The polymer was incorporated into an OLED with indium tin oxide (ITO) and Calcium electrodes, as well as a hole injection layer of poly(3,4-ethylenedioxythiophene) (PEDOT) for balanced hole injection [9]. The use of pulsed EDMR is a particularly appropriate technique for investigation of coherent dynamics in organic materials, as the spin dynamics are set solely by the microwave pulses, whereas any variation in the RC timescales of the device

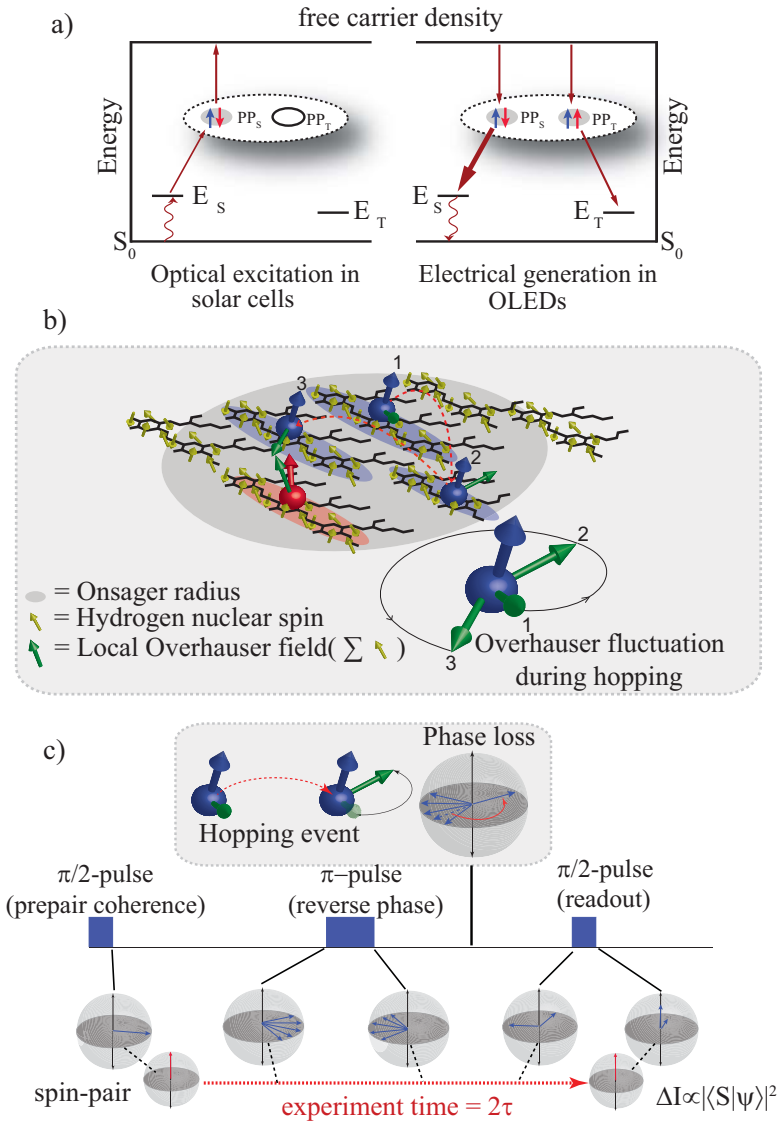

Figure 5.1. a) Illustration of the PP process discussed in Chapters 1 to 4. The important step for recombination is the PP, a state that is accessible by pEDMR. PPs exist both in the singlet (S) and triplet (T) configuration and can couple to excitons at energies E_S, E_T. b) An electron (blue) and hole (red) form a carrier pair. As charges hop from site to site within the Onsager radius of the Coulombically-bound pair, they experience an effective temporal fluctuation in the local magnetic field, even when the nuclear spin ensemble is quasi-static. The decoherence time therefore places an upper limit on the intersite hopping rate of charges within a pair. c) The measured loss of phase coherence within a pair can be seen as a hopping event to a new Overhauser site during the spin-echo sequence, where the current change ΔI is proportional to the singlet content of the wavefunction.

only impact the readout timescale [7, 10]. The correspondence between electrically and optically detected pulsed electron spin resonance experiments [11] on similar structures indicates that the polaron pairs seen in this work are oppositely charged. However, this method may also be of use for materials which contain bipolaron pairs [12] (pairs of like-charge polarons), or other more complex spin pairings [8].

Recently, it was shown that controllably perturbing the spin state of the polarons which comprise polaron pairs directly modifies both the conductivity [13] and luminescence of an OLED [11]. Although conventional electron spin resonance is used to manipulate the spins, the change in optoelectronic properties is sensitive to singlet and triplet spin configuration within the pairs, and not to the ensemble magnetization, as is usually the case in electron spin resonance [14]. Because of this, the measurement is sensitive to the dynamics of the intermediate state, the polaron pair. However, a number of challenges remain if this technique is utilized to understand the process which limits polaron pair coherence in devices. First, the simple Rabi oscillations shown in Ref. [13] provide only a lower limit on the spin phase coherence time, and as a result do not allow us to determine the microscopic processes limiting spin phase coherence. Second, the measurements reported in Ref. [13] were undertaken at low temperatures. In the following, electrically-detected Hahn echo sequences are demonstrated to directly measure the phase coherence time at room temperature, under conditions much more similar to those in which devices operate. The echo sequence provides the basis for a computational model to simulate polaron pair spin decoherence, allowing us to extract an estimate of the hopping transport timescale of polarons bound in polaron pairs in the organic semiconductor MEH-PPV.

5.2 Decoherence mechanism

The first question that is addressed here is how long the spin ensemble retains memory of its phase. Spin relaxation can be either longitudinal or transverse. In interpreting the transient response of the spin-dependent (electrically-detected) resonance signal, it is important to distinguish pure decoherence (an irreversible loss in quantum phase information over time T_2) from simple dephasing (a situation where the phase

relationship within an ensemble of spins becomes unknown due to either a reversible or an irreversible process over time T_2^*). Following a recent demonstration at low temperatures1, coherent evolution of the carrier pair spins was measured at room temperature, yielding Rabi oscillations observed in the device current (not shown), much like what is discussed in Ref. [5]. The oscillations are exponentially damped with a time constant $T_2^* \approx 123$ns. However, this damping arises due to phase variations within the pair resulting from the spatial inhomogeneity in the Overhauser field $B_H(x)$ as well as the limited homogeneity of the resonant driving field B_1, and not solely due to the intrinsic phase relaxation, providing only a lower limit to the true decoherence time. This coherent phase loss due to the $B_H(x)$ and B_1 inhomogeneities can be undone with a first-order decoupling scheme, in this case a modified version of the Carr-Purcell echo sequence [15], leaving only the dephasing effects due to irreversible processes. The experiment is implemented as follows [16] (Fig 5.1 c)): with the external static magnetic field B_0 defining the z-axis and after approach of the steady state, which is dominated by triplet pairs due to the much longer triplet lifetime, an on-resonance microwave $\frac{\pi}{2}$ -pulse is applied. This pulse rotates one (or both) of the spins of the pair into the transverse plane. Once in the x-y plane, the spins precess around a transverse field $B_T(x) = B_0 + B_H(x)$. The spatial inhomogeneity of the hyperfine field $B_H(x)$ leads to a coherent dephasing of the ensemble, with those spins experiencing the larger $B_T(x)$ precessing faster. After a delay time τ a π-pulse is applied, equal in magnitude and frequency to the first, but of twice its duration. Those spins experiencing a larger $B_T(x)$ now lag spins with a smaller $B_T(x)$ in their precession, such that at a time τ after the second pulse all the spins regain the same relative phase. If the observable were the polarization, as in standard ESR, one would simply see an increase in magnetization in the form of an echo (a Hahn-echo) at a time τ after the π-pulse. However, since one can not detect changes in current due to variations in the spin-singlet content of the ensemble, a magnetization rephasing will not lead to current changes unless an additional $\frac{\pi}{2}$ -pulse is added, a readout pulse, to project the rephased state back onto the z-axis [17]. When the time between pulses, τ is increased, a corresponding decrease in the observed echo current signal is seen

due to irreversible loss of phase information during the time 2τ (Fig. 5.2).

A simple exponential describes this dephasing with a true phase coherence time, $T_2 = 348(18)$ns at room temperature. Upon cooling to 10K, T_2 increases to 611(44)ns, a mere factor of 2 difference from the room temperature value.

Loss of spin phase coherence due to recombination or dissociation of spins in the ensemble, or irreversible spin flips due to spin-orbit interactions, can be discounted as the source of decoherence, since the spin lifetime should also be limited by such a process [10]. However, a lower limit for the spin lifetime of $T_1 > 36\ \mu\text{s} \gg T_2$ is observed from the transient current response to an on-resonance pulse [10], allowing us to exclude this mechanism of rapid spin flips. Decoherence could arise due to spin-dipolar interactions between charge carriers, but would have to display a significant dependence on current density due to an increase in the local magnetic field fluctuations caused by elastic and inelastic scattering events [18]. However, after a large change in device current there is no effect found on the measured spin-echo coherence time (Fig. 5.2 inset), indicating that spin-spin interactions are not likely responsible for decoherence. Decoherence resulting from a temperature-activated Orbach process, a two-phonon event involving an excited state [19], is also unlikely given the small change in coherence time with temperature (blue data point in the inset of Fig. 5.2). Therefore, it is concluded that decoherence arises due to hopping of the carrier pairs or of one of the pair partners in the inhomogeneous distribution of nuclear Overhauser fields, $B_H(x)$.

5.3 Simulation of hopping pairs

To investigate the influence of hopping on the measured phase coherence time, a numerical simulation of the evolution of an ensemble of polaron pairs during application of an echo sequence was carried out. As a measure of coherence, we find the probability of the polaron pair returning to the initial state (either $T^+ = |\uparrow\uparrow\rangle$ or $T^- = |\downarrow\downarrow\rangle$) after an echo sequence is applied. To include the influence of hopping, a simplified Overhauser field environment is generated for each spin pair, consisting of a 5 x 5 x 5 grid of sites. This approach is motivated by the recent work by Kersten et

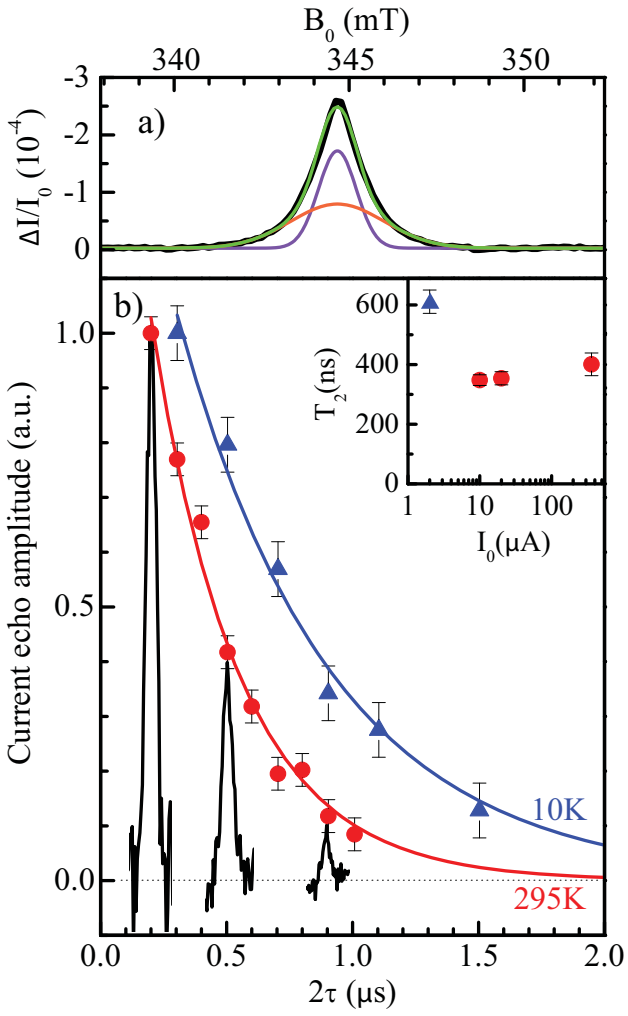

Figure 5.2. Experimentally observed magnetic resonance spectrum and spin echoes. a) The spectrum is described by two Gaussians (orange, purple lines) representing the hyperfine field-broadened resonance of electron and hole (sum of Gaussians: green line). b) Using a Carr-Purcell (CP) spin-echo pulse sequence as described in Fig. 5.1 c), the effect of spin dephasing can be removed, providing a measure of the intrinsic phase coherence time T_2. The three black curves show CP echoes scaled to the time axis. The echo intensity follows an exponential decay with time and depends only weakly on temperature. All measurements were performed at 295K unless otherwise marked. The inset shows T_2 values at different device currents to exclude the possibility of current-induced dephasing.

al. [20] where each molecular site is assigned a random Overhauser field,$B_H(x)$, and a specific site energy, drawn from random Gaussian distributions (FWHM$_{electron}$ = 0.96mT and FWHM$_{hole}$ = 2.15mT) taken from literature [5, 21, 22]. The spins may hop independently to nearest-neighbor sites in a stochastic manner. The characteristic hopping time in transport may be varied by modifying the hopping attempt frequency. The characteristic hopping time t_{hop} denotes the time between hops of either spin in the pair. In this work, these two hopping rates have been set to be equal, such that the characteristic hoping time of a single spin is $2t_{hop}$. The spatially varying Overhauser field obtained is then incorporated into the echo simulation.

For a fixed t_{hop} , the echo simulation is performed for a large number of echo times, 2τ. An example is shown in the inset of Fig. 5.3 a). The decoherence data generated follows an exponential decay yielding a characteristic coherence time T_2^{Sim}. Fig. 5.3 a) shows the decay time obtained for a range of different hopping times. As the figure reveals, at slow hopping times T_2^{Sim} is equal to the hopping time plus the dephasing time expected due to the change in magnetic environment after a hopping event; $T_2^{Sim} = t_{hop} + t_d^0$, where $t_d^0 = \frac{1}{g\mu_B B_H^{1/2}(x)}$ is determined by the FWHM, $B_H^{1/2}(x)$, of the Gaussian distribution of hyperfine fields $B_H(x)$. However, when the hopping time becomes shorter than the time required for dephasing due to the randomization of the environment after every hop, the decay time T_2^{Sim} is found to increase rapidly. This counterintuitive effect is a process known as motional narrowing, whereby the rapid change in random Overhauser fields due to fast hopping leads to a time-averaged *reduction* in the effective disorder. This phenomenon can be accounted for by equating $T_2^{Sim} = t_{hop} + t'_d$, with $t'_d = t_d^0(1 + t_d^0/t_{hop})$. The simulated data in Fig. 5.3 a) are accurately described by this analytical result (grey line).

As a result of the motional narrowing, there are two hopping times that are compatible with the experimentally observed decoherence time at room temperature - $t_{hop} \approx T_2$=320ns , and $t_{hop} \approx 10^{-11}$s $\ll T_2$. However, it is possible to distinguish between these two cases by considering the linewidth of the resonance shown in Fig. 5.2 a), which provides a measure of the local Overhauser field. Fig. 5.3 b) plots the calculated line width, $\Delta B' = \frac{1}{2}(\frac{1}{2\pi g\mu_B t'_d})$, as a function of the hopping rate.

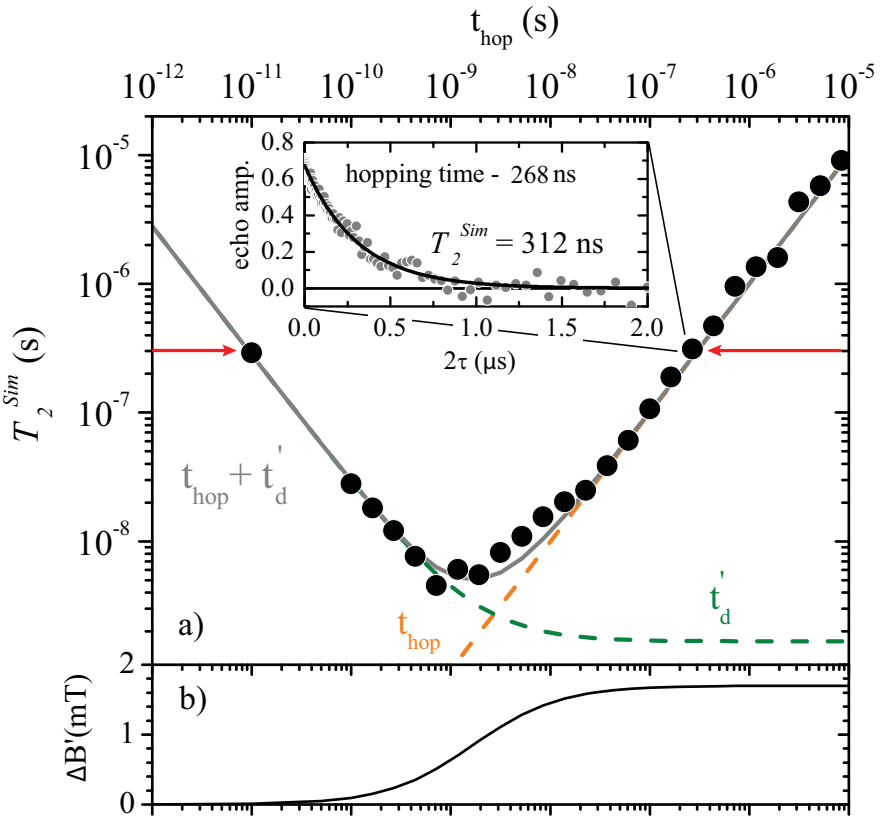

Figure 5.3. Computational modeling of the expected echo decay time T_2^{Sim} as a function of polaron hopping time for an ensemble of polaron pairs. The inset shows the computed decay for a single hopping time, simulated for a number of different echo wait times 2τ. The echo is described by an exponential decay. a) The simulated decoherence time T_2^{Sim} is plotted in the main panel as a function of hopping time. For very short hopping times, T_2^{Sim} increases with decreasing hopping time due to motional narrowing. The simulated data are well described by the relation $T_2^{Sim} = t_{hop} + t'_d$, where t'_d describes on-site dephasing due to the local Overhauser fields estimated from the resonance line width. The modeled decay time coincides with the experimentally measured time of 320 ns for two hopping times (red arrows). b) The expected resonance line width depends on hopping time due to motional narrowing, providing a measure to differentiate between the two possible hopping times. Acknowledgment to D.R. McCamey and T.L. Keevers for the above simulation.

For slow hopping, the line width is set by the hyperfine disorder field, $B_H^{1/2}(x)$. For fast hopping, the line shape is motionally narrowed, and becomes increasingly small. If the faster of the two hopping times compatible with the experimental T_2 value is considered, one would expect a line width of approximately 0.01mT. However, this is substantially smaller than the $\approx$ 2mT linewidth seen experimentally (Fig. 5.2 a), and as such, one can exclude fast hopping as the source of the observed coherence decay. It is thus concluded that the hopping time in the MEH-PPV OLED measured here is approximately 320ns at room temperature, increasing only to 610ns at low temperature.

5.4 Discussion

The ability to observe this rich phase coherence behavior demonstrates the potential of using organic semiconductors for room-temperature electronics based on quantum coherence effects. More importantly, however, the method reveals surprising insight into elementary charge transport processes in these materials, which are hard to access by other means [23, 24] . Whereas transient electroluminescence and pump-probe spectroscopy [25] are nonequilibrium techniques probing the final step in carrier recombination and the first step in exciton dissociation, respectively, the experiments presented here are sensitive to the first step in recombination and the final step in dissociation, and thus report on equilibrium conditions.

These processes occur remarkably slowly (on the timescale of microseconds at room temperature) and must originate from a correlated carrier pair, since spin memory exists. In contrast, in transient absorption experiments, correlated pair recombination is often interpreted to occur swiftly, within tens of nanoseconds [25]. Seeing that such recombination poses a major loss channel in organic photovoltaic devices, it is helpful to be able to identify this process spectroscopically.

We note that during the phase coherence time T_2, the local spin bath is treated as quasi-static due to the much longer nuclear spin-flip times. This approximation allows limits to be placed on the time scale for conformational changes in the hydrogenated side chains, as well as the lifetime of nuclear spins, as both would lead to variations

of the Overhauser field felt by the carriers. In addition, the T_2 times pose a limit for intrapair charge hopping rates, since hopping of a carrier within a pair from one molecular site to another would lead to dephasing due to the randomly varying Overhauser fields. As the temperature is lowered, the size of the Coulombically-bound carrier pair increases. This Onsager radius is given by the balance of Coulomb and thermal energy. Since T_2 decreases only by a factor of two over a 30-fold increase in temperature, it is concluded that intrapair charge carrier hops are rare and only weakly thermally activated under equilibrium conditions. This surprising conclusion contrasts with the strong Arrhenius-type activation seen in (non-equilibrium) time-of-flight experiments [26]. On the other hand, if charge hopping occurs solely by tunneling and is not phonon assisted, no thermal activation should be observed. Such an absence of thermal activation is generally seen in photoconductivity [27], and has posed a long-standing puzzle to a quantitative description of charge transport in organic electronics. It is concluded that equilibrium carrier dynamics in organic semiconductors are inherently slow and very weakly thermally activated, pointing to a tunneling-type form of intersite coupling.

In summary, organic semiconductors exhibit surprisingly long pure spin coherence times at room temperature. Electrical access to spin coherence phenomena promises facile integration and scalability in quantum information architectures. In addition, spin coherence spectroscopy offers a new perspective on carrier migration in organic semiconductors, revealing the absence of thermally-activated hopping under equilibrium transport conditions in disordered materials.

5.5 References

[1] V. A. Dediu, L. E. Hueso, I. Bergenti, and C. Taliani, Nat Mater **8**, 707 (2009).

[2] A. J. Drew et al., Nat Mater **8**, 109 (2009).

[3] H. C. Koo et al., Science **325**, 1515 (2009).

[4] N. Tombros, C. Jozsa, M. Popinciuc, H. T. Jonkman, and B. J. van Wees, Nature **448**, 571 (2007).

[5] D. R. McCamey et al., Phys. Rev. Lett. **104**, 017601 (2010).

[6] C. Boehme et al., phys. stat. sol. (b) **246**, 2750 (2009).

[7] C. Boehme and K. Lips, Phys. Rev. B **68**, 245105 (2003).

[8] W. J. Baker, D. R. McCamey, K. J. van Schooten, J. M. Lupton, and C. Boehme, Phys. Rev. B **84**, 165205 (2011).

[9] M. Gross et al., Nature **405**, 661 (2000).

[10] D. R. McCamey, S.-Y. Lee, S.-Y. Paik, J. M. Lupton, and C. Boehme, Phys. Rev. B **82**, 125206 (2010).

[11] S.-Y. Lee et al., J. Am. Chem. Soc. **133**, 2019 (2011).

[12] J. Behrends et al., Phys. Rev. Lett. **105**, 176601 (2010).

[13] D. R. McCamey et al., Nat Mater **7**, 723 (2008).

[14] N. Atherton, M. Davies, B. Gilbert, and A. Davies, *Electron Spin Resonance*, Electron spin resonance, Royal Society of Chemistry, 1996.

[15] C. P. Slichter, *Priciples of Magnetic Resonance*, Springer, New York, third edition edition, 1989.

[16] S.-Y. Paik, S.-Y. Lee, W. J. Baker, D. R. McCamey, and C. Boehme, Phys. Rev. B **81**, 075214 (2010).

[17] H. Huebl et al., Phys. Rev. Lett. **100**, 177602 (2008).

[18] R. d. S. X. Hu and S. D. Sarma, *Foundations of Quantum Mechanics in the Light of New Technology*, World Scientific, 2003.

[19] J. W. Culvahouse and P. M. Richards, Phys. Rev. **178**, 485 (1969).

[20] S. P. Kersten, A. J. Schellekens, B. Koopmans, and P. A. Bobbert, Phys. Rev. Lett. **106**, 197402 (2011).

[21] T. D. Nguyen et al., Nat Mater **9**, 345 (2010).

[22] I. H. Nayyar et al., J. Phys. Chem. Lett. **2**, 566 (2011).

[23] M. Wohlgenannt, W. Graupner, G. Leising, and Z. V. Vardeny, Phys. Rev. Lett. **82**, 3344 (1999).

[24] L. S. Swanson et al., Phys. Rev. B **46**, 15072 (1992).

[25] T. Virgili et al., Phys. Rev. Lett. **90**, 247402 (2003).

[26] P. M. Borsenberger, L. T. Pautmeier, and H. Bssler, Phys. Rev. B **48**, 3066 (1993).

[27] V. I. Arkhipov, E. V. Emelianova, and H. Bssler, Phys. Rev. Lett. **82**, 1321 (1999).

CHAPTER 6

ROBUST ABSOLUTE MAGNETOMETRY WITH ORGANIC THIN-FILM DEVICES

Magnetic field sensors based on organic thin film materials have attracted considerable interest in recent years as they can be manufactured at very low cost and on flexible substrates. In spite of these advantages, the technological relevance of such magnetoresistive sensors is limited due to their narrow magnetic field ranges ($\approx$ 30mT) and the continuous calibration required to compensate temperature fluctuations and materials degradation. Conversely, magnetic resonance based sensors, which utilize fundamental physical relationships for extremely precise measurements of fields, are usually large and expensive. In this chapter, a technical application one of the spin–dependent processes discussed in the previous chapters is demonstrated. It is shown that an MEH-PPV can be used as an organic magnetic resonance based magnetometer, employing the PP process in an organic diode. This sensor combines the low cost thin film fabrication and integration properties of organic electronics with the precision of a magnetic resonance based sensor. It is shown that the device never requires calibration, operates over large temperature and magnetic field ranges, is robust against materials degradation, and allows for absolute sensitivities of less than 50 nT $Hz^{-1/2}$. This chapter[1]. is reprinted from a manuscript that is to be published in *Nature Communications* and has been coauthored by K. Ambal, D. P. Waters, R. Baarda, H. Morishita, K. van Schooten, D.R. McCamey, J. M. Lupton and C. Boehme.

[1]W.J. Baker, K. Ambal, D. P. Waters, R. Baarda, H. Morishita, K. van Schooten, D.R. McCamey, J. M. Lupton and C. Boehme; Robust absolute magnetometry with organic thin-film devices; to be published in Nature Communications. Copyright 2012 by the Nature Publishing Group. Reprinted with permission from the Nature Publishing Group

6.1 Traditional magnetometry approaches

Measuring absolute magnetic fields is crucial for many scientific and technological applications [1–3]ranging from physics to biology. While superconducting quantum interference devices address this issue for extremely weak magnetic fields [4], magnetic resonance (MR) based sensors allow the drift and offset-free determination of magnetic fields for intermediate to strong magnetic fields. MR magnetometers (MRMs) are based on bringing electromagnetic radiation into MR with paramagnetic centers whose Landé-factors are well known [5] and they exploit Planck's fundamental relationship between the frequency of the radiation and the Zeeman energy $\Delta E = h\nu = h\gamma B_0$ of the paramagnetic centers to determine a magnetic field(γ being the gyromagnetic ratio, B_0 the applied magnetic field, and h the Planck constant). The drawback of MRMs is their cost and bulkiness: conventional radiation detected MR requires large volumes (up to hundreds of cm^3) [5, 6] and since MR signals disappear at low magnetic fields (due to the disappearance of spin polarization), MRMs are poor detectors even for intermediate magnetic field strengths. There have been several proposals to solve these drawbacks by using spin-dependent charge transport or recombination processes in semiconductors for the electrical (EDMR) or optical (ODMR) detection of MR [7–10] EDMR and ODMR signals usually do not depend on spin polarization [11] which makes them remarkably sensitive even at very low magnetic fields. In addition, they are not volume sensitive and so can be fabricated on nanoscopic size scales [12]. Previously proposed EDMR and ODMR based magnetometers were based on either silicon, whose spin-dependent signals are either non-present at room temperature [10] or very weak, or on nitrogen-vacancy centers in diamond, whose optical detection requires a fluorescence microscopy setup [9, 13, 14].

In this chapter, an MRM concept is described which combines the advantages of organic thin film electronic devices and traditional MRMs. Specifically, the spin–dependent PPs recombination in MEH-PPV has been investigated [15–17](Fig. 6.1).

Since this spin-dependent electronic transition governs the material conductivity, magnetic resonance with either electrons or holes can be detected simply by measuring

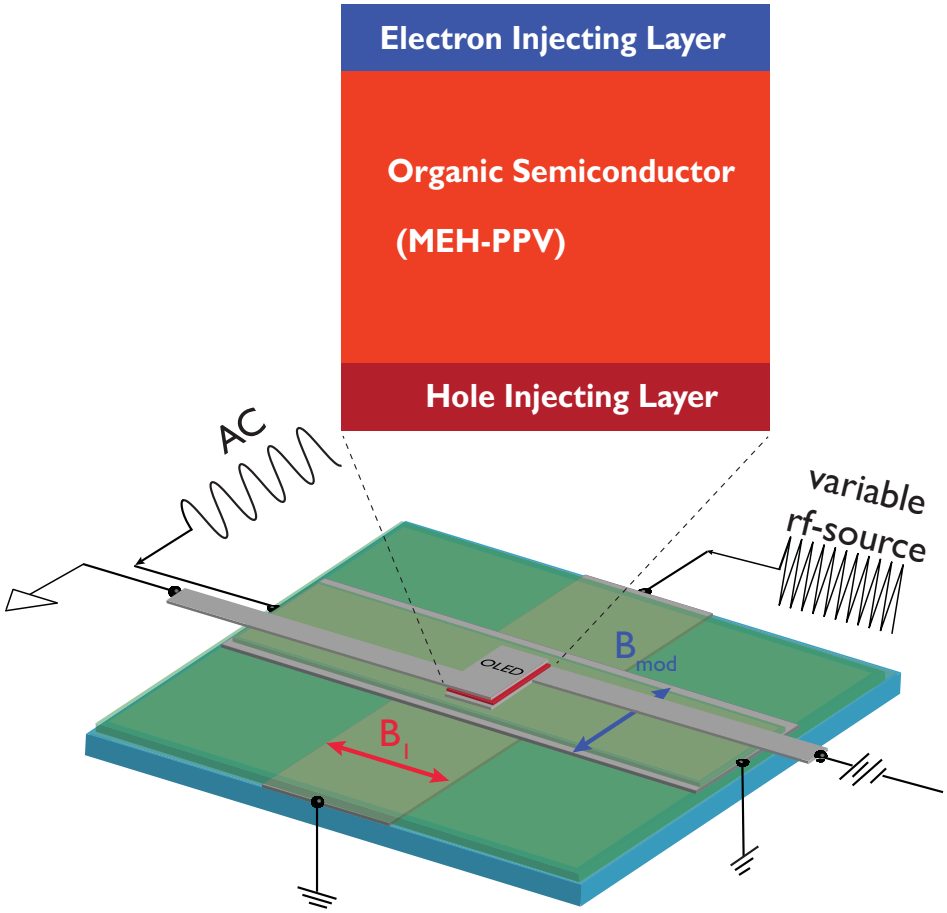

Figure 6.1. Device concept of an organic semiconductor magnetic resonance based magnetometer (MRM). The device consist of an organic diode structure, which is located above two mutually perpendicular striplines required for on-chip spin resonant excitation and field modulation. Electron and hole polarons are injected from opposite sides into the diode structure, and recombine spin-dependently in the organic semiconductor.

the current. At its core, the diode consists of a thin MEH-PPV layer sandwiched between an electron and a hole injecting contact. This structure is identical to organic semiconductor stacks used for conventional organic light emitting diodes [16]. In order to measure an externally applied magnetic field B_0, changes to a current flowing through the diode structure are monitored by a lock-in amplifier whose reference frequency is provided by a low-frequency alternating current that is applied to a thin film stripline coil which is positioned underneath the diode. This lock-in detected current change is then measured as a function of the RF field applied to a second thin-film stripline which is positioned underneath the first stripline with a perpendicular orientation (the B_1 field). Once a frequency ν is identified at which the MR induced diode current change is maximized, finding $B_0 = \nu/\gamma$ is simple, with γ being the gyromagnetic ratio of the charge carrier species that is in resonance. The properties of this organic thin film MRM are explored with regard to its feasibility, its sensitivity and magnetic field-limitation as well as its response to temperature fluctuations and device degradation. In the following, the results of these studies are discussed. Unless otherwise stated, the experimental data were acquired at room temperature.

6.2 Results

6.2.1 Resonant current change mechanism

First the assumption that electrically detected spin-resonance signals are independent of spin polarization over large magnetic field ranges are scrutinized, a crucial prerequisite for the feasibility of the MRM. For polaron-pair (PP) recombination, spin-dependent rates are based on the spin permutation symmetry of charge carrier pairs, not on spin polarization [18, 19], and therefore only a weak B_0-dependence of the signal current is expected. While this model has been scrutinized extensively in recent years with EDMR and ODMR spectroscopy [16, 20, 21], these studies were all been performed at X-Band ($B_0 \approx 340$mT) [22] or frequencies in the same order of magnitude [23]. Fig. 6.2 a)-b) shows measurements of a direct current flowing through the diode structure as a function of B_0 while an RF-field with constant frequency and amplitude is applied.

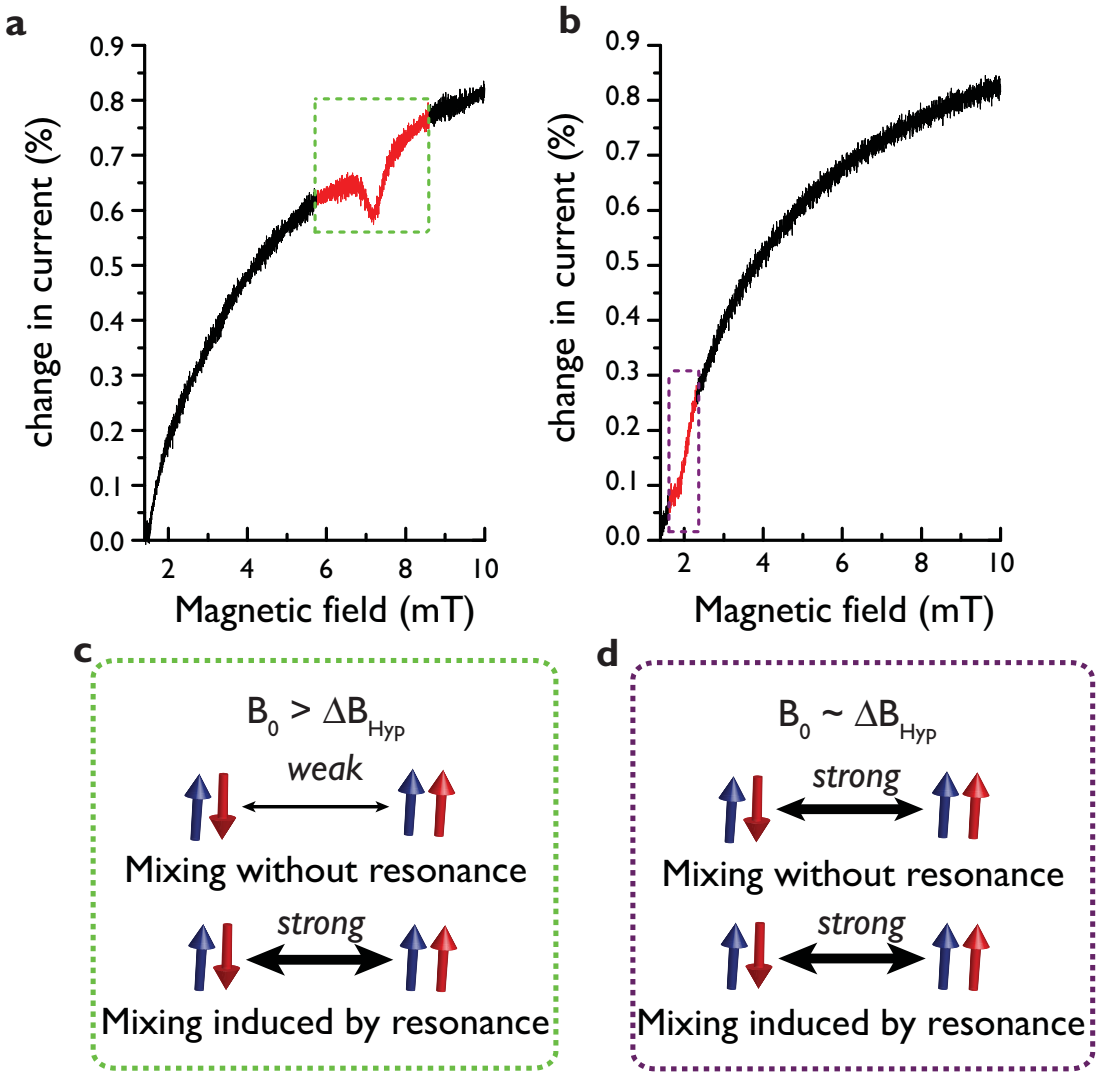

Figure 6.2. (a) - (b) The magnetic field response of a DC current (no modulation) in a bipolar MEH-PPV diode as a function of magnetic field as RF radiation (200 MHz, in (a) ; 50 MHz, in (b)) is applied. Reductions in the current are seen when MR conditions are satisfied. These are more pronounced when the applied field $B_0 > B_{Hyp}$ where MR-induced spin mixing dominates. (c) - (d) Schematic illustration of the origin of resistance changes due to spin mixing induced by the local hyperfine fields (B_{Hyp}) and due to MR excitation. All measurements were performed at room temperature.

The left plot displays the relative current change $\Delta I/I$ in the presence of RF radiation ($\nu = 200$MHz) as a function of the magnetic field for 1.3mT $< B_0 <$ 10mT. Throughout the measured range, the plot shows a monotonic increase of the sample current, a behavior which is due to the strong magnetoresistance. In addition to the monotonic magnetic dependence of the current, the plot shows a reduction of the sample current around $B_0 \approx 7.14$mT, corresponding to the magnetic resonance condition of $g \approx 2.0026(4)$ with a ($\Delta I/I \approx 10^{-3}$) decrease of the device current, similar in magnitude to previous X-Band EDMR measurements [16, 22].This current change is due to a change of the charge carrier ensembles' spin dynamics from a steady state to a spin-resonantly excited state. When spins of charge carriers are manipulated, the ratio of singlet to triplet pairs changes, and as a result, recombination and dissociation rates, and thus, the current change [16]. This behavior was confirmed at a large number of B_0 values between 2mT and 340mT (see Fig. 6.3).

A strong reduction of this signal below $B_0 \approx 2$mT was observed with a detection limit (for a DC measurement with bandwidth $\approx$ 10kHz) at about $B_0 \approx 1$mT. Fig. 6.2 b), right panel shows the repetition of the measurement illustrated in the left panel for an RF field of $\nu = 50$MHz. Again, a MR induced change of the current is visible at $g \approx 2.002$, ($B_0 \approx 1.79$mT) but with diminished amplitude. This lower B_0 measurement limit is attributed to reduced MR induced spin mixing rate changes: as long as the external magnetic field exceeds the local hyperfine field of the -conjugated polymer ($B_0 > B_{Hyp}$), spin mixing is drastically suppressed and longitudinal spin relaxation rates T_1 are long [25, 26]. The applied MR can then increase spin-mixing artificially (as depicted schematically below the spectra [7], and, therefore, substantially modify the current. In contrast, when $B_0 < B_{Hyp}$, spin mixing is fast with and without the presence of MR. Thus, MR changes the spin mixing, and therefore the spin-dependent current, only marginally, and as a consequence the EDMR signal disappears.

The disappearance of the MR signal when $B_0 \approx B_{Hyp}$ provides confirmation that the PP (electron-hole) mechanism illustrated in Fig. 6.2 a) is responsible for both the EDMR signal as well as for the DC magnetoresistance. This assignment has previously been a subject of debate [7, 25, 27–29]. It is crucial to note that for

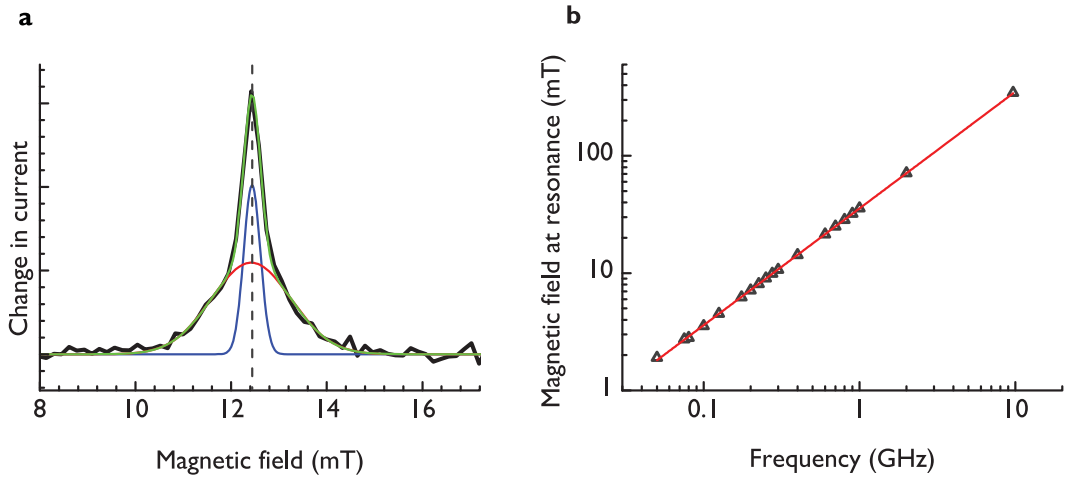

Figure 6.3. Calibration of the MR magnetometer. (a) Resonance spectrum for 350MHz radiation, measured using pulsed resonant excitation. Note that the current change after the excitation pulse was detectable for approximately 1ms undergoing a quenching/enhancement transient that is known for spin-dependent pair processes [24]. The data presented here were measured 20μs after the pulse excitation to maximize s/n. The spin resonance used for the MRM device is the narrow (blue) component of the spectrum. The (red) component represents the wide peak, and the (green) curve is the fit using (red) and (blue) in sum. (b) Plot of the peak magnetic field where maximal MR-induced current change is measured as a function of the applied excitation frequency, following a linear relationship (note that the error of the data points is below the size of the symbols). A linear fit of the above data yields a gyromagnetic ratio $\gamma = 28.03(4)$ GHz T^{-1} and a corresponding g-factor $g = 2.0026(4)$. Thus, the electrically detectable electron gyromagnetic ratio can be used as an absolute magnetic-field standard.

MR-based magnetometry, this effect does not set a lower limit on magnetic field measurements: when $B_0 < B_{Hyp}$, a magnetic field $B_{det} = B_0 + B_{off} > B_{Hyp}$ can be determined by application of a well-defined DC magnetic offset field Boff via a direct current in the modulation stripline. B_0 is then obtained from $B_{det} - B_{off}$.

6.2.2 Field sensing: precision and stability

Most important for the absolute determination of the magnetic field experienced by the MRM device is the measurement standard, which in this case is the gyromagnetic ratio γ (or Landé g-factor) of the polaron spin. The set of EDMR measurements conducted the thin-film samples over a large magnetic field range can be used in order to accurately determine γ and to confirm the independence of γ from the magnetic field itself. Experimentally, the B_0-dependence for single pulse transient experiments was measured. One fitted spectrum for $\nu = 350$MHz is shown as an example in Fig. 6.3 a). As expected for the EDMR spectrum of the PP process, the signal shows two Gaussian peaks corresponding to the two charge carrier species [16, 20]. In order to maximize the accuracy of the B_0 measurement, one should choose the narrow Gaussian peak for the MRM, which is attributed to one charge carrier species (electron or hole). Fig. 6.3 b) displays a plot of the magnetic field values for which the maximal current change was observed as a function of the applied RF field. The data is fit by a linear function revealing a value of $\gamma = 28.03(4)$ GHz T^{-1}. The slight difference between this value and the free electron gyromagnetic ratio (28.025 GHz T^{-1}) arises due to the weak but non-negligible spin-orbit coupling of the charge carrier spin states [21, 30]. Fig. 6.3 b) demonstrates the reproducibility of this value over nearly three orders of magnitude in MR frequency (40MHz - 9.7GHz). The limitation of this experiment to less than $\approx$ 340mT ($\approx$ 9.7GHz) is of purely technical nature. To determine the operational range of the sensor, the stability of the gyromagnetic ratio in the devices was explored as a function of temperature and device degradation. This was accomplished by (i) reproducing γ at a collection of temperatures ranging from 5K to room temperature, and (ii) repeating the experiment after device degradation. The results of these experiments are summarized in Fig. 6.4 a) which shows the

gyromagnetic ratios obtained under the different conditions. Note that the error bars displayed for each of the data points represent the standard deviation estimated from the fit of the EDMR spectra belonging to the individual measurements. The true errors are expected to be much lower than these fit estimates since the variation of the data throughout the measurement range is much smaller. To test this hypothesis, the temperature average value ($\gamma = 28.03$ GHz T^{-1} represented by the red line) was compared with its standard deviation obtained from the entire set of measurements ($\sigma_\gamma = 0.01$ represented by the grey bar about the red line). This comparison shows (i) that the real error of the individual measurements is about 10MHz/T and (ii) that within this error, the magnetic field measurement is independent of temperature over almost two orders of magnitude, and finally (iii) that γ is confirmed when compared to the fit in Fig. 6.3. Even with encapsulation, devices made with organic semiconductors can degrade over time, leading to fluctuations in device conductivity. The effect of this degradation was simulated by exposure of the diodes to ambient atmosphere for 24 hours [31], without using any protective measures, to investigate the impact of degradation on the MR approach described above. The comparison of the current voltage characteristics of the degraded and the pristine sample is shown in Fig. 6.4b).

The data exhibit a strong reduction in device conductivity upon degradation, which impacts on DC magnetoresistance. In contrast to this significant device modification, the resonant current change occurs under the same gyromagnetic ratio after degradation, within the error determined from the pristine sample. The measurements of γ were repeated on different thin film samples made with a variety of different contact materials (with a range of work functions) as well as with different spin cast parameters. The results of these measurements indicate that while the gyromagnetic ratio of the two resonance lines can change, depending on these parameters, the temperature- and degradation independence for any given sample is reproduced for the narrow resonance line. There is also no line shape or g-factor dependence of the narrow resonance line on the applied bias voltage, which further corroborates the robustness of this magnetic field standard.

Next the sensitivity limitations of the organic MRM were investigated. Using

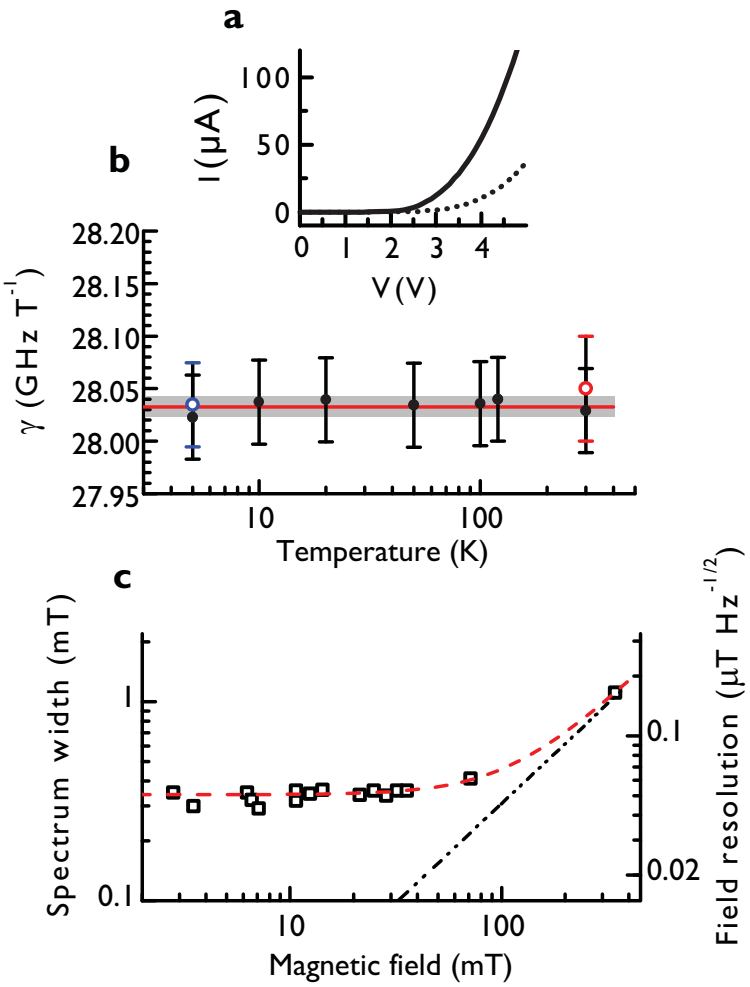

Figure 6.4. Robustness and sensitivity limits of the magnetometer device. (a) An example of the current-voltage characteristics of a device at 5K before (solid line) and after (dashed line) intentional degradation in air shows a drastic change of the device in spite of the unchanged MR behavior. (b)The gyromagnetic ratio,γ, measured as a function of temperature and degradation. The closed points drive from pristine devices, and the open circles (with colored error bars) from two of these devices after degradation. The error bars are upper estimates obtained from the fits of the individual spectra. The grey bar represents the standard deviation obtained from all data points. The red solid line gives the temperature average of all data. Within this range, neither the change in temperature nor degradation of the materials impact the reproducibility of the gyromagnetic ratio. (c) Plot of the MR peak width (left axis) as well as the resulting field resolution as a function of the externally applied magnetic field. The data illustrate how hyperfine fields dominate the resonance widths at low magnetic fields while spin-orbit contributions (which cause g-factor inhomogeneities) dominate at high magnetic fields. Right axis: Spectral sensitivity of the magnetic field measurements as a function of applied magnetic field.

field-modulated lock-in detection, the lower limit of the distinguishable field strength, or the minimum resolved external field [8] δB_{min}, depends on the spectral line width, the electrical shot noise [32] and the modulation amplitude of the driving field in the following form: $\delta B_{min} = \frac{\Delta I_{noise}}{B_m \frac{\delta^2 I}{\delta B^2}}$, where $\Delta I_{noise} = \sqrt{2eI\Delta f}$, and B_m is the amplitude of modulation. The second derivative of the magnetic field-dependent current, as given in the denominator of this term, represents the "sharpness" of the resonance used, i.e. the slope (the first derivative) of the lock-in-detected spectrum at the zero-crossing point. As this quantity is the second derivative of a Gaussian function for the hyperfine-field broadened MEH-PPV resonance [16], it is proportional to the line width as well.

The widths of the EDMR spectra, and thus the device sensitivity, are not always independent of an applied external magnetic field. EDMR lines can be broadened inhomogeneously (randomly, following a Gaussian) due to a distribution of spin-orbit interactions as well as hyperfine fields. Intersite variations in spin-orbit interaction lead to a distribution of the g-factor, and therefore a resonance line width proportional the applied B_0 field. In contrast, inhomogeneous broadening due to random hyperfine fields is independent of any external magnetic field as long as the nuclear spin ensemble remains unpolarized by the external field (at room temperature, significant thermal hydrogen nuclear polarization cannot be achieved with static magnetic fields < 100T). Thus, for the polaron resonance line used here, at low external magnetic fields one can expect the line widths to be limited by random hyperfine fields, and therefore to be constant. As spin-orbit induced line broadening exceeds the hyperfine fields, the linewidth should become proportional to the external magnetic field. Fig. 6.4 c), left ordinate (red line), displays the measured line width of the PP resonance as a function of B_0. When hyperfine fields and spin-orbit effects convolute, one can expect the Gaussian line width ΔB to be the geometric sum $\Delta B = \sqrt{(B_{Hyp})^2 + (\alpha B_0)^2}$ of the hyperfine field distribution width B_{Hyp} and the spin-orbit induced width of the gyromagntic ratio α multiplied by the applied external magnetic field B_0. The fit of the data in Fig. 6.4 c) with this relation reveals $B_{Hyp} \approx 0.35$mT (note that only the narrow polaron line was used here) while $\alpha \approx 2.9 \times 10^{-3}$ is given by the line

width obtained from a linear fit of the data at high fields where the spin-orbit term dominates. This is in excellent agreement with a previous estimate of the spin-orbit induced variations in g-factor based on X-band MR [29]. Given these parameters, one can now estimate the resolution limit for the MEH-PPV devices used in this study. For a modulation amplitude $B_m = \Delta B = 0.35$mT, a device current of $I_0 = 100\mu$A, and a MR-induced current change of I_A =100nA), one obtains a resolution of $\delta B_{min} \approx$ 50 nT Hz$^{-1/2}$ with a signal to noise of 1 within the hyperfine-limited magnetic field range ($<$ 100mT). The resolution for larger B_0 is given in Fig. 6.4 c), right ordinate (black line).

6.2.3 An integrated magnetic resonance-based organic magnetometer

The results described above confirm that the spin-dependent PP mechanism in MEH-PPV exhibits the resonance and stability properties that are needed for an organic MRM. With this given, one can demonstrate that all required components - the organic diode, microwave field modulation and a method for generating a resonant microwave frequency - can be integrated into a monolithic device, shown in Fig. 6.5 a). A diode, used to measure MR current changes, sits near two thin perpendicular strips of conducting materials which are electrically isolated from each other. One of the strips, the resonance stripline, is coupled to a high frequency source (low MHz to GHz range) that is used to generate the oscillating magnetic field required for spin resonance. A current is applied to the other strip to generate a magnetic field, either oscillating (to enable lock-in measurements) or static (for offsetting the resonance field), or both.

We have used this device to perform real magnetometry experiments. To determine the magnetic field B_0, a sweep of the frequency is carried out until the MR condition is found. Since it is difficult to implement a stripline with constant transmission properties over a very wide range of frequencies, one needs to use a magnetic field modulation lock-in scheme to filter the effects of the unwanted current changes that result from the coupling between the resonance strip and the device. During a measurement the MR excitation frequency is stepped on one line

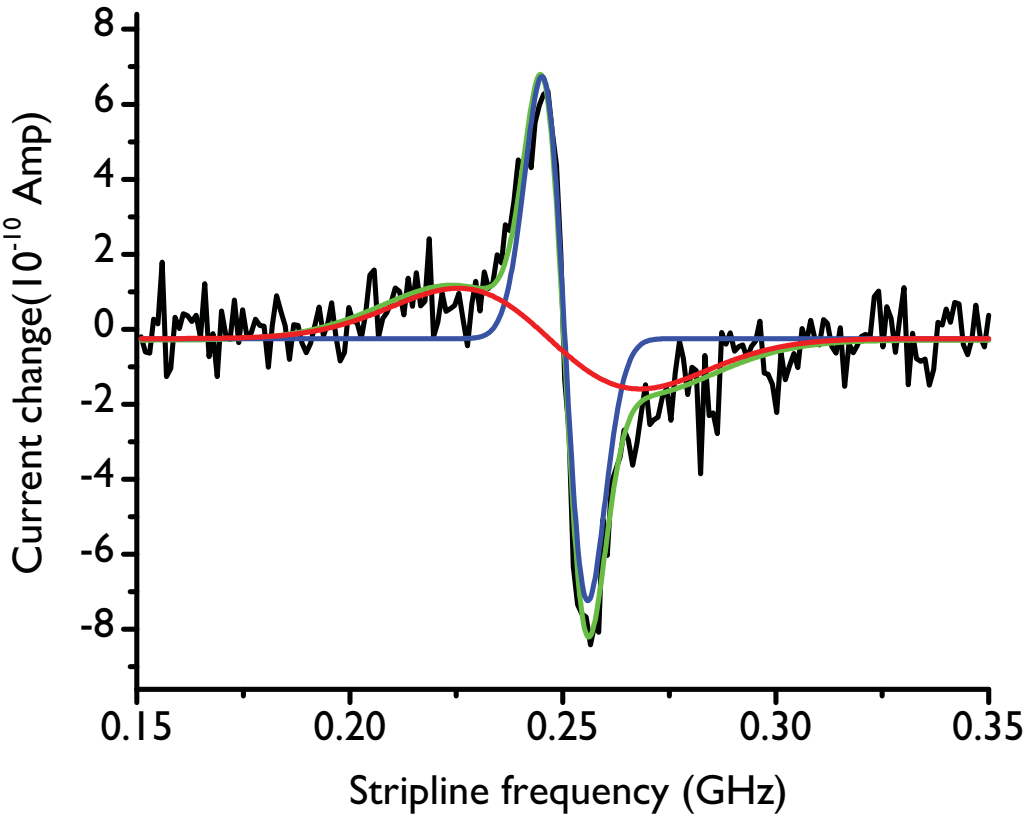

Figure 6.5. An integrated absolute magnetic field sensor. The magnetic field modulated current change in an integrated device as sketched in Fig. **??** a) as a function of stripline frequency in a static magnetic field of 8.93mT. A small modulation field of 0.05mT is applied to the static field at a frequency of 6kHz via the second stripline (labeled B_{mod}) to enable lock-in detection. The data shows the presence of two Gaussian resonances (red and blue curves), with the narrow resonance (blue fit) being significantly more pronounced in the lock-in detected derivative spectrum. Note that the presence of the broader of the two resonance lines (red) does not compromise the measurement since both resonances exhibit identical gyromagnetic ratios. The green curve is the sum of the respective Gaussians used in the fit, and shows an excellent fit.

whilst a low frequency (kilohertz) magnetic field modulation is applied to the other. Lock-in detection is then used to monitor changes in the device current. Fig. 6.5 b) shows the B_0-modulated device current change as the RF field is swept while the external magnetic field is held at a constant, arbitrary value. Since now, lock-in detection is employed, the derivative spectrum of the resonance line is seen. The zero crossing of the measured function is observed at 250.5(1)MHz, corresponding to a $B_0 = 8.93(2)$mT. From this data, a sensitivity spectral density of 6 μT Hz$^{-1/2}$ is determined. This agrees with the relation for δB_{min} given above, with $B_m \approx 0.05$mT and a bandwidth of $\Delta f \approx 10$Hz.

The position of the resonance, and thus the measured magnitude of the field, is independent of the orientation of the sensor. However, the amplitude of the resonant change in current for unknown fields oriented parallel to B_1 will be vanishingly small. This does not pose a limitation on the device, since it is possible to use either one of the perpendicular strips for driving spin resonance. Along with the magnitude, the direction of the measured magnetic field can also be determined by adding small offset fields and repeating the measurement - simple geometric analysis can then be used to determine the orientation of the magnetic field.

6.3 Discussion

An organic thin film calibration and offset-free, as well as temperature- and degradation-independent, MR-based magnetometer has been demonstrated. The feasibility of this sensor for magnetic fields B_0 is shown in a range 1mT $< B_0 <$ 340mT. These are not fundamental limitations, but more technical in nature. The upper limit was set by the limitation of the available microwave frequency equipment, whilst the lower limit could be overcome by a DC offset field added to the B_0 modulation. The sensor has been integrated into a monolithic device capable of high precision sensing. Due to the all-thin-film design of the device, it is anticipated that a large number of sensors could be accommodated on a single (perhaps flexible) substrate for imaging spatially-varying magnetic fields [33] , with a spatial resolution of less than 100 nm [34]. A comparison of this organic MRM concept with existing magnetometer

devices (discussed in detail elsewhere [35]) shows that this implementation may fill the gap for intermediate field precision magnetometry on small length scales. The organic MRM is less sensitive than SQUIDs but more sensitive than Hall sensors. In contrast to SQUIDs which only work at cryogenic temperatures, and Hall sensors, whose calibration is very temperature-dependent, the organic MRM operates – calibration free – over large temperature ranges. Compared to conventional NMR-based MRMs which are bulky and have diminished sensitivity in the lower magnetic field range, the organic MRM can be very small and its sensitivity is independent of magnetic field over a wide range. Since NMR resonances are more narrow than the polaron resonance used for the organic MRM, NMR-based MRMs will provide higher sensitivity at high magnetic fields. Similarly, for very small magnetic fields, SQUIDs will continue to be the most sensitive magnetic field detectors. It shall be noted that MRMs using NV centers in diamond have a number of the advantages discussed here (such as good temperature stability and high spatial resolution) but unlike the OLED-based magnetometer, they cannot be accessed electrically. One challenge for the organic thin film MRM will be the measurement time. As for conventional NMR-based MRMs, finding the MR lines can require time consuming frequency sweeps. However, for the proposed device design, this drawback could potentially be overcome by a combination of the MRM operation of the device with the magnetoresistive behavior of the polymer layer. The magnetic fields could be measured at high bandwidth using the magnetoresistance effect, while the MRM is used periodically for recalibration. In essence, this organic hybrid magnetometer would combine the advantages of both sensor approaches; the speed of a magnetoresistive measurement with the temperature and degradation independent accuracy of an MRM. Significantly increased sensitivity could also be obtained by exploiting the long spin phase coherence found in these materials [36], to perform quantum-enhanced field sensing [9,24], although this would require more complex pulsed spin resonance excitation [24].

6.4 Methods

6.4.1 Device fabrication

The EDMR device is a diode [37] stack consisting of the following materials: an indium tin oxide layer of ≈ 200nm, a hole injection layer of poly(3,4-ethylenedioxythiophene) (PEDOT)(≈ 50 nm thick) that was applied using a spin-coater at ≈ 3000rpm, followed by a thin layer ≈ 200nm of poly[2-methoxy-5-(2'-ethyl-hexyloxy)-1,4-phenylene-vinylene] (MEH-PPV) with density ≈ 7.5g/l that was also applied via spin coating at ≈ 1600rpm in a nitrogen glove box, with a ≈ 25nm calcium contact for good electron injection, followed by an Al layer (≈ 50nm thick). Devices were fabricated on Corning glass substrates. The temperature dependent γ data were taken with devices with either Sr or Ca electrical top-contacts in order to verify the contact material independence of the observed spectra. The Al, Ca, and Sr contacts were thermally evaporated in a nitrogen glove box at a pressure of $\approx 10^{-6}$ mbar.

6.4.2 Experimental setup

For the measurements in Fig. 6.2 the device was operated in forward bias with a SRS SIM928 isolated voltage source, and placed inside a small coil. The coil was connected to a tunable frequency source for the application of a fixed frequency. The device output current was then connected to an SRS SR570 low-noise current amplifier set to operate as a low-pass filter (10Hz cutoff). The output then connected to a 16-bit fast digitizer card for acquisition. For the single pulse experiments included in Fig. 6.3, a single stripline resonator design was used while the diode was operated in forward bias mode. The output current was then connected to a SRS SR570 low-noise current amplifier in high band-width mode with an offset current close to I_0. This output was then connected to an 8-bit transient recorder. For the data in Fig. 6.5 b), the device was operated in forward bias while situated near two electrically separated stripline resonators (as described in Fig. 6.5 a)) for the application of the driving and modulation fields, respectively. A reference frequency of ≈ 6kHz was fed to the modulation stripline by a SRS DS345 function generator at ≈ 5Vpp thus providing ≈ 0.02mT of modulation field amplitude. The in-phase output was then connected to a 16-bit fast digitizer card for data acquisition. For more details regarding the low-field

setup and resonator characterization, please see Appendix A.

6.4.3 Sensitivity analysis

The sensitivity (also called resolution) δB_{min} of an individual magnetic field measurement corresponds to the error (the standard deviation) of a single measurement. Its unit is equal to the unit of the observed quantity, the magnetic field. If conducting a measurement with sensitivity δB_{min} takes a time τ, then the sensitivity of the setup can be improved to a sensitivity $\delta B_{min}/\sqrt{n}$ simply by conducting n measurements in a time $n\tau$ followed by averaging of the n measured values. The sensitivity of a magnetometer is therefore dependent on the measurement time and it is more meaningful to describe the device in terms of its sensitivity spectral density (which, rather confusingly, is often also referred to as 'sensitivity' in the literature). The sensitivity spectral density is a magnetic field times the square-root of time, its unit is $[T\sqrt{sec}] = [T/\sqrt{Hz}]$. The resolution in measurable field can be affected by the electrical shot noise, the amplitude of the applied modulation field B_m and the width of the resonance line ΔB through the following relation: $\delta B_{min} B_m \frac{\delta^2 I}{\delta B^2} = I_{noise}$, where $I_{noise} = \sqrt{2e\Delta f I_0}$ is the shot noise.$\frac{\delta^2 I}{\delta B^2}$ is the second derivative of the magnetic field dependence of the device current I(B_0) which for the case of MEH-PPV is a Gaussian function $I(B_0) = \frac{I_a B_m}{\Delta B\sqrt{2\pi}} e^{\frac{(B_0 - B_{res})^2}{2(\Delta B)^2}}$ with I_a being the spin-dependent on-resonance signal current through the device.Δf is the bandwidth of the measured signal and is defined by the low-pass filter of the lock-in detector. At the center of the Gaussian distribution ($B_0 = B_{res}$), $\frac{\delta^2 I}{\delta B^2}(B_0) = \frac{I_a B_m}{2}\sqrt{\frac{2}{\pi}}\frac{1}{\Delta B^3}$. Thus, the sensitivity spectral density is $\frac{\delta B_{min}}{\sqrt{\Delta f}} = 2\frac{\sqrt{\pi e I_0}}{I_a}\Delta B$, where it is assumed that the modulation amplitude B_m is set equal to the line width ΔB. For the resolution estimation in the given devices, experimental values of $I_a = 100$nA, $I_0 = 100\mu$A, and ΔB = 0.35mT as obtained from the fits in Fig. 6.4c) were used.

6.5 References

[1] M. Hmlinen, M, R. Hari, R. J. Ilmoniemi, J. Knuutila, and O. V. Lounasmaa, Rev. Mod. Phys. **65**, 413 (1993).

[2] J.-B. Mathieu, S. Martel, L. Yahia, G. Soulez, and G. Beaudoin, Mri systems as a mean of propulsion for a microdevice in blood vessels, in *Engineering in Medicine and Biology Society, 2003. Proceedings of the 25th Annual International Conference of the IEEE DOI - 10.1109/IEMBS.2003.1280880*, volume 4, pages 3419–3422 Vol.4, 2003.

[3] M. Adamo, C. Bonavolont, M. Valentino, and E. Sarnelli, Investigation of artificial cracks by scanning squid magnetic microscope, 2009.

[4] S. J. Bending, Advances in Physics **48**, 449 (1999).

[5] I. M. Savukov, S. J. Seltzer, M. V. Romalis, and K. L. Sauer, Phys. Rev. Lett. **95**, 063004 (2005).

[6] I. K. Kominis, T. W. Kornack, J. C. Allred, and M. V. Romalis, Nature **422**, 596 (2003).

[7] T. D. Nguyen, B. R. Gautam, E. Ehrenfreund, and Z. V. Vardeny, Phys. Rev. Lett. **105**, 166804 (2010).

[8] A. Jander and P. Dhagat, Solid-State Electronics **54**, 1479 (2010).

[9] J. M. Taylor et al., Nat Phys **4**, 810 (2008).

[10] A. Honig, Review of Scientific Instruments **49**, 183 (1978).

[11] I. Solomon, D. Biegelsen, and J. Knights, Solid State Communications **22**, 505 (1977).

[12] D. R. McCamey et al., Appl. Phys. Lett. **89**, 182115 (2006).

[13] M. V. G. D. Nusran N.M., Ummal Momeen M., Nat Nano **7**, 109 (2012).

[14] W. G. et al., Nat Nano **7**, 105 (2012).

[15] R. H. Friend et al., Nature **397**, 121 (1999).

[16] D. R. McCamey et al., Phys. Rev. Lett. **104**, 017601 (2010).

[17] J. M. Lupton, D. R. McCamey, and C. Boehme, ChemPhysChem **11**, 3040 (2010).

[18] E. Frankevich et al., Phys. Rev. B **62**, 2505 (2000).

[19] E. L. Frankevich et al., Phys. Rev. B **46**, 9320 (1992).

[20] S.-Y. Lee et al., J. Am. Chem. Soc. **133**, 2019 (2011).

[21] G. Silva, L. Santos, R. Faria, and C. Graeff, Physica B: Condensed Matter **308-310**, 1078 (2001).

[22] W. J. Baker, D. R. McCamey, K. J. van Schooten, J. M. Lupton, and C. Boehme, Phys. Rev. B **84**, 165205 (2011).

[23] P. A. Lane, X. Wei, and Z. V. Vardeny, Phys. Rev. B **56**, 4626 (1997).

[24] J. R. Maze et al., Nature **455**, 644 (2008).

[25] T. D. Nguyen et al., Nat Mater **9**, 345 (2010).

[26] S. P. Kersten, A. J. Schellekens, B. Koopmans, and P. A. Bobbert, Phys. Rev. Lett. **106**, 197402 (2011).

[27] P. A. Bobbert, W. Wagemans, F. W. A. van Oost, B. Koopmans, and M. Wohlgenannt, Phys. Rev. Lett. **102**, 156604 (2009).

[28] P. A. Bobbert, T. D. Nguyen, F. W. A. van Oost, B. Koopmans, and M. Wohlgenannt, Phys. Rev. Lett. **99**, 216801 (2007).

[29] J. M. Lupton and C. Boehme, Nat Mater **7**, 598 (2008).

[30] Z. G. Yu, Phys. Rev. B **85**, 115201 (2012).

[31] S. Gardonio et al., Organic Electronics **8**, 37 (2007).

[32] N. Stemeroff and R. de Sousa, Phys. Rev. Lett. **107**, 197602 (2011).

[33] L. M. Pham et al., New Journal of Physics **13**, 045021 (2011).

[34] H. Yamamoto et al., Nano Lett. **5**, 2485 (2005).

[35] J. Lenz, Proceedings of the IEEE DOI - 10.1109/5.56910 **78**, 973 (1990).

[36] *Baker, W.J. et al. Slow hopping and spin-dephasing of coulombically-bound polaron pairs in an organic semiconductor at room temperature, to be published in Phys. Rev. Lett. (2012).*

[37] D. R. McCamey et al., Nat Mater **7**, 723 (2008).

CHAPTER 7

SUMMARY AND OUTLOOK

The work presented in this dissertation has confirmed the previously discussed polaron pair recombination qualitatively and quantitatively. The control of recombination rates with spin–resonantly induced coherent spin motion revealed unambiguously that the observed recombination path is due to a system consisting of two weakly spin–coupled paramagnetic centers with $s = 1/2$. The properties of the PPs in MEH-PPV have been investigate and the results include longitudinal and transverse relaxation times, polaron hopping times, intra pair coupling strengths and hyperfine interactions. In addition to the exploration of the PP process, another, qualitatively different spin–dependent process was observed and confirmed, the previously proposed triplet-exciton polaron recombination process which was observed in electron rich devices at temperatures below 100K. The fundamental insights gained in the course of this work will help to further corroborate the microscopic physics of organic semiconductors. In addition, the unexpectedly long coherence times of polaron pair spins could potentially lead to the implementation of polaron qubits, the application of polarons for quantum storage and quantum information technologies. The ability of spin-state manipulation in MEH-PPV to control charge propagation has also been demonstrated to be utilizable for an organic electronics based magnetic resonance magnetometry (OMRM). OMRMs are organic spintronic sensors whose performance is accurate without calibration on wide temperature ranges and even when strong materials degradation occurs.

There are still many open question about the nature of spin–dependent processes in organic semiconductors. The experiments in chapter 5 were motivated by the question of ballistic spin–diffusion in MEH-PPV. In spite of very long transverse

relaxation times which have been mesured, it is still not clear why a Hanle effect can not be observed in organic spin valves, even on very short diffusion paths (a few nanometers). Also, with the insights gained on the nature of hyperfine interaction in Chapters 5 and 6, the question of whether hyperfine interaction can be utilized for technical applications such nuclear spin memory is open. Future experiments involving electrically detected ESR and nuclear magnetic resonance, so called electron-nuclear double resonance experiments (ENDOR) are conceivable. Similarly, magnetic resonance spectroscopy at very low fields which has been pioneered in this dissertation is could conceivably lead to a range of new and exciting insights. Finally, the experimentally verified triplet-exciton polaron recombination process should be further investigated on a more quantitative level. Transition times, spin relaxation times, spin-interactions within pairs of polarons and triplet excitons are still elusive.

7.1 List of publications

Pulsed electrically detected magnetic resonance in organic semiconductors

C. Boehme, D.R. McCamey, K.J. van Schooten, W.J. Baker, S-Y. Lee, S-Y. Paik, J.M. Lupton,

Phys. Stat. Sol. (b) 246 (11-12), 2750-275 (2009).

Hyperfine-field-mediated spin beating in electrostatically bound charge carrier pairs

D.R. McCamey, K.J. van Schooten, W.J. Baker, S-Y. Lee, S-Y. Paik, J.M. Lupton, C. Boehme,

Phys. Rev. Lett. 104, 17601 (2010).

T_1 and T_2 spin relaxation time limitations of phosphorous donor electrons near crystalline silicon to silicon dioxide interface defects

S-Y. Paik, S-Y. Lee, W.J. Baker, D.R. McCamey, C. Boehme,

Physical Review B 81, 075214 (2010).

Differentiation between polaron-pair and triplet-exciton polaron spin-dependent transport mechanisms in organic light-emitting diodes by coherent spin beating

W.J. Baker, D.R. Mccamey, K.J. van Shooten, J.M. Lupton, C. Boehme,

Physical Review B 84, 165205, (2011).

Robust absolute magnetometry with organic thin-film devices

W.J. Baker, K. Ambal, D. P. Waters, R. Baarda, H. Morishita, K. van Schooten, D.R. McCamey, J. M. Lupton and C. Boehme,

Nature Commun. 3, 898, doi:10.1038/ncomms1895 (2012).

Slow hopping of coherently coupled polaron pairs in an organic semiconductor at room temperature

W.J. Baker,T.L. Keevers, D.R. McCamey, J.M. Lupton, C. Boehme,

Phys. Rev. Lett. 108, 267601(2012).

7.2 Pending manuscripts

Spin-dependent exciton quenching and intrinsic spin coherence in CdSe/CdS nanocrystals

K. J. van Schooten, J. Huang, W. J. Baker, D. V. Talapin, C. Boehme, and J. M. Lupton,

submitted for publication.

Effect of dipolar coupling on coherently controlled spin-dependent transition rates

M. E. Limes,J. Wang, W. J. Baker, S.-Y. Lee, B. Saam, and C. Boehme,

in preparation.

Effect of injection materials on spin-orbit coupling in MEH-PPV thin film devices.

W. J. Baker, K.J. van Shooten, J. M. Lupton, and C. Boehme,

in preparation.

APPENDIX

LOW-FIELD METHODS

A.1 Setup for CW magnetoresistance measurements

To determine whether a organic device has a monotomic DC response or magnetoresistance effect to an external magnetic field change, the setup shown in Fig. A.1 was created. With this configuration the DC current response can be measured while an external RF signal is applied to test for a resonant response in the magnetoresistance. A sample is placed in either the all-coil or all-stripline resonator (described below) where a constant voltage to the device can be applied from an SRS SIM928

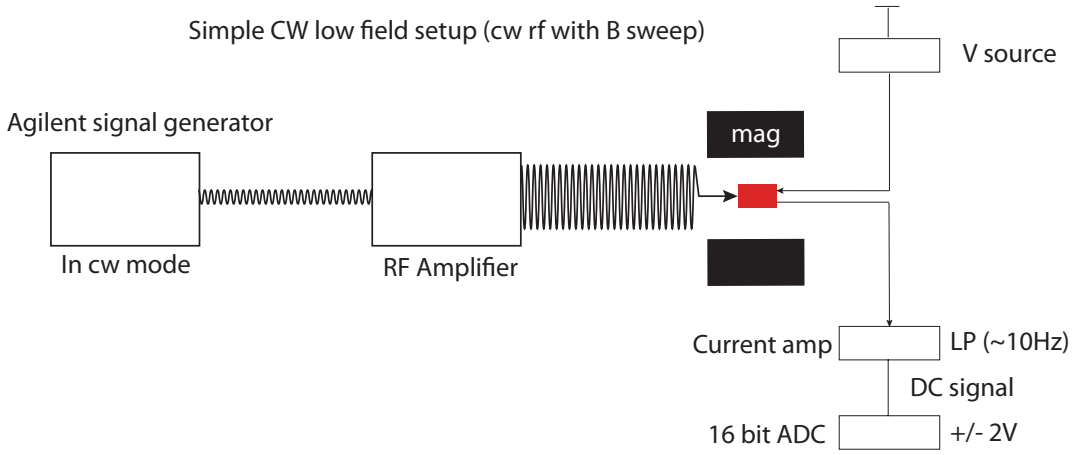

Figure A.1. The setup used in the magnetoresistance measurements in this chapter (Fig. **??**). The signal generator is set to a single frequency and the external magnetic field is then rapidly swept (t $\approx$ 30 sec) through the resonant field value. The current amplifier is also used as a low pass filter. The 16 bit ADC (analog to digital converter) is used for its high dynamic range.

isolated constant voltage source, while a RF signal can be applied to the sample from an external RF signal generator. The external magnetic field was swept by the Bruker's field controller and the detection was carried out by the Bruker's built-in 16-bit ADC. Before the signal is sent to the ADC it is first amplified by a low-noise SRS 570 current amplifier where a low pass filter ($\approx$ 10Hz) is used to obtain only the DC current.

A.2 Setup for low field pEDMR

To test the response in the device current after a short pulse of RF from an external signal generator, the configuration in Fig. A.2 was used.

In order to synchronize the RF pulse and signal acquisition, the Bruker's PatternJet and 8-bit ADC with signal averaging was used in conjunction with the PulseSpell programming language. The signal generator was gated by the PatternJet by connecting the [+x] phase pulse output to the trigger input of the signal generator. Before this can work, the signal generator must be set to pulse mode and external

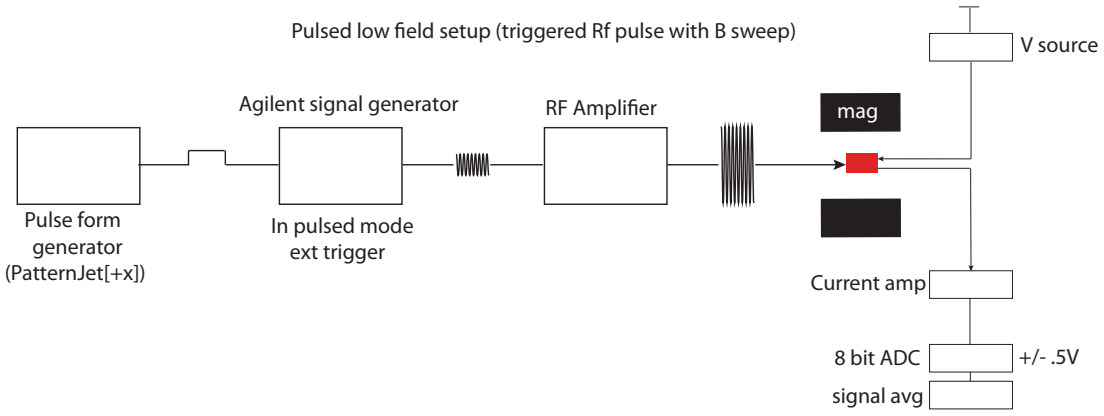

Figure A.2. The low-field pulsed EDMR setup. An external signal generator is gated by the Bruker's PatternJet pulse former. The pulse is then sent to an amplifier then into the sample space. All else is same as a standard pEDMR experiment.

trigger mode. This signal is then passed through an RF amplifier to increase the power then finally connected to the RF signal input in either low-field resonator (described below). The output from the device was then connected to an SRS current amplifier where a band pass (high band width mode) filter was set, making sure the filter settings did not cut off relevant frequencies. Finally, the signal was acquired and averaged by the Bruker's SpecJet transient recorder where an 8-bit ADC was used and any number of averages can be taken to achieve the right signal to noise ratio. Any pulse program that you can create in the PulseSpell programming language, can be implemented with this setup, for instance a Rabi-nutation or Hahn-echo scheme.

A.3 Lock in detected frequency sweep: magnetic field sensor

In order to determine the magnitude of an external magnetic field, a separate experiment must be used in which the frequency of the source is swept while monitoring the current response of the device. This can be done with or without a phase sensitive detection scheme, however phase sensitive detection is better due to the differing impedance matching cases as the frequency is swept. Below in Fig. A.3 is a depiction of the setup used to determine an unknown magnetic field with the spin-dependent current change in an OLED using lock-in detection.

The idea is that the frequency of the RF signal is swept while the unknown external magnetic field is modulated at a lower frequency reference signal in which to carry out lock-in or phase sensitive detection on the current response. An example is shown in Fig. A.4. To do this the signal generator is set frequency-sweep mode to carry out a frequency sweep. Every time a new frequency is set a trigger signal is sent to the ADC to acquire. Each new acquisition at a given frequency was measured for 5 seconds by the ADC, where the sweep time was set to 6 seconds. This is the basis for synchronization. In order to have good overlap of signal acquisition set the trigger delay or sweep time in the signal generator to be greater than the acquisition time of the ADC. In order to only see changes in current do to the resonant changes and not impedance mismatching, an external lock-in was used in which a 6 kHz signal was sent to a set of modulation coils or a small stripline oriented perpendicular to

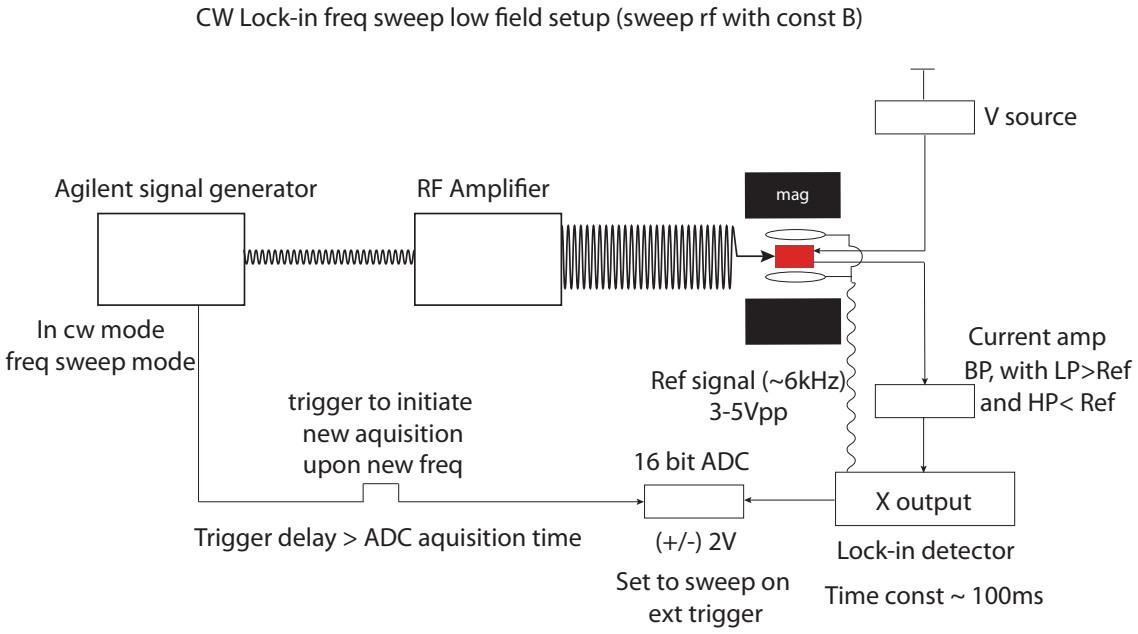

Figure A.3. The magnetic field sensor configuration. The signal generator is set to frequency sweep mode and will out put a CW signal for some dwell time. Each new detection is triggered by a signal from the signal generator and is sent to the ADC. The external magnetic field is kept at a constant value while being modulated by a set of small coils or a small stripline with the reference frequency coming from either the external lock-in detector or a function generator. The signal is sent through a current amplifier where a band pass around the reference frequency is set. The X-output from the lock-in is then sent to the 16-bit ADC for acquisition.

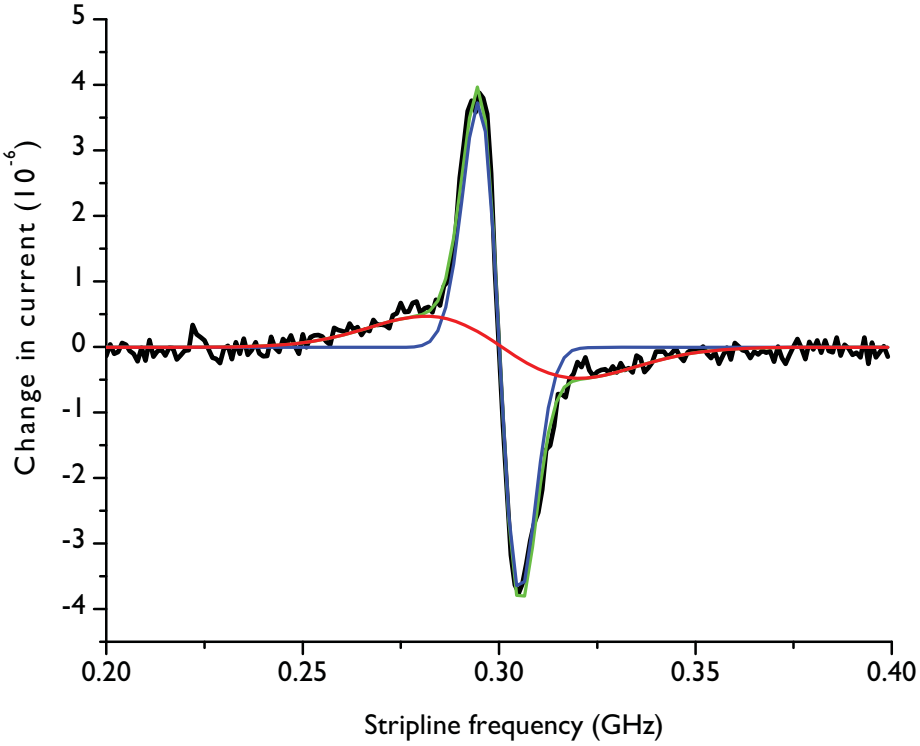

Figure A.4. An example of frequency sweep experiment carried out with the all-coil configuration shown in Fig. A.5 and the lock-in detection setup shown in Fig. A.3. When compared to the similar sweep done with the stripline setup, the effect of the greater B_{mod} from the Helmholtz coils versus the small stripline is seen, with a dramatic increase in the signal to noise. However, this is at a cost of space. The all-stripline or monolithic configuration could be repeated and packed into a small volume for a pixelated type magnetic field sensor design, for instance, on a cell-phone screen.

the driving field from the signal generator. The current output from the device was passed through a current amplifier where a gain was set and a bandpass filter was also employed which was set around the reference frequency, then into the lock-in detector where an additional sensitivity setting was used and an appropriate time const was used to set the low pass filter (τ = 100ms). In order to have the ADC respond to the signal generator's trigger, the ADC must be set to ext sweep mode.To determine the magnetic field strength B_1 that can be delivered by the given coil configuration shown in Fig. A.5, a simple Rabi-nutation experiment was carried out at different powers where the transient response in device current is integrated as a function of the RF pulse length. The experimental configuration used is shown in Fig. A.2. The results are shown in Fig. A.6. At full power (0db), a 10mW signal from the signal generator is amplified by a 100W amplifier with a 50db gain in signal. With this 0db setting a π rotation in one spin in a polaron pair is obtained in approximately 108ns which corresponds to a B_1 of around 2G. From the data shown in Chapter 6 Fig. 6.3 it is obvious that the main stripline can supply a large enough driving field in which to effect the mutual spin orientation of recombining spin pairs in the OLED device that sits above. However, to gain a better understanding of the actual field strength possible from the microstripline we must carry out either a Rabi-nutation experiment or confirm the strength with an external Hall probe magnetometer. Since there are two striplines in the magnetometer structure shown in Fig. A.7 we need to characterize them both. For the larger stripline a Rabi-nutation experiment was carried out and the results of which are shown in Fig. A.8. The source of the field is the RF driven surface currents on the surface of the metallic stripline which is connected to a RF source via a SMA and RF amplifier(used the same amplifier as previous low-field measurements). The OLED is placed in proximity to the stripline surface in which to maximize the field strength and homogeneity. From the results in the figure we can place an approximate maximum field strength from the period of the Rabi-nutation signal. The signal has all the signs of the PP signal, so the expected particle under rotation is a spin-1/2 electron or hole undergoing recombination. From the π rotation point in the nutation we can approximate a field strength of $\sim$1G at

0db. The smaller stripline in the structure,labeled B_{mod} in Fig. A.7 the field strength is much smaller. This is due to the smaller allowed current from the electrical leads. For this measurement a Hall probe magnetometer was used, and a field of approximately 0.5G was found at a input current of I=10mA.

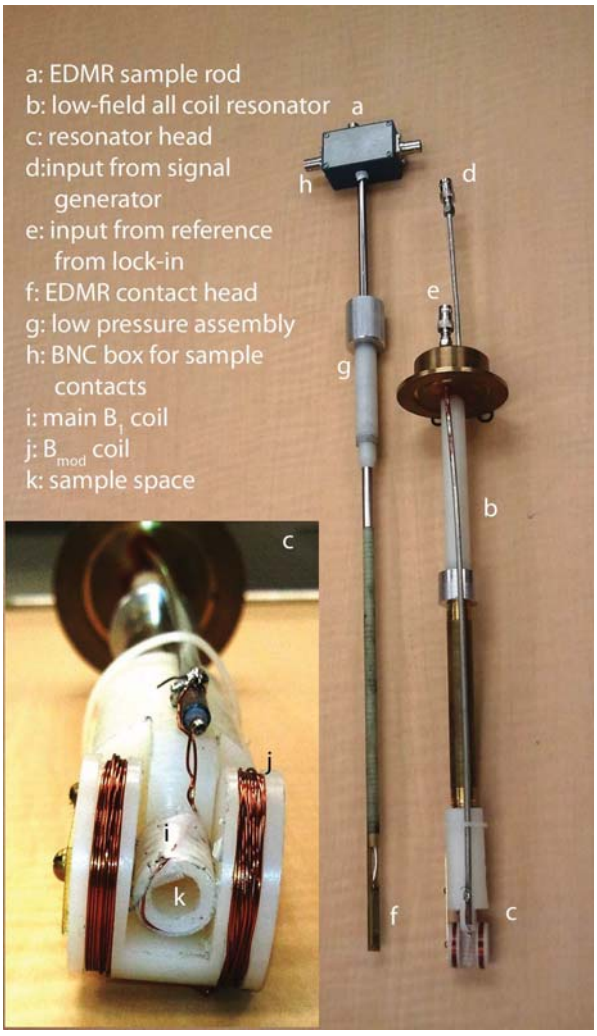

Figure A.5. A diagram explaining the components of the all-coil low field resonator. This was used for the magnetoresistance experiments and some of the single pulse experiments.

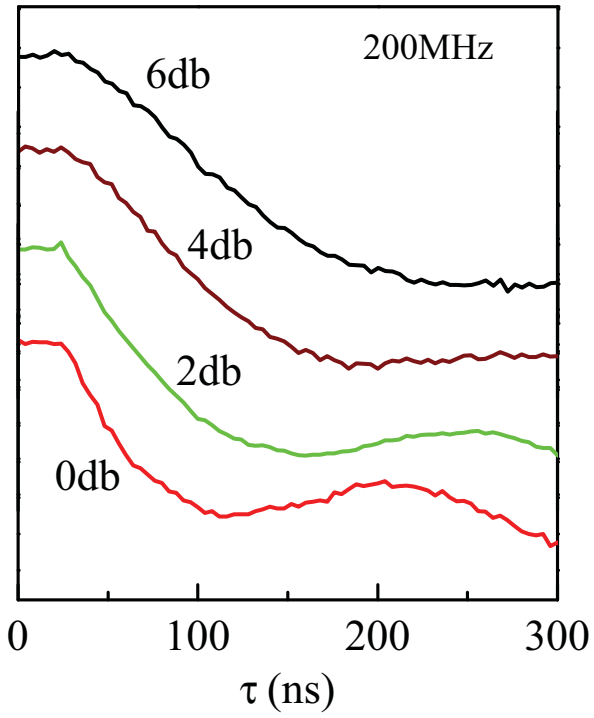

Figure A.6. A collection of Rabi-nutations using the configuration shown in Fig. A.5 and Fig. A.2 at different powers, showing a π rotation of 108 ns at 0db at 200MHz RF signal with an external field of $B_0 = 71.4G$. This corresponds to a driving field B_1 of 2G at 0db. The attenuation was carried out by the signal generator

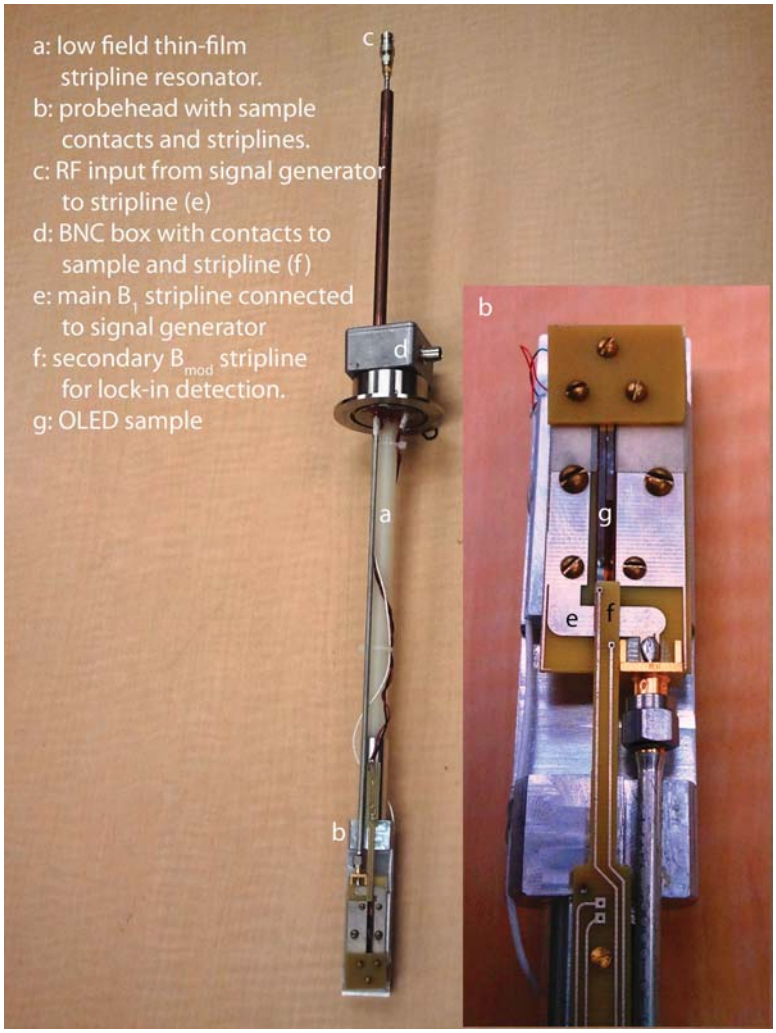

Figure A.7. A diagram explaining the components of the all-stripline low field resonator. This was used for some of the single pulse experiments as well as the frequency-sweep sensor configuration experiment.

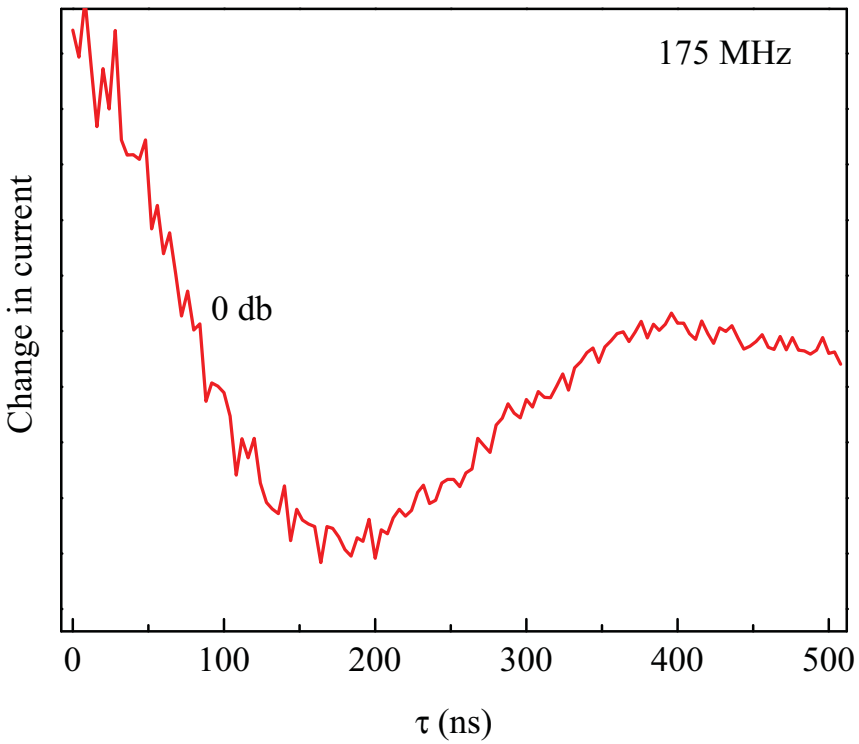

Figure A.8. A single Rabi-nutation experiment at 0db using the configuration shown in Fig. A.7 and Fig. A.2 with a RF of 175MHz with an external field of $B_0 = 62.6G$. Showing a π time of 175ns corresponding to a B_1 driving field of 1G.